Modeling and Control of Biomimetic Cilia-Based Devices for Microfluidic Applications

Jiradech Kongthon

A dissertation submitted in partial fulfillment of

the requirements for the degree of

Doctor of Philosophy

University of Washington

2011

Santosh Devasia, Chair

James J. Riley

Jae-Hyun Chung

Nathan J. Sniadecki

Program Authorized to Offer Degree:

Mechanical Engineering

University of Washington

Abstract

Modeling and Control of Biomimetic Cilia-Based Devices for Microfluidic Applications

Jiradech Kongthon

Chair of the Supervisory Committee:
Professor Santosh Devasia
Mechanical Engineering

This research investigates biomimetic cilia-based devices (cantilever-type vibrating devices) to reduce the time needed for micro-scale fluid mixing. Inspired by biological systems, the cilia-based devices (that are excited by external excitations) have been proposed for mixing and manipulating liquids in micro/nano-fluidic applications. This research develops models and control methods for such devices. Experimental mixing results, with and without cilia, are comparatively evaluated to show more than an order-of-magnitude reduction in the mixing time with the use of cilia.

TABLE OF CONTENTS

Page

List of Figures iv

List of Tables xi

Chapter 1: Introduction 1
1.1 Why Microfluidics 1
1.2 Challenges 2
1.3 Microfluidic Systems 3
1.4 How to Address the Challenges 4
1.5 Cilia-based Approaches 7
1.6 New Approach Proposed 8
1.7 Cilia in Nature 8
1.8 Research Problems 9
1.9 Structure of the Dissertation 14

Chapter 2: Added-mass effect in modeling of cilia-based devices for microfluidic systems 15
2.1 Overview 15
2.2 Introduction 15
2.3 Dynamics of Cilium in Fluid 18
2.4 Theoretical Modeling 22
2.5 Discussion of Added-Mass Effect 26
2.6 Conclusions 34

Chapter 3: Dynamics of Cilia-Based Microfluidic Devices 35
3.1 Overview 35
3.2 Introduction 35

3.3 Modeling the Cilia Dynamics 37
3.4 Experimental Results and Discussions 46
3.5 Conclusions 67

Chapter 4: Iterative Control of Piezoactuator for Evaluating Biomimetic, Cilia-Based Micromixing 68
4.1 Overview 68
4.2 Problem Formulation 70
4.3 Iterative Control of Piezoactuator 72
4.4 Experimental Evaluation of Mixing 84
4.5 Conclusions 94

Chapter 5: Conclusions and Future Works 95
5.1 Conclusions 95
5.2 Future Works 96

Bibliography 99

Appendix A: Optimal Inversion-Based Feedforward Control of Piezoactuator (without Feedback) 107
A.1 Introduction 108
A.2 Problem Formulation 108
A.3 Feedforward Control of Piezoactuator 110
A.4 Conclusions 117
A.5 Matlab Code 118

Appendix B: Making Biomimetic Cilia and Cilia Devices 126

Appendix C: Control Design and Implementation 134
C.1 Determining the Controller Gain, K 135
C.2 Hardware and Software for Implementing the Control 137
C.3 Iterative Control Approach to Finding the Inverse Inputs 141

Appendix D: Sample Images from Mixing Experiments, Image Analysis, and Plotting the Mixing Index 167
D.1 Sample Images Captured from Mixing Experiments in Chapter 4 . . . 168

D.2 Image Analysis and Plotting the Mixing Index 172

Appendix E: Particle Experiments and Determining the Speeds 178
E.1 Images Captured from the Particle Experiments in Chapter 4 179
E.2 Determining the Distance Traveled and the Time Taken for Computing the Speed 185

Appendix F: Student *t*-Test 186
F.1 Student *t*-test for Chapter 3 188
F.2 Student *t*-test for Chapter 4 189

LIST OF FIGURES

Figure Number Page

1.1 Illustration of turbulent flow : Eddy flows are right there to help accelerate mixing 2

1.2 Illustration of laminar flow : Solid lines with arrows represent streamlines and dots represent molecular diffusion increasing over time along the channel 3

1.3 Illustration of mixing with flow (continuous flow mixing) in Y-shaped microchannel 5

1.4 Illustration of mixing without flow (batch mode mixing) in microliter well 6

1.5 Research problem on added mass:(a)cilia shaken in air (b)cilia shaken in water 10

1.6 Research problem on sloshing: whole chamber containing cilia shaken 12

1.7 Excitation waveforms u_c for one time period: (a) desired symmetric, sinusoidal waveform $u_{c,d}$, (b) preliminary asymmetric triangular waveform $u_{c,p}$, where the ratio $\alpha = t_A/t_B = 0.25$ is a measure of the time asymmetry. 13

2.1 (a) Experimental setup for testing the resonant vibrational frequency of cilia. (b) Image of a cilium excited by piezo stage. (c) Nominal cilium dimensions are length $L = 800\mu m$, depth $D = 10\mu m$, and height $H = 45\mu m$. 19

2.2 Frequency response of cilia with nominal dimensions $L \times H \times D = 800 \times 45 \times 10\mu m$ in: (a) air; and (b) de-ionized (DI) water. Dots represent the experimental data (mean value of six cilia), and bars represent the standard deviation $\pm\sigma$. Lines represent the response of the model in Eq. 2.2 with the fitted parameters in Tables 2.1 and 2.2. 19

2.3 Contour plot for normalized resonant vibrational frequency $\bar{\omega}_r$ in Eq. 2.44. 30

2.4 Frequency response prediction in water for models of cilia (with different lengths): (a) with the added-mass effect (solid lines); and (b) without the added-mass effect (dashed lines). Experimentally measured data points are shown in the left plot. 33

3.1 Schematics of experiment for evaluating the frequency response of cilia. (a) Experimental setup. (b) Image of a cilium in water excited by the piezoactuator. (c) Input $u_b(t)$ and output $y(t)$ motions of the cilium. 39

3.2 Pressure gradient due to accelerating fluid generates buoyancy-like force across the thickness of a cilium. 41

3.3 Schematic experimental setup (images not to scale) for evaluating the effects of added mass and sloshing on the frequency response of cilia. Case (a) the cilia are oscillated in air; case (b) the cilia are oscillated in water (inside a stationary, relatively-large 60mm×115mm chamber); and case (c) the chamber (3mm diameter) containing the cilia is oscillated. In each case, three cilia are used. 47

3.4 Frequency responses for three cases. The frequency responses of the fitted models are shown using solid lines, and experimental mean values (for three cilia in each case) are represented by dots. Case (a) the cilia are oscillated air; case (b) the cilia are oscillated in water (inside a stationary chamber); and case (c) the chamber containing the cilia is oscillated. The same set of cilia is used in case (a) and case (b) to capture the added mass effect. The estimated added mass is used to model the cilia response with sloshing in case (c). 50

3.5 Experimental frequency responses (mean value of three cilia) with and without sloshing, i.e., free surface is constrained from sloshing with a glass cover. The same set of three cilia were used for both experiments, with and without sloshing. 52

3.6 Frequency responses for cilia in an oscillating chamber when the height of water is varied. Each data point (dot) represents the average value for the three cilia used in each experiment. The same cilia are used in all these experiments. The frequency responses of the fitted models are given by solid lines. 54

3.7 Variation of the sloshing natural-frequency ω_{sl} with the ratio of the water height h to the chamber radius R. The dots represent the experimental data and the solid line represents the prediction by the fitted model in Eq. (3.42) 55

3.8 Stationary chamber (case b): frequency responses for different-length cilia. Experimental values are represented by dots. Responses of models with parameters fitted by least-squares error minimization is presented with solid lines. 58

3.9 Oscillating chamber (case c): frequency responses for different-length cilia. Experimental values are represented by dots. Response of models with parameters fitted by least-squares error minimization is presented with solid lines. Dashed lines represent responses of predicted models. 60

3.10 Schematic setup of cilia device shown in Figure 3.1(a) for mixing experiments in a 3mm diameter chamber. 62

3.11 Sample images of the mixing process at different time instants t and corresponding mixing indices, I_{mix} as in Eq 3.45 : (a) with cilia, run 1 in Table 3.6 ; and (b) without cilia, run 1 in Table 3.6. 63

3.12 Time profiles of the mixing index I_{mix} in Eq. (3.45) for seven experimental runs with cilia. The 90% mixing time is indicated with circles. 65

3.13 Time profiles of the mixing index I_{mix} in Eq. (3.45) for seven experimental runs without cilia. The 90% mixing time is indicated with circles. 66

4.1 Schematics of experiment for evaluating micromixing with cilia. Experimental setup: (a) schematic; and (b) photo. (c) Nominal cilium dimensions are length $L = 800\mu m$, width $W = 10\mu m$, and height $H = 45\mu m$. (d) Base motion $u_c(t)$ at $x = 0$ and tip motion $y(t)$ at the free end $x = L$ of a cilium. (e) Photo of a cilium in water excited by piezoactuator. 71

4.2 Block diagram of the positioning system. The piezoactuator is represented by G_p, the achieved chamber motion u_c is measured with an inductive sensor with gain $K_s = 0.2$ (V/µm), and G_{cl} represents the closed-loop system. 72

4.3 Experimental frequency responses of the closed-loop system, G_{cl} in Figure 4.2 for two cases: small amplitude (dashed line); and large amplitude (solid line). 73

4.4 Hysteresis in the closed-loop piezoactuator system obtained by applying sinusoidal input V to the closed-loop system at 20Hz and measuring the resulting output position u_c. 74

4.5 Frequency response of seven runs of cilia. Dots represent the experimental data (mean values of seven runs of cilia), and bars represent the standard deviation $\pm\sigma$. Detailed models can be found in Refs. [1, 2]. 75

4.6 Excitation waveforms u_c for one time period: (a) desired symmetric, sinusoidal waveform $u_{c,d}$, (b) preliminary asymmetric triangular waveform $u_{c,p}$, where the ratio $\alpha = t_A/t_B = 0.25$ is a measure of the asymmetry. 77

4.7 Input energy weight, $R(\omega)$ and tracking-error weight, $Q(\omega)$ used in the cost function (in Eq. 4.1) to find the optimal inverse V_{opt} and the optimally filtered bandwidth-limited asymmetric waveform $u_{c,opt}$. . . . 78

4.8 Asymmetric waveform: (dashed line) original, infinite-bandwidth, triangular waveform; and (solid line) optimally-filtered, bandwidth-limited waveform. 80

4.9 The frequency dependent bound $M(\omega)$ (solid line) on the iteration gain $\rho(\omega)$ as in [3]. The minimum value (0.8) is shown as a dashed line. . . 80

4.10 Iteration results for iteration steps k from 1 to 6: (a) optimal inverse input $V_{opt,k}$; (b) experimentally measured waveform $u_{c,k}$; and (c) error in waveform $E_k(t) = u_{c,opt}(t) - u_{c,k}(t)$. 82

4.11 Comparison of initial $u_{c,1}$ and final ($u_{c,6}$ at iteration step 6) waveforms with the desired, optimal, asymmetric waveform $u_{c,d} = u_{c,opt}$. 83

4.12 (a) Schematic and (b) photo of setup of cilia device for mixing experiments in a 3mm diameter chamber. 85

4.13 Sample images of the mixing process at different time instants t for Run 1: (a) sinusoidal excitation without cilia (b) sinusoidal excitation with cilia; (c) asymmetric excitation without cilia; and (d) asymmetric excitation with cilia. 87

4.14 Mixing indices for devices with : (a) sinusoidal excitation without cilia, (b) sinusoidal excitation with cilia. 90

4.15 Mixing indices for devices with : (a) asymmetric excitation without cilia, (b) asymmetric excitation with cilia. 91

A.1 Schematics of experiment for evaluating micro-mixing with cilia. (a) Experimental setup. (b) Image of a cilium in water excited by piezoactuator. (c) Base motion $u_c(t)$ at $x = 0$ and tip motion $y(t)$ at the free end $x = L$ of a cilium. (d) Nominal cilium dimensions are length $L = 800\mu m$, width $W = 10\mu m$, and height $H = 45\mu m$. 109

A.2 Block diagram of the positioning system. An input voltage V is amplified by K_{amp} to V_a and applied to the piezoactuator (model G_p). The amplifier gain K_{amp} is adjusted to achieve a fixed-amplitude for the excitation waveforms u_c applied to the cilia-containing chamber. Such fixed-amplitude motion of the cilia chamber enables the comparative evaluation of mixing with different excitation waveforms u_c. 110

A.3 Experimental and model-based frequency response of piezoactuator G_p in Figure A.2. Experimental responses are shown for two different input amplitude levels: the dashed line represents the response with input voltage $V_a = 11.2$V peak-peak; and the dotted line represents the response with $V_a = 16$V peak-peak. The response of the fitted model G_p (in Eq. A.1) is represented by the solid line. 111

A.4 Excitation waveforms u_c for one time period: (a) sinusoidal waveform, (b) sawtooth waveform. 112

A.5 Input energy weight, $R(j\omega)$ and tracking-error weight, $Q(j\omega)$ used in the cost function (in Eq. A.2) to find the optimal inverse. 114

A.6 Simulation results using the piezoactuator model G_p in Figure A.2. Input voltages V_a are shown in plot (a) and the corresponding responses u_c of the piezoactuator are in plot (b). Results are shown for three cases: (a) sawtooth excitation; (b) without correcting dynamics $V_{a,DC}, u_{c,DC}$; and (c) optimal input-output $V_{a,opt}, u_{c,opt}$. 116

A.7 Comparison of simulation and experimental results. Simulated response (solid line) and experimental response (dotted line) for three cases: (a) sawtooth excitation; (b) without correcting dynamics $V_{a,DC}, u_{c,DC}$; and (c) optimal input-output $V_{a,opt}, u_{c,opt}$. Plot (d) shows the error between the simulated response and and experimental response with the optimal input $V_{a,opt}$. 118

B.1 Weighing polydimethylsiloxane (PDMS) and curing agent 128

B.2 Mixing polydimethylsiloxane (PDMS) with curing agent 129

B.3 Mixture left in the vacuum chamber for air bubble removal 129

B.4 Filling the mixture onto the mold 130

B.5 Precise manipulation of the mixure through the microscope 130

B.6 Mixure on the mold left at the room temperature for 20 minutes for the complete fill-up 131

B.7 Mixure on the mold left in the oven for 12 hours for curing 131

B.8 Peeling off the cilia structure from the mold 132

B.9 An array of cilia obtained 132
B.10 Cutting the array to obtain a shorter array 133
B.11 Final assembly of the mixing chamber, ready for mixing experiments 133

C.1 Root locus 136
C.2 Circuit diagram 138
C.3 Op-amp circuit built on the breadboard connected to NI myDAQ : Power supply lines, ground lines, blue capacitors between them, and DAQ wires on the circuit board are not shown in Figure C.2. 139
C.4 Labview front panel for DAQ system while running the mixing experiment 139
C.5 Labview block diagram for DAQ system 140

D.1 Sample images captured at different mixing indices for sinusoidal excitation without cilia 168
D.2 Sample images captured at different mixing indices for sinusoidal excitation with cilia 169
D.3 Sample images captured at different mixing indices for asymmetric excitation without cilia 170
D.4 Sample images captured at different mixing indices for asymmetric excitation with cilia 171
D.5 Pinnacle studio used to capture videos 172
D.6 Selecting the frame range and choosing a decimation number : Decimated by 3 for mixing with cilia and decimated by 15 for mixing without cilia (slower settling time) 173
D.7 Exporting the image sequence 173
D.8 Storing the images 174
D.9 Mixing index plot 177

E.1 Captured image used for measuring the distances traveled by particles 1 to 10 while being under the influence of sinusoidal excitation without cilia : Initial frame 179
E.2 Captured image used for measuring the distances traveled by particles 1 to 10 while being under the influence of sinusoidal excitation without cilia : Final frame 180
E.3 Captured image used for measuring the distances traveled by particles 1 to 5 while being under the influence of sinusoidal excitation with cilia : Initial frame 180

E.4 Captured image used for measuring the distances traveled by particles 1 to 5 while being under the influence of sinusoidal excitation with cilia : Final frame 181
E.5 Captured image used for measuring the distances traveled by particles 6 to 10 while being under the influence of sinusoidal excitation with cilia : Initial frame 181
E.6 Captured image used for measuring the distances traveled by particles 6 to 10 while being under the influence of sinusoidal excitation with cilia : Final frame 182
E.7 Captured image used for measuring the distances traveled by particles 1 to 10 while being under the influence of asymmetric excitation without cilia: Initial frame 182
E.8 Captured image used for measuring the distances traveled by particles 1 to 10 while being under the influence of asymmetric excitation without cilia: Final frame 183
E.9 Captured image used for measuring the distances traveled by particles 1 to 5 while being under the influence of asymmetric excitation with cilia: Initial frame 183
E.10 Captured image used for measuring the distances traveled by particles 1 to 5 while being under the influence of asymmetric excitation with cilia: Final frame 184
E.11 Captured image used for measuring the distances traveled by particles 6 to 10 while being under the influence of asymmetric excitation with cilia: Initial frame 184
E.12 Captured image used for measuring the distances traveled by particles 6 to 10 while being under the influence of asymmetric excitation with cilia: Final frame 185

F.1 Values of t_α , from Table 4 in [4] 198

LIST OF TABLES

Table Number Page

2.1 Experimental fit of the parameters in Eq. 2.2 for six cilia actuated in air ($L = 800\mu$m), where σ represents the standard deviation and $K = 1.566$. 20

2.2 Experimental fit of the parameters in Eq. 2.2 for cilia actuated in DI water ($L = 800\mu$m), where σ represents the standard deviation and $K = 1.566$. 21

2.3 Columns 2-5: experimental fit of the parameters in Eq. 2.2 for cilia with different lengths L actuated in DI water with $K = 1.566$. Columns 6-9: predicted natural frequencies $\omega_{n,w,p}$ and resonant vibrational frequencies $\omega_{r,w,p}$ using parameters for the 800μm cilia (in Table 2.2), and prediction errors $E_{n,w}, E_{r,w}$ as in Eq. 2.50. The predictions are not applicable (N/A) for the 800μm case. 32

3.1 Parameters for three cilia (length $L = 800\mu$m) actuated in air, i.e., case (a), with the transfer function given in Eq. (3.37). The resonance frequency of the fitted model is $\omega_{r,a}$. 49

3.2 Parameters for three cilia (the same cilia as in Table 3.1 in air) actuated in water, i.e., case (b), with the transfer function given in Eq. (3.37). The resonance frequency of the fitted model is $\omega_{r,b}$. 50

3.3 Variation of sloshing parameters with water height in the chamber. . 54

3.4 Stationary chamber: parameters and maximum amplification A_{max} of fitted models for different-length cilia corresponding to Figure 3.8. . . 60

3.5 Oscillating chamber: parameters and maximum amplification A_{max}, of fitted models for different-length cilia corresponding to Figure 3.9 along with maximum error (Eq. 3.44) in fitted and predicted models. 61

3.6 Mixing time(s) quantified by the time for the mixing index I_{mix} in Eq. (3.45) to reach and stay within 90% of its final value, with and without cilia. 67

4.1 Resonant Frequencies of cilia (seven runs) 76

4.2 Maximum $E_{k,max}$ and rms $E_{k,rms}$ tracking error 83

4.3 Mixing time(s) for sinusoidal excitation, quantified by the time for the mixing index I_{mix} in Eq. (4.10) to reach and stay within 90% of its final value, without and with cilia 92
4.4 Mixing time(s) for asymmetric excitation, quantified by the time for the mixing index I_{mix} in Eq. (4.10) to reach and stay within 90% of its final value, without and with cilia 93
4.5 Speed, mean value and standard deviation for 10 microspheres for each of the four cases — without and with cilia, and symmetric (sinusoidal) and asymmetric excitation 94

A.1 Parameters of piezoactuator model G_p in Eq. (A.1) 112

C.1 Parameters of piezoactuator model G_p in Eq. (C.1) : Open-loop model 135
C.2 Closed-loop pole locations 136

F.1 Critical regions for testing $\mu_1 - \mu_2 = \delta$ 187
F.2 Mixing time, mean value and standard deviation for 7 runs for each of the four cases — without and with cilia, and symmetric (sinusoidal) and asymmetric excitation 189
F.3 Speed, mean value and standard deviation for 10 microspheres for each of the four cases — without and with cilia, and symmetric (sinusoidal) and asymmetric excitation 189

ACKNOWLEDGMENTS

This dissertation would not have come into existence without the encouragement, support, and guidance of many individuals. As my dissertation closes, I would love to express my deepest gratitude to all of the hearts and souls I met along the way.

First and foremost, with so much respect, appreciation, and admiration, I would like to express my deepest gratitude to my advisor, Professor Santosh Devasia for his constant guidance, dedication, encouragement, help, support, and care in all stages of my research. I am very fortunate and greatly honored to have Professor Santosh Devasia direct my dissertation. I learned a lot of lessons from him even beyond the classrooms and the books. His scholarly and systematic guidance and his enthusiasm for research helped me hurdle all of the obstacles and accelerate the completion of this research.

I would like to thank the members of the supervisory committee, Professor James J. Riley, Professor Jae-Hyun Chung, Professor Nathan J. Sniadecki, Professor Kailash C. Kapur, and Professor Richard L. Storch, for their challenging questions, constructive comments, and time. My special thanks go to Professor James J. Riley, Professor Jae-Hyun Chung, Doctor Kieseok Oh, and Brandon P. Smith, for their collaboration in this research project.

I would like to gratefully acknowledge Professor John Kramlich for appointing me to be a teaching assistant and an instructor. The appointments provided me with invaluable teaching experience and will benefit my career growth in the future. I would also like to take this opportunity to thank all of the teachers in my life for shaping and brightening my future.

I would also like to thank my labmates and friends for their camaraderie, moral support, informative discussions, and for the fun and joy we shared in snow, on mountains, in lakes, and on beaches.

My heartfelt gratitude goes to my parents, my loving siblings, and my loved ones including my soulmate, for their unconditional love, support, understanding, and warm encouragement. Unfortunately, my beloved parents, who would love to frame all of my diplomas and post them on the wall, passed away. I am sure that they would have been very proud of me, and I am very grateful to them forever.

Besides individuals, I would like to acknowledge the National Science Foundation for the generous support through NSF grants CMII 0624597 and CMII 1000404. Lastly, I would love to thank the University of Washington for building an excellent academic climate and for being my alma mater. I take pride in being an alumnus.

DEDICATION

to my parents, my loving siblings, and my loved ones

Chapter 1

INTRODUCTION

This research investigates biomimetic cilia-based devices (cantilever-type vibrating devices) to reduce the time needed for micro-scale fluid mixing. Inspired by biological systems, the cilia-based devices (that are excited by external excitations) have been proposed for mixing and manipulating liquids in micro/nano-fluidic applications. This research develops models and control methods for such devices. Experimental mixing results, with and without cilia, are comparatively evaluated to show more than an order-of-magnitude reduction in the mixing time with the use of cilia.

1.1 Why Microfluidics

Microfluidic systems can save samples, cost, and time. For example, an acoustic 96-well microplate mixer manufactured by Advalytix, can handle liquid volumes in nanoliter scale. With a very small volume of liquid, material costs and process time can be saved compared to a larger scale volume process.

The well size has been miniaturized over years. In early 1950s in Hungary where a severe outbreak of influenza took place, Dr. Gyola Takatsy needed faster diagnostic tests for hundreds of patients and the standard test tube was too cumbersome and time-consuming. Dr.Takatsy then made the first microplate [5] with 6 rows of 12 wells and used in place of the test tubes. In 1967, Nelson M. Cooke and Paul H. Hall invented and patented the disposable microtitration plate [6], composed of 96 wells(8 rows and 12 columns) with a capacity of either 25 or 50 microliters. In 2002, Affymax, a drug discovery firm based in Palo Alto, California, was reported to manufacture a 20,000-well plate in which had a volume of just 25 nanoliters, [7].

The revolution of microfluidic research is miniaturizing and transforming a large laboratory analyzing fluids into a microchip-based system called "lab on a chip". Large and costly instruments are being replaced by microchip-based systems developed by MEMS technology. Microfluidic systems streamline experimental and analytical processes, provide convenience, and save samples, costs, and time.

1.2 Challenges

In general, mixing is not difficult in macroscale where turbulent mixing can be achieved because in a turbulent regime, eddy flows, or vortices can help increase interfacial areas between fluids, thereby accelerating the mixing as illustrated by Figure 1.1.



Figure 1.1: Illustration of turbulent flow : Eddy flows are right there to help accelerate mixing

In microfluidic devices where the characteristic length is very small, Reynolds numbers are very small [8]. Under these conditions, the flow is only in the laminar regime where fluids flow in parallel streamlines (smooth flow) and the layers in the flow are well-defined (illustrated by Figure 1.2), so the eddy flows generally do not occur.

In microfluidic devices, mixing then occurs by diffusion only, but in general the diffusion in liquids is a slow process, compared to diffusion in gas, especially for large particles such as DNA and protiens. The rate of diffusion is inversely proportional to the molecular weight of the substance. Therefore, the mixing in microscale can be slow for large particles. In particular [9], for large molecules, such as DNA and

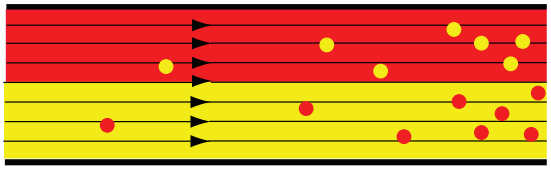

Figure 1.2: Illustration of laminar flow : Solid lines with arrows represent streamlines and dots represent molecular diffusion increasing over time along the channel

proteins, the diffusion coefficients are in the order of $10^{-10}m^2/s$ or less as the diffusion coefficient of water in water is $2.3 \times 10^{-9}m^2/s$ (23 times larger). Hence, the mixing time and the mixing length can both be very long and impractical.

1.3 Microfluidic Systems

A microfluidic system moves fluids through a network of microchannels and microchambers. Processes such as pumping,valving, separating ,and mixing fluids take place on a lab on a chip. Mixing of fluids on a lab on a chip is one of the most challenging issues ,and can take place in either microchannels or microchambers. In this research, the focus will be given to the mixing issue on how to improve mixing in a microchamber.

The literature in the field discusses a number of devices designed to enhance micromixing. These devices fall into one of two categories [10]:

1) active mixers that utilize external perturbations to introduce vorticity into laminar flow. Active mixers use a periodical change of pumping energy or electrical fields, acoustic fluid shaking, ultrasound, electrowetting-based droplet shaking, microstirrers, or others.

2) passive mixers that use no energy input except the mechanism (pressure head or pump) used to drive the fluid flow. Examples of these devices and techniques are Y- and T-type flow mixers, multi-laminating mixers, split-and-recombine mixers, chaotic mixers, jet colliding mixers, recirculation flow mixers, and others.

Many attempts have been made to enhance passive mixing in microchannels. One way of achieving good mixing at low Reynolds numbers is to introduce the phenomenon known as chaotic advection in which simple regular velocity fields generate chaotic particle trajectories. Chaotic advection typically creates the exponential growth of the interfacial area [10], which results in rapid mixing. In order to introduce chaotic advection, the geometry of a channel must be complicated enough while the fabrication process of the channel is simple enough [11].

Several works have been done to complicate microchannels. For example, the staggered herringbone pattern is provided to at the bottom of the channel to introduce chaotic advection to reduce the mixing length, or the mixing time [12]. A three-dimensional serpentine microchannel design is implemented to generate chaotic advection to passively enhance fluid mixing [11].

1.4 How to Address the Challenges

There are two approaches to overcome the diffusion limit for micromixing: (i) mixing with flow, and (ii) mixing without flow.

1)Mixing with Flow

Several works have achieved good mixing by using continuous flows. For example, passive techniques such as channels with patterned grooves can be used to generate chaotic folding (and refolding) of the liquid as it flows past the grooves to improve mixing [12]. Such flow-type mixing can be used when a sufficiently-large amount of sample is available to achieve the flow through the grooved channel. In this work, flows and the patterned channel help accelerate mixing. Mixing with flow can be illustrated by Figure 1.3.

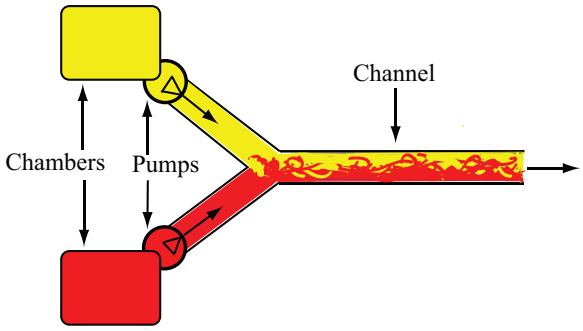

Figure 1.3: Illustration of mixing with flow (continuous flow mixing) in Y-shaped microchannel

There are other approaches to improving the mixing with flows. For example, acoustic fields [13], magnetic fields [14], [15], or electrical fields [9], [16], [17] were used to achieve good mixing with flow, but those external fields could damage samples.

Since mixing with flow depends on continuous flows, some disadvantages or problems may arise due to the dependence on the flow. For example, as seen in Figure 1.3, the system needs external chambers and pumps and dead volume is present in the system. Moreover, if there are some particles in the system, the particles may clog the channels. Furthermore, if solutions have larger viscosity (such as protein solutions) and the microchannels get smaller, larger flow impedance will be created, so a higher pump power is required. If the pump power is insufficient, then the microchannels could be clogged [18], and therefore, it is difficult to achieve good mixing. Also if the amount of samples is insufficient or samples are expensive, mixing with flow is not a good choice. Mixing with flow is then not practical for those cases. Hence, an approach that does not depend on the flows is needed, and mixing without flow can be used in place of mixing with flow for those cases.

2) Mixing without Flow

Mixing without flow is preferred when the amount of samples are insufficient or sam-

ples are expensive. Another advantage of mixing without flow is that no external microchannels/microchamber are required.



Figure 1.4: Illustration of mixing without flow (batch mode mixing) in microliter well

In mixing without flow, there is no external flow to help improve mixing (e.g. in Figure 1.4), so it is more challenging to achieve good mixing. Several approaches have been proposed and implemented to achieve good mixing without flow. For example, acoustic fields [19], [20], magnetic fields [21], or electrical fields [22] were used to allow good batch mode mixing, but those external fields could damage samples. For example, acoustic waves were used to improve mixing as shown in [19]. However, the very high frequency waves(from 100MHz to 6GHz) applied to improve mixing could damage the sensitive biosamples.

Biomaterials such cells and proteins are delicate and this often causes problems in bioprocessing. One such problem is "shear" [23].

The application of ultrasonic wave to improve mixing shows the promise in terms of mixing performance, but ultrasonic frequency could cause negative bioeffects such as disaggregating bacteria cells, disrupting human erythrocytes and platelets , or others due to its high shear strain rate, or high shear strain field [20].

It is noted that typical research issues in mixing without flow are on:

1) how to increase the rate of mixing.

2) how to avoid the damage to biosamples due to electrical, magnetic, acoustic fields,or mechanical forces.

1.5 Cilia-based Approaches

Several works based on cilia have been proposed to increase the rate of mixing without damage to samples.

For example, an actuator made of self-oscillating soft polymer gel was used to mimic cilia motion [24]. The swelling-de-swelling oscillations of polymer gel acted as the actuator, but the actuator had the actuation frequency of 0.0055Hz, which is much lower than the typical beating frequency of cilia in nature.

Another work made use of polydimethylsiloxane (PDMS) to fabricate cardiomyocyte bio-microactuator. The fabricated soft PDMS micropillar structures were actuated to perform repetitive motion by attached pulsating cardiomyocytes [25], but this is challenging because cardiomyocyte must be cultured and attached to the micropillars.

The work in [26] used magnetic field to actuate high-aspect-ratio cantilevered micro- and nanorod arrays made of a PDMS-ferrofluid composite material. The composite material composed of magnetic particles and PDMS material was controlled by a magnetic field. However, it is challenging in the fabrication process because the formation of the structure was not uniform and the irregular composite structure caused a nonuniform deflection. Another concern is that the magnetic field can cause damage to sensitive samples such as biomolecules and enzymes [27].

Another attempt to mimic cilia motion and create micromixing is in [28]. This work used electrostatic actuation of artificial cilia and showed the mixing of fluid flows. The cilia composed of curled polymer coated chromium (Cr) micro-beams were manipulated easily using an AC voltage to produce micromixing. However, a high AC electric field can cause damage to biosamples and limits bio-applications due

to cell lysis [29] and electrolysis of the solution [30].
To avoid possible damage to biosamples due to acoustic, magnetic,and electric fieilds, the new cilia-based approach is proposed in this research.

1.6 New Approach Proposed

This research proposes a low-frequency mechanical excitation approach for biomimetic cilia to increasing the rate of mixing in a microscale device. There are several advantages for the low-frequency approach to excite the cilia. Namely, no magnetic,electrical,or acoustic fields are present in the device and biomimetic cilia are similar (soft, low frequency) to biological cilia which seem to be biofriendly (more biomimetic). It is anticipated that there is potentially less damage to biosamples.

The work in [31] shows that noticeable damage of the biomolecules in the cilia mixer has not been observed. It is speculated that the biocompatible mixing is improved by the complex circulation flow caused by the resonating cilia. The flow induced by the cilia does not generate a high local shear flow and this can avoid the damage to the biomolecules. Further investigation on biomolecular damage is needed to support this notion.

1.7 Cilia in Nature

Biological cilia are very fine, hair like (micron scale) soft structures that beat in a rythmic manner (10-100 Hz) [32].

In general,the fluid manipulations of cilia can be viewed in two ways.
1) Cilia generate motion. For example, a paramecium is covered with thousands of cilia around the body and uses beating cilia to swim through liquids.
2) Cilia move fluids and particles. Several cells in the human body have cilia. For example, lung cells have numerous cilia that move rhythmically to sweep and move mucus out of the lung.

1.8 Research Problems

The main contributions of this research are to address the following three issues in mixing with biomimetic cilia.

1) Added mass effect to explain the substantial reduction in the resonant vibrational frequency of the cilia operating in liquid when compared to the resonant frequency of the cilia in air. This work was published in [1].

2) Sloshing effect to explain the large amplitude of cilia tip motions even in the presence of substantial damping in liquid. This work was published in [2].

3) Exploring the potential of using asymmetric excitation waveforms to reduce mixing time. This work was published in [33] and was also submitted to appear in [34].

1.8.1 Added Mass Effect

This work shows that the added mass due to fluid structure interaction significantly affects the vibrational dynamics of cilia-based (vibrating cantilever-type) devices for handling micro-scale fluid flows. Commonly, the hydrodynamic interaction between the cilia-based actuators and fluid is modeled as a drag force that results in damping of the cilia motion.

This chapter reports on models for cilia-based devices (cantilever-type vibrating devices) for handling micro-scale fluid flows. Inspired by biological systems, cilia-based microactuators (that are excited by external vibrations or acoustic excitations) have been proposed for mixing and manipulating liquids in micro/nano-fluidic applications [32]. In such applications, models of the cilia dynamics are needed for optimizing the geometric design as well as controlling the cilia to maximize the flow and minimize the required input energy. The challenge in modeling such cilia-actuators is the coupling between the mechanical dynamics of the cilia and the fluid. Such coupling can lead to damping effects due to drag forces [35]- [37], which change the amplitude

and resonant vibrational frequency of the cilia when operated in liquid in contrast to operation in air or vacuum. However, experimental results are presented to show that the drag or damping effects are not sufficient to explain the substantial reduction in the resonant vibrational frequency when the cilia actuators are operated in liquid (as opposed to the natural frequency when the cilia actuators are operated in air).

The main contribution is to show that such damping effects cannot explain the substantial reduction in the resonant vibrational frequency of the cilia actuator operating in liquid when compared to the natural frequency of the cilia in air. It is shown that an added-mass approach (that accounts for the inertial loading of the fluid) can explain this reduction in the resonant vibrational frequency when operating cantilever-type devices in liquids. Additionally, it is shown that the added-mass effect can explain why the cilia-vibration amplitude is not substantially reduced in a liquid by the hydrodynamic drag force. Thus, this research shows the need to model the added-mass effect, both, theoretically and by using experimental results. In the evaluation of the added mass effect, the cilia are to be shaken in air and in water contained in a stationary and large chamber as illustrated in Figure 1.5(Figure not to scale),and the natural frequencies in air and in water are to be determined.

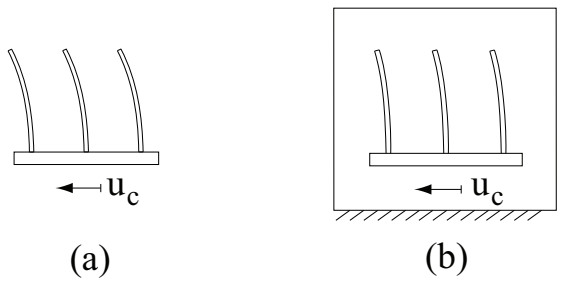

Figure 1.5: Research problem on added mass:(a)cilia shaken in air (b)cilia shaken in water

1.8.2 Sloshing Effect

In spite of the presence of substantial damping in water, the observed amplitude of cilia tip motions is still large when the whole chamber containing cilia and water is oscillated. This work models the dynamics of cilia-based devices (soft cantilever-type vibrating devices that are excited by external vibrations) for mixing and manipulating liquids in microfluidic applications. The behavior of biological cilia, discovered by Anton de Heide in 1684 [38], has been studied in, e.g., [38]- [43]. Bio-mimetic, cilia-like structures have been proposed for a variety of applications such as nasal filters [44] and sample transport [45]. In microfluidics, bio-mimetic actuators have been proposed for mixing and manipulation in liquid environments [46]- [50]. The main contribution of this chapter is to develop a model for a cilia-based device, which shows that liquid sloshing (e.g., [51, 52]) and the added mass effect (e.g., [53]- [56]) play substantial roles in generating large-amplitude motion of the cilia in liquid when the chamber containing the cilia is oscillated to mechanically excite the cilia resonance. Additionally, experimental results are presented to show that the average mixing time with cilia is more than an order-of-magnitude lower than the average mixing time without cilia.

Mixing can be improved by generating complex flows in the fluid to overcome the mixing-rate limits of laminar flows that are typical at the micro scale. For example, passive techniques such as channels with patterned grooves can be used to generate chaotic folding (and refolding) of the liquid as it flows past the grooves to improve mixing [12]. Such flow-type mixing can be used when a sufficiently-large amount of sample is available to achieve the flow through the grooved channel. In contrast, if the amount of sample is limited, then batch-type mixing is sought in small chambers containing the sample. Batch mixing can be enhanced using a variety of actuation techniques such as high-frequency ultrasound excitation [13, 57] and time-varying external magnetic fields [15], [21]- [59]. In the current work, cilia are ex-

cited by low-frequency oscillations (compared to higher-frequency acoustic excitation) of the chamber containing the sample. This low-frequency mechanical excitation of cilia is advantageous for mixing samples that are susceptible to damage from high-frequency excitation and magnetic fields. The work shows that batch mixing can be substantially improved by using cilia when compared to the case without cilia — for the same oscillatory actuation of the chamber.

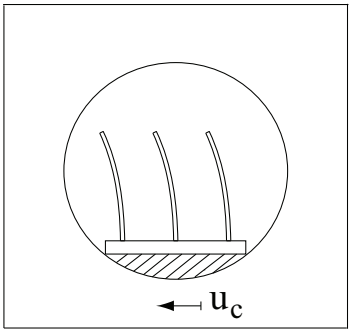

Figure 1.6: Research problem on sloshing: whole chamber containing cilia shaken

1.8.3 Effect of different excitation waveforms on mixing time

This work evaluates the use of different excitation waveforms as shown in Figure 1.7 to improve biomimetic-cilia-based mixing in microfluidic applications. A challenge in such studies is that, at high frequencies, vibrations in the piezoactuator can distort the achieved excitation waveform. An iterative approach is used in this work to account for the vibrational dynamics and avoid unwanted vibrations in the achieved excitation waveforms, and thereby enable the evaluation of different excitation waveforms on mixing. The main contribution of this work is to use these controlled, excitation waveforms for showing that (i) mixing time is substantially reduced (by more than an order of magnitude) with the use of cilia when compared to the case without cilia and (ii) mixing time with cilia can be further reduced (by more than half) by using an asymmetric excitation waveform when compared to symmetric (sinusoidal)

excitation.

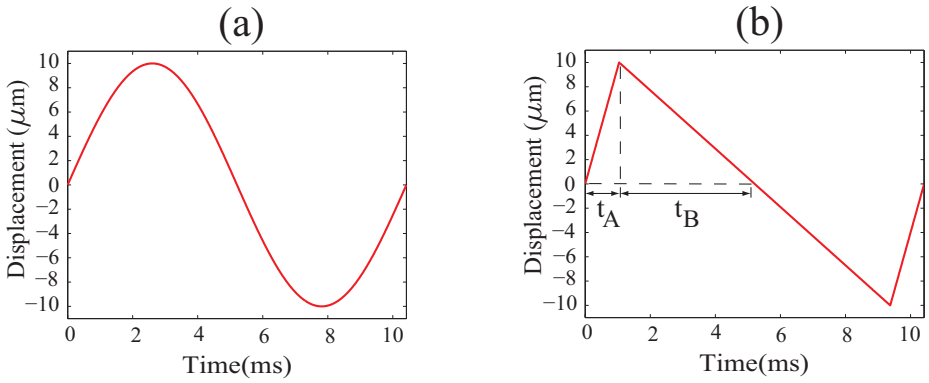

Figure 1.7: Excitation waveforms u_c for one time period: (a) desired symmetric, sinusoidal waveform $u_{c,d}$, (b) preliminary asymmetric triangular waveform $u_{c,p}$, where the ratio $\alpha = t_A/t_B = 0.25$ is a measure of the time asymmetry.

Based on biological cilia systems, e.g., [40–43], biomimetic, cilia-type, compliant actuators have been proposed for mixing and manipulation in liquid environments, e.g., see [15, 32, 46–50]. Recent works have shown that mechanical (sinusoidal) excitation of the cilia by using a piezoactuator to oscillate the cilia-chamber can improve mixing in microfludic devices [2, 60]. This work aims to evaluate potential improvements in cilia-based mixing with different excitation waveforms of the cilia-chamber. A challenge in such evaluation studies is that, at high frequencies, vibrations in the piezoactuator can distort the achieved motion (excitation waveform) of the cilia-chamber, and thereby, limit the ability to evaluate the effect of a desired excitation waveform on mixing. An iterative feedforward approach [61] is used in this work to account for the vibrational dynamics of the piezoactuator, and reduce unwanted vibrations in the achieved excitation waveforms.

In general, micromixing can be improved by generating complex flows in the fluid to overcome the mixing-rate limits of laminar flows that are typical at the microscale. For example, passive techniques such as grooves can be used to generate chaotic folding (and refolding) of the liquid as it flows past the grooves to improve mixing, e.g.,

in [12]. Such flow-type mixing can be used when a sufficiently-large amount of sample is available to achieve the flow through the grooved channel. In contrast, if the amount of sample is limited, then batch-type mixing needs to be achieved in small chambers containing the sample. Batch mixing can be enhanced using a variety of actuation techniques such as high-frequency ultrasound excitation [13, 57, 62] and time-varying external magnetic fields [15, 21, 58, 59]. In this work, cilia are excited by relatively-low-frequency oscillations of the chamber containing the sample when compared to higher-frequency ultrasound excitation. It is noted that the low-frequency excitation used in this chapter is advantageous for mixing samples that are susceptible to damage from high-frequency excitation [63–65]. Similarly, sample damage is a concern with the use of rapidly varying external magnetic fields, which is also avoided with the present approach. The work shows that batch mixing can be substantially improved by using low-frequency excitation with soft cilia — this use of low-frequency excitation with soft actuators has the potential to reduce the damage of fragile samples during micromixing.

1.9 Structure of the Dissertation

The dissertation discusses the added-mass effect in modeling of cilia-based devices for microfluidic systems in Chapter 2. Chapter 3 investigates the dynamics of cilia-based microfluidic devices to model and explain the sloshing effect. Chapter 4 demonstrates the use of iterative inversion to control the piezoactuator for evaluating the effect of different excitation waveforms on mixing time. Conclusions and future works are provided in Chapter 5.

Chapter 2

ADDED-MASS EFFECT IN MODELING OF CILIA-BASED DEVICES FOR MICROFLUIDIC SYSTEMS

2.1 Overview

This chapter shows that the added mass due to fluid structure interaction significantly affects the vibrational dynamics of cilia-based (vibrating cantilever-type) devices for handling micro-scale fluid flows. Commonly, the hydrodynamic interaction between the cilia-based actuators and fluid is modeled as a drag force that results in damping of the cilia motion. The main contribution is to show that such damping effects cannot explain the substantial reduction in the resonant vibrational frequency of the cilia actuator operating in liquid when compared to the natural frequency of the cilia in air. It is shown that an added-mass approach (that accounts for the inertial loading of the fluid) can explain this reduction in the resonant vibrational frequency when operating cantilever-type devices in liquids. Additionally, it is shown that the added-mass effect can explain why the cilia-vibration amplitude is not substantially reduced in a liquid by the hydrodynamic drag force. Thus, this chapter shows the need to model the added-mass effect, both, theoretically and by using experimental results.

2.2 Introduction

This chapter reports on models for cilia-based devices (cantilever-type vibrating devices) for handling micro-scale fluid flows. Inspired by biological systems, cilia-based microactuators (that are excited by external vibrations or acoustic excitations) have been proposed for mixing and manipulating liquids in micro/nano-fluidic applica-

tions [32]. In such applications, models of the cilia dynamics are needed for optimizing the geometric design as well as controlling the cilia to maximize the flow and minimize the required input energy. The challenge in modeling such cilia-actuators is the coupling between the mechanical dynamics of the cilia and the fluid. Such coupling can lead to damping effects due to drag forces [35]- [37], which change the amplitude and resonant vibrational frequency of the cilia when operated in liquid in contrast to operation in air or vacuum. However, experimental results are presented in this chapter to show that the drag or damping effects are not sufficient to explain the substantial reduction in the resonant vibrational frequency when the cilia actuators are operated in liquid (as opposed to the natural frequency when the cilia actuators are operated in air). The main contribution of this work is the use of an added-mass effect to account for this reduction in the natural frequency when cantilever-type devices are operated in a liquid. Thus, this work shows the need to include the added-mass effect (that accounts for the inertial loading of the liquid) when modeling the vibration of cantilever-type devices in a liquid medium.

Several works have modeled the vibrational dynamics of cilia-type (cantilever-type) devices operated in air [35, 36], liquid [37, 66], and vacuum [67]- [69]. The dynamics of these devices can be modeled as a second order linear dynamic system, as shown in [35]. The drag force between the cilia actuators and the fluid affects the dynamics. The damping caused by the drag force can change the amplitude and resonant vibrational frequency of the cilia actuators when operated in liquid in contrast to operation in air or vacuum. For example, experimental results, presented in this chapter, show that the resonant vibrational frequency $\omega_{r,w} = 109.54\text{Hz}$ of the cilia actuators in water is substantially smaller than the natural frequency $\omega_{n,a} = 338.68\text{Hz}$ of the cilia in air. However, this substantial reduction in the observed resonant vibrational frequency is not predicted by standard second-order models for such cantilever structures, which yield a resonant vibrational frequency expression of

$$\omega_{r,w} = \omega_{n,a}\sqrt{1 - 2\zeta^2} \tag{2.1}$$

where ζ is the damping ratio (e.g., see [70], Section 10.8). For example, the damping ratio ζ in a liquid tends to be in the range of 0.05 to 0.5 [66]. For this range of the damping ratio, the anticipated resonant vibrational frequency $\omega_{r,w}$ in a liquid is expected to be between $0.997\omega_{n,a} = 337.66\text{Hz}$ to $0.707\omega_{n,a} = 239.45\text{Hz}$ from Eq. 2.1. Note that this range (239.45Hz to 337.66Hz) is much larger than the observed experimental value for the resonant vibrational frequency in water of $\omega_{r,w} = 109.54\text{Hz}$. Thus, damping effects are not sufficient to capture the change in the resonant vibrational frequency of the cilia actuators when operated in liquids.

The main contribution of this work is to show that an added-mass effect is needed to account for the substantial reduction in the resonant vibrational frequency of cantilever-type devices in liquids. It is noted that the added-mass effect is important in models of underwater vehicles such as submarines [71], and was modeled in early works on pendulum oscillations initiated by Dubuat — the history of the added mass is provided by Stokes in [53]. Such an added-mass model is proposed to account for the substantial decrease in the vibrational natural frequency for cilia-type devices. The proposed added-mass model affects the natural frequency $\omega_{n,w}$ of the system in liquid, which in turn changes the resonant vibrational frequency $\omega_{r,w}$. Such changes in the natural frequency $\omega_{n,w}$ are shown to occur in experimentally obtained models. Additionally, it is shown that the added-mass effect can explain why the cilia-vibration amplitude is not substantially reduced in a liquid by the hydrodynamic drag force. Thus, this work shows the need to capture the added-mass effect to model the vibration of cantilever-type devices in liquid media.

2.3 Dynamics of Cilium in Fluid

2.3.1 System description

The displacement along the length (x) of a cilium is excited by the motion ($u(t)$) of the cilia base by using a piezo stage (Burleigh PZS200) as shown in Figure 2.1. The cilia are fabricated from polydimethylsiloxane (PDMS) using a silicon mold. Detailed information on cilia fabrication and material properties can be found in [32]. The nominal dimensions of the silicon mold used to fabricate the cilia used in the experiments are length ($L = 800\mu m$), height ($H = 45\mu m$), and depth ($D = 10\mu m$). The input to the system is the motion

$$u(t) = Asin(\omega t)$$

of the base of the cilia (actuated by the piezo stage) and the output of the system is the motion

$$y(t) = \hat{y}(L, t),$$

of the cilia tip, i.e., at the free end with $x = L$, as shown in Figure 2.1. The input (cilia-base motion $u(t)$) and the output (cilia-tip motion $y(t)$) are observed by using an optical microscope (Bausch & Lomb MicroZoom II High Performance Microscope with an attached Sony Color Video Camera 3CCD) and the displacement of the vibrating cilia is measured using captured still images (Pinnacle Studio Version 9.4.3). Two cases are studied: (a) cilia vibrating in air; and (b) cilia vibrating when immersed in water — the fluid container (see Fig. 2.1) is stationary. An example image of cilia vibrating in fluid is shown in Figure 2.1.

2.3.2 Experimental frequency response

The experimentally measured, input-to-output responses of the cilia (of nominal length $L = 800\mu m$) are shown in Figure 2.2 for two cases: (case a) cilia in air; and (case b) cilia in deionized water (DI water). The input-to-output frequency

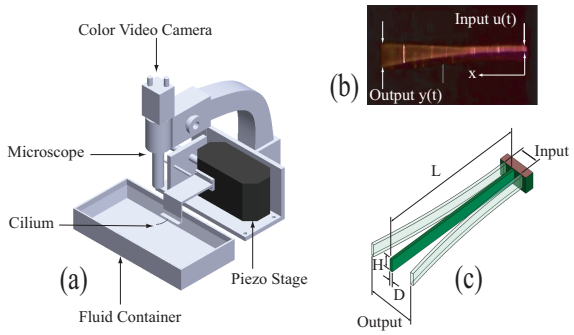

Figure 2.1: (a) Experimental setup for testing the resonant vibrational frequency of cilia. (b) Image of a cilium excited by piezo stage. (c) Nominal cilium dimensions are length $L = 800\mu m$, depth $D = 10\mu m$, and height $H = 45\mu m$.

responses in Figure 2.2 show a sharp increase in the output to input ratio near the resonant vibrational frequencies. Note that the resonant vibrational frequency $\omega_{r,w} = 109.54\text{Hz}$ of the cilia actuators in water is substantially smaller than the resonant vibrational frequency $\omega_{r,a} = 336.05\text{Hz}$ of the cilia in air.

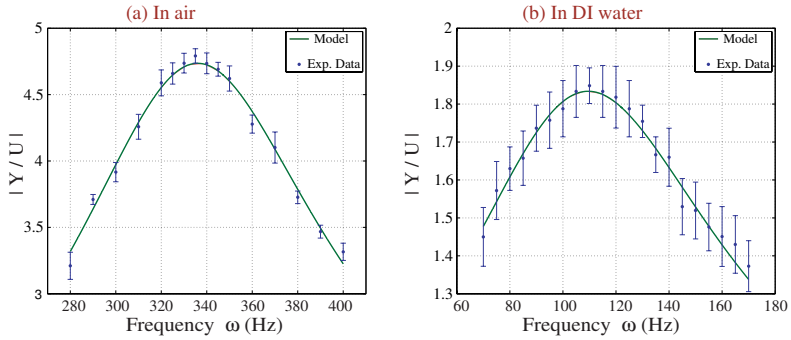

Figure 2.2: Frequency response of cilia with nominal dimensions $L \times H \times D = 800 \times 45 \times 10\mu m$ in: (a) air; and (b) de-ionized (DI) water. Dots represent the experimental data (mean value of six cilia), and bars represent the standard deviation $\pm\sigma$. Lines represent the response of the model in Eq. 2.2 with the fitted parameters in Tables 2.1 and 2.2.

2.3.3 Model of the frequency response

The experimental frequency responses (in air and in water) can be captured using simplified, second-order, linear models of the following form (similar to [35, 72])

$$G(s) = \frac{Y(s)}{U(s)} = \frac{-K(s^2 + 2\zeta_1\omega_n s)}{s^2 + 2\zeta_2\omega_n s + \omega_n^2} + 1 \tag{2.2}$$

where $G(s)$ is the transfer function in the Laplace domain, K is a constant related to the transfer function's gain, ω_n is the natural frequency, and ζ_1, ζ_2 are the damping ratios. It is noted that at small input frequencies (i.e., when $s \to 0$), the transfer function in Eq. 2.2 approaches one ($G(s) \to 1$), which implies that the tip displacement is similar to the base displacement. The parameters of the model, found by minimizing the least-squares-error between the predicted and measured frequency responses, are presented in Tables 2.1 and 2.2. The fitted model captures the experimental frequency response, as shown in Figure 2.2.

	ζ_1	ζ_2	$\omega_{n,a}$ (Hz)	$\omega_{r,a}$ (Hz)
Cilium 1	0.143	0.166	340.2	337.56
Cilium 2	0.145	0.167	340.8	338.12
Cilium 3	0.142	0.165	336.4	333.82
Cilium 4	0.145	0.167	336.9	334.25
Cilium 5	0.144	0.166	341.1	338.45
Cilium 6	0.145	0.166	336.7	334.09
Mean	0.1440	0.1662	338.68	336.05
σ	0.0013	0.0008	2.23	2.21

Table 2.1: Experimental fit of the parameters in Eq. 2.2 for six cilia actuated in air ($L = 800\mu$m), where σ represents the standard deviation and $K = 1.566$.

	ζ_1	ζ_2	$\omega_{n,w}$ (Hz)	$\omega_{r,w}$(Hz)
Cilium 1	0.43	0.45	116.4	109.19
Cilium 2	0.45	0.46	114.5	107.15
Cilium 3	0.44	0.45	117.6	110.40
Cilium 4	0.43	0.44	118.2	111.31
Cilium 5	0.44	0.45	114.1	107.12
Cilium 6	0.44	0.45	119.4	112.09
Mean	0.438	0.450	116.70	109.54
σ	0.008	0.006	2.10	2.10

Table 2.2: Experimental fit of the parameters in Eq. 2.2 for cilia actuated in DI water ($L = 800\mu$m), where σ represents the standard deviation and $K = 1.566$.

2.3.4 Reduction in natural frequency

There is a substantial reduction in the resonant-vibrational frequency and the natural frequency when the cilia are actuated in water in comparison to the case when the cilia are actuated in air, as seen in Tables 2.1 and 2.2. For example, the resonant vibrational frequency drops from 336.05Hz to 109.54Hz and the natural frequency drops from 338.68Hz to 116.70Hz. The considerable decrease in the natural frequency (and the associated resonance frequency) can not be explained by a standard model that predicts the natural frequency ω_n for a cantilever beam to be [73]

$$\omega_n = \omega_{n,a} = \omega_{n,w} = \left(\frac{1.875^2}{L^2}\right)\sqrt{\frac{EI}{\rho_b A_b}} = \beta^2\sqrt{\frac{EI}{\rho_b A_b}} \tag{2.3}$$

where ρ_b is the mass density, $A_b = DH$ is the cross sectional area, $I = HD^3/12$ is the area moment of inertia and E is the Young's modulus. Note that the natural frequency expression (in Eq. 2.3) does not depend on the fluid properties nor on damping effects. Therefore, there is a need to reformulate the model to include fluid effects to capture the reduction in natural frequency when operating in fluids — in

particular, to include the effect of inertial loading of the fluid on the cantilever. The modeling of this added-mass effect is discussed in the following section.

2.4 Theoretical Modeling

To predict the experimental second-order response in Eq. 2.2, a model can be developed by using the Euler-Bernoulli beam approach [35, 36, 73], as shown next.

2.4.1 Standard beam model without added-mass effect

The standard Euler-Bernoulli beam approach [72,73] to describe the net motion $\hat{y}(x,t)$ of a vibrating cilium (beam) is

$$\rho_b A_b \frac{\partial^2 \hat{y}(x,t)}{\partial t^2} + EI \frac{\partial^4 \hat{y}(x,t)}{\partial x^4} = f(x,t) \tag{2.4}$$

where the subscript b represents a property of the beam, the subscript w represents a property of the water (liquid) and the net motion $\hat{y}(x,t)$ is composed of the base motion, i.e., the input $u(t) = Asin(\omega t)$, and the elastic deflection, $\hat{w}(x,t)$ of the cilium (beam)

$$\hat{y}(x,t) \ = u(t) + \hat{w}(x,t). \tag{2.5}$$

The first term on the left hand side of Eq. 2.4 represents the inertial effects, the second term on the left hand side of Eq. 2.4 represents the elastic effects and $f(x,t)$ represents the external forces (per unit length), which is composed of two damping terms

$$f(x,t) = f_f(x,t) + f_i(x,t). \tag{2.6}$$

In the above equation, f_f is the distributed drag force due to hydrodynamic interaction that depends on the relative velocity between the structure and the fluid; it is approximated as (similar to [35, 36])

$$f_f(x,t) \ = -B_f \left[\frac{\partial \hat{y}(x,t)}{\partial t} - V_f \right] \ = -B_f \left[\frac{\partial \hat{y}(x,t)}{\partial t} \right] \tag{2.7}$$

where B_f is the fluid damping parameter that depends on the flow conditions, and V_f is the fluid velocity, which is zero in the current experimental setup. The internal damping force f_i per unit length (in Eq. 2.6) that depends on the rate of change of the beam's elastic deflection is

$$f_i(x,t) \;\; = \;\; -B_i(\frac{\partial \hat{w}(x,t)}{\partial t}) \tag{2.8}$$

where B_i is the internal damping parameter that depends on the beam properties. Applying the distributed fluid drag force, f_f in Eq. 2.7 and the distributed internal damping force, f_i in Eq. 2.8 as external forces, the Euler-Bernoulli equation (Eq. 2.4) becomes in the terms of the beam deflection $\hat{w}$ and base motion u (in Eq. 2.5)

$$\rho_b A_b \frac{\partial^2 \hat{w}(x,t)}{\partial t^2} + (B_f + B_i)\frac{\partial \hat{w}(x,t)}{\partial t} + EI\frac{\partial^4 \hat{w}(x,t)}{\partial x^4} \;\; = -B_f \dot{u}(t) - \rho_b A_b \ddot{u}(t) \tag{2.9}$$

with the standard, cantilever boundary conditions:

$$\hat{w}(0,t) = 0, \quad \frac{\partial \hat{w}(0,t)}{\partial x} = 0, \quad \frac{\partial^2 \hat{w}(L,t)}{\partial x^2} = 0, \quad \frac{\partial^3 \hat{w}(L,t)}{\partial x^3} = 0. \tag{2.10}$$

2.4.2 Modeling the added-mass effect

The added-mass effect arises because of the need to accelerate the fluid around an object when it is accelerated through a fluid [53] [54]- [56]. The inertia of the fluid exerts a resistive force on the body; this resistive force is termed as the *added-mass effect* because the body responds as if its mass has increased. This added-mass of the body depends on the medium in which the body (cilia-actuator) is moving. This added-mass effect can be modeled with an additional inertial forcing term (f_m) to the external force f in Eq. 2.6, which becomes

$$f(x,t) = f_f(x,t) + f_i(x,t) + f_m(x,t) \tag{2.11}$$

with

$$f_m(x,t) = -\rho_w A_w \frac{\partial^2 \hat{y}(x,t)}{\partial t^2} \;\; = -C_m \rho_b A_b \frac{\partial^2 \hat{y}(x,t)}{\partial t^2} \;\; = -C_m \rho_b A_b \left(\frac{\partial^2 \hat{w}(x,t)}{\partial t^2} + \ddot{u}(t) \right) \tag{2.12}$$

where A_w is the effective hydrodynamic area of the fluid that affects the inertial force f_m (per unit length), ρ_b is the beam density and

$$C_m = \frac{\rho_w A_w}{\rho_b A_b} \tag{2.13}$$

is the added-mass coefficient, which is zero if the added mass is zero. The beam Eq. 2.9, after dividing all terms with $\rho_b A_b (1 + C_m)$ becomes

$$\frac{\partial^2 \hat{w}(x,t)}{\partial t^2} + \frac{(B_f + B_i)}{\rho_b A_b (1 + C_m)} \frac{\partial \hat{w}(x,t)}{\partial t} + \frac{EI}{\rho_b A_b (1 + C_m)} \frac{\partial^4 \hat{w}(x,t)}{\partial x^4} = r(t) \tag{2.14}$$

with the forcing term $r(t)$ given by

$$r(t) = -\ddot{u}(t) - \frac{B_f}{\rho_b A_b (1 + C_m)} \dot{u}(t). \tag{2.15}$$

2.4.3 Transfer function for first vibrational mode

The partial differential Eq. 2.14 is solved by substituting the following separation of variables

$$\hat{w}(x,t) = \sum_{n=1}^{\infty} X_n(x) T_n(t) \tag{2.16}$$

for $\hat{w}$ into Eq. 2.14 to obtain

$$\sum_{n=1}^{\infty} X_n(x) \ddot{T}_n(t) + \frac{(B_f + B_i)}{\rho_b A_b (1 + C_m)} \sum_{n=1}^{\infty} X_n(x) \dot{T}_n(t) + \frac{EI}{\rho_b A_b (1 + C_m)} \sum_{n=1}^{\infty} X_n''''(x) T_n(t) = r(t). \tag{2.17}$$

Note that $X_n(x)$ represents the shape of the nth vibrational mode, which is obtained by considering the homogeneous equation with $r(t) = 0$ in Eq. 2.17. The homogeneous equation is satisfied if each mode satisfies

$$X_n(x) \ddot{T}_n(t) + \frac{(B_f + B_i)}{\rho_b A_b (1 + C_m)} X_n(x) \dot{T}_n(t) + \frac{EI}{\rho_b A_b (1 + C_m)} X_n''''(x) T_n(t) = 0 \tag{2.18}$$

which can be re-written as a function of x on one side and a function of t on the other side that are both constant $(-z^2)$, i.e.,

$$\frac{\ddot{T}_n(t)}{T_n(t)} + \frac{(B_f + B_i)}{\rho_b A_b (1 + C_m)} \frac{\dot{T}_n(t)}{T_n(t)} = -\frac{EI}{\rho_b A_b (1 + C_m)} \frac{X_n''''(x)}{X_n(x)} = -z^2.$$

This yields two equations

$$\ddot{T}_n(t) + \frac{(B_f + B_i)}{\rho_b A_b (1 + C_m)} \dot{T}_n(t) + z^2 T_n(t) = 0 \tag{2.19}$$

$$X_n''''(x) - \frac{\rho_b A_b (1 + C_m)}{EI} z^2 X_n(x) = 0. \tag{2.20}$$

Each mode shape X_n can be obtained from Eq. 2.20 as [73]

$$X_n(x) = cosh(\beta_n x) - cos(\beta_n x) - \sigma_n(sinh(\beta_n x) - sin(\beta_n x)) \tag{2.21}$$

where

$$X_n''''(x) = \beta_n^4 X_n(x) \tag{2.22}$$

$$\beta_n = \left[\frac{\rho_b A_b (1 + C_m)}{EI} z^2\right]^{1/4} \tag{2.23}$$

For the first mode of vibration $X_1(x)$

$$\beta_1 L = 1.875, \quad \sigma_1 = 0.7341. \tag{2.24}$$

Multiplying the non-homogeneous Eq. 2.17 with the first mode $X_1(x)dx$ and integrating with respect to the length after using the mode shape property in Eq. 2.22 results in

$$\sum_{n=1}^{\infty} \int_0^L X_1(x) X_n(x) dx \ddot{T}_n(t) + \frac{(B_f + B_i)}{\rho_b A_b (1 + C_m)} \sum_{n=1}^{\infty} \int_0^L X_1(x) X_n(x) dx \dot{T}_n(t) + \frac{EI}{\rho_b A_b (1 + C_m)} \sum_{n=1}^{\infty} \int_0^L \beta_n^4 X_1(x) X_n(x) dx T_n(t) = r(t) \int_0^L X_1(x) dx.$$

The orthogonality of the mode shapes results in only the first mode remaining after the integration in the above equation to yield

$$\ddot{T}_1(t) + \frac{(B_f + B_i)}{\rho_b A_b (1 + C_m)} \dot{T}_1(t) + \frac{EI}{\rho_b A_b (1 + C_m)} \beta_1^4 T_1(t) = r(t) K_1 \tag{2.25}$$

$$K_1 = \frac{\int_0^L X_1(x) dx}{\int_0^L X_1(x) X_1(x) dx} = \frac{0.783L}{L} = 0.783 \tag{2.26}$$

which can be rewritten (using r from Eq. 2.15) as

$$\ddot{T}_1(t) + 2(\zeta_f + \zeta_i)\omega_n \dot{T}_1(t) + \omega_n^2 T_1(t) = -K_1 \left[\ddot{u}(t) + 2\zeta_f \omega_n \dot{u}(t)\right] \tag{2.27}$$

where the natural frequency ω_n, fluid damping ratio ζ_f and internal damping ratio ζ_i are given by

$$\omega_n = \left(\beta_1^2\sqrt{\frac{EI}{\rho_b A_b}}\right)\frac{1}{\sqrt{(1+C_m)}} = \frac{\omega_n^*}{\sqrt{(1+C_m)}} \tag{2.28}$$

$$\zeta_f = \frac{1}{2\omega_n}\left(\frac{B_f}{\rho_b A_b\,(1+C_m)}\right) = \frac{B_f}{2\beta_1^2\sqrt{EI\rho_b A_b}}\frac{1}{\sqrt{(1+C_m)}} = \frac{\zeta_f^*}{\sqrt{(1+C_m)}} \tag{2.29}$$

$$\zeta_i = \frac{1}{2\omega_n}\left(\frac{B_i}{\rho_b A_b\,(1+C_m)}\right) = \frac{B_i}{2\beta_1^2\sqrt{EI\rho_b A_b}}\frac{1}{\sqrt{(1+C_m)}} = \frac{\zeta_i^*}{\sqrt{(1+C_m)}} \tag{2.30}$$

where $\omega_n^*, \zeta_f^*, \zeta_i^*$ are the natural frequency, fluid damping ratio, and internal damping ratio, respectively, without the added-mass effect. The total tip displacement, due to the first vibrational mode X_1 and the base motion $u(t)$ is

$$y(t) = X_1(L)T_1(t) + u(t) = 2T_1(t) + u(t). \tag{2.31}$$

since (from Eq. 2.21) $X_1(L) = 2$. Taking the Laplace transform on both sides of Eq. 2.27 to find $T(s)$, substituting this expression for $T(s)$ into Eq. 2.31 (after taking the the Laplace transform on both sides of Eq. 2.31), and dividing Eq. 2.31 by $U(s)$ yields

$$G(s) = \frac{Y(s)}{U(s)} = \frac{-2K_1(s^2 + 2\zeta_f\omega_n s)}{s^2 + 2(\zeta_f + \zeta_i)\omega_n s + \omega_n^2} + 1 \tag{2.32}$$

which is the same as the experimental model (in Eq. 2.2) with

$$K = 2K_1 = 1.566, \quad \zeta_1 = \zeta_f, \quad \zeta_2 = \zeta_f + \zeta_i \tag{2.33}$$

where the value of K_1 is from Eq. 2.26.

2.5 Discussion of Added-Mass Effect

This section begins with a discussion of the effective fluid area that influences the inertial loading to quantify the added-mass effect. This is followed by a comparative evaluation of models with and without the added-mass effect. In particular, it is

shown that the added-mass effect (when compared to the case without the added mass): (i) lowers the resonant vibrational frequency; and (ii) increases the vibrational amplitude at resonance in liquid.

2.5.1 Quantifying the added-mass effect

The added-mass coefficient C_m (in Eq. 2.13) quantifies the added mass $\rho_w A_w$ (per unit length of the beam) in terms of the displaced mass $\rho_b A_b$. The value of the added-mass coefficient C_m, in water, is obtained by using Eq. 2.28 and Tables 2.1, 2.2 as

$$C_m = \left(\frac{{\omega_n^*}^2}{{\omega_{n,w}}^2} - 1\right) \approx \left(\frac{{\omega_{n,a}}^2}{{\omega_{n,w}}^2} - 1\right) = \left(\frac{338.68^2}{116.70^2} - 1\right) = 7.42 \tag{2.34}$$

where the natural frequency ω_n^* without the added-mass effect (as in Eq. 2.28)

$$\omega_n^* = \beta_1^2 \sqrt{\frac{EI}{\rho_b A_b}}, \tag{2.35}$$

which is the same in water as in air, is approximated by the natural frequency in air $\omega_{n,a}$ because the added-mass effect is expected to be relatively negligible in air due to the low density of air when compared to water, i.e.,

$$\omega_n^* \approx \omega_{n,a}. \tag{2.36}$$

The effective hydrodynamic area A_w that contributes to the added-mass effect as the beam oscillates in water can be quantified in terms of the height H of the beam as (using Eq. 2.13)

$$A_w = \gamma H^2 = C_m \left(\frac{\rho_b A_b}{\rho_w}\right). \tag{2.37}$$

The density of the PDMS cilia (which ranges from $940 - 1000\text{kg/m}^3$ is similar to the density 1000kg/m^3 of DI water. Therefore, the coefficient γ (in Eq. 2.37) can be estimated from the value of C_m in Eq. 2.34 and the cilia depth $D = 10\mu\text{m}$ and height $H = 45\mu\text{m}$

$$\gamma = C_m \left(\frac{\rho_b D}{\rho_w H}\right) = 7.42(10/45)\left(\frac{\rho_b}{\rho_w}\right) = 1.65\left(\frac{\rho_b}{\rho_w}\right) \tag{2.38}$$

to lie in the range

$$1.55 \leq \gamma \leq 1.65 \ . \tag{2.39}$$

Comparison with added-mass effect on cylinder

Note that for a cylinder with cross-section diameter H, the area A_{cyl} associated with added-mass term is [74] (Chapter 4),

$$A_{cyl} \ = (\pi/4)H^2 \ = 0.785H^2 \ = \gamma_{cyl}H^2$$

with $\gamma_{cyl} = 0.785$. Thus, the effective area (γH^2) influencing the added mass is about two times larger for cilia (γ in Eq. 2.39) when compared to a cylinder with $2\gamma_{cyl} = 1.57$. This increase in the effective area for the cilia is anticipated since a thin rectangle of height H (with sharp edges) is expected to influence a larger fluid area when compared to a relatively smoother cylinder of cross-sectional diameter H.

Beam density and the added-mass effect

The added-mass effect captured by the added-mass coefficient $C_m = 7.42$ (in Eq. 2.34) depends on the relative density of the fluid and the beam material as in Eq. 2.13. In the current experimental setup, the density of the PDMS cilia is close to the density of the liquid (water). In contrast if the density of the beam is substantially larger (e.g., for metal or silicon-nitride cilia) then the added-mass effect would be much smaller. Thus, the significant added-mass effect in reducing the natural frequency of the cilia arises because, in addition to the geometry effect (i.e., the rectangular cross section), the density of the cilia is low.

2.5.2 Added mass reduces resonance frequency

It is shown that the added-mass effect substantially reduces the natural frequency (and thereby, the resonant vibrational frequency) in liquid. Moreover, it is shown that this substantial reduction in resonant vibrational frequency cannot be due to the

damping effect alone. The resonant vibrational frequency is the frequency ω at which the magnitude of the transfer function in Eq. 2.2

$$\begin{aligned} |G(j\omega)| &= \left[\frac{(K-1)^2\omega^4 + 2(K-1)\omega^2\omega_n^2 + \omega_n^4 + 4(\zeta_2 - \zeta_1 K)^2\omega^2\omega_n^2}{\omega^4 + (4\zeta_2^2 - 2)\omega^2\omega_n^2 + \omega_n^4}\right]^{1/2} \\ &= \left[\frac{(K-1)^2(\frac{\omega}{\omega_n})^4 + 2[2\zeta_1^2K^2 + (1-4\zeta_1\zeta_2)K + 2\zeta_2^2 - 1](\frac{\omega}{\omega_n})^2 + 1}{(\frac{\omega}{\omega_n})^4 + (4\zeta_2^2 - 2)(\frac{\omega}{\omega_n})^2 + 1}\right]^{1/2} \end{aligned} \quad (2.40)$$

is maximum. The magnitude is maximized when its square is maximized, or rather at the normalized frequency $\bar{\omega}$ that satisfies

$$\frac{d|G(\bar{\omega})|^2}{d\bar{\omega}} = 2|G(\bar{\omega})|\frac{d|G(\bar{\omega})|}{d\bar{\omega}} = \frac{d}{d\bar{\omega}}\left(\frac{P\bar{\omega}^2 + Q\bar{\omega} + 1}{\bar{\omega}^2 + R\bar{\omega} + 1}\right) = 0 \quad (2.41)$$

where

$$\begin{aligned} \bar{\omega} &= (\tfrac{\omega}{\omega_n})^2 \\ P &= (K-1)^2 \\ Q &= 2[2\zeta_1^2K^2 + (1-4\zeta_1\zeta_2)K + 2\zeta_2^2 - 1] \\ R &= 4\zeta_2^2 - 2. \end{aligned} \quad (2.42)$$

The optimization condition in Eq. 2.41 is equivalent to

$$(PR - Q)\bar{\omega}^2 + 2(P-1)\bar{\omega} + Q - R = 0. \quad (2.43)$$

and the resonant vibrational frequency is given by

$$\bar{\omega}_r = \frac{\omega_r}{\omega_n} = \sqrt{\frac{(P-1) + \sqrt{(P-1)^2 - (Q-R)(PR-Q)}}{Q - PR}}\ . \quad (2.44)$$

The normalized resonant vibrational frequency $\bar{\omega}_r$ in Eq. 2.44 is shown in Figure 2.3. Note from this figure that the maximum reduction in the resonant vibrational frequency is about 10% of the natural frequency for damping ratios ζ_1, ζ_2 less than 0.5 [66] because

$$\bar{\omega}_r = \frac{\omega_r}{\omega_n} > 0.9\ . \quad (2.45)$$

Without the added-mass effect, the natural frequency in water $\omega^*_{n,w}$ would be the same as the natural frequency in air $\omega^*_{n,a}$, which in turn would equal ω^*_n in Eq. 2.35

$$\omega^*_{n,w} = \omega^*_{n,a} = \omega^*_n. \quad (2.46)$$

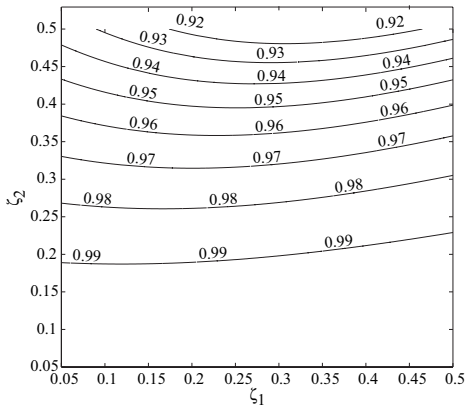

Figure 2.3: Contour plot for normalized resonant vibrational frequency $\bar{\omega}_r$ in Eq. 2.44.

Therefore, the reduction of the resonant vibrational frequency $\omega^*_{r,w}$ in water due to damping effect alone (without the added-mass effect) would not be significant — it would be less than 10% from Eq. 2.45, which predicts the resonant vibrational frequency (without added mass) to be

$$\omega^*_{r,w} > 0.9\omega^*_{n,w} = 0.9\omega^*_n \approx 0.9\omega_{n,a} = 0.9(338.68) = 304.81Hz. \tag{2.47}$$

from the approximation in Eq. 2.46. However, the observed natural frequency in water ($\omega_{n,w} = 116.7$Hz in Table 2.2) is substantially lower than the observed natural frequency in air ($\omega_{n,a} = 338.68$Hz in Table 2.1). This substantial reduction cannot be predicted by damping effects alone, without the added-mass effect. In contrast, the added-mass effect predicts a substantially lower natural frequency in water $\omega_{n,w}$ in comparison to the natural frequency in air $\omega_{n,a}$ — by a factor of κ

$$\kappa = \frac{1}{\sqrt{(1 + C_m)}} = 0.345 \tag{2.48}$$

as in Eq. 2.28 with C_m from Eq. 2.34. The further relatively-minor reduction of the resonant vibrational frequency in water ($\omega_{r,w} = 109.54$Hz in Table 2.2) in comparison to the natural frequency in water ($\omega_{n,w} = 116.7$Hz in Table 2.2) is the result of the damping effect as in Eq. 2.44. Therefore, the added mass (and not the damping) has

the dominant influence on the reduction of the natural frequency $\omega_{n,w}$, and therefore, on the reduction of the resonant vibrational frequency $\omega_{r,w}$ in liquid when compared to the natural frequency $\omega_{n,a}$ in air.

2.5.3 Added-mass effect on cilia with different lengths

To evaluate the model of the added-mass effect, predictions of the resonant vibrational frequency are comparatively evaluated against experimental results for cilia with different lengths. Cilia of different lengths were obtained by cutting the available, micro-fabricated 800μm cilia. Since the cilia depth D and height H are the same, the cut cilia have the same cross-sectional area, and therefore, the added-mass coefficient C_m (in Eq. 2.13) is expected to remain the same. Therefore, from Eqs. 2.24,2.28 the predicted natural frequency in water $\omega_{n,w}(L)$ for length L μm is related to the natural frequency in water (116.7Hz in Table 2.2) for length 800μm by

$$\omega_{n,w,p}(L) \ = 116.7 \left[\frac{800}{L}\right]^2 Hz. \tag{2.49}$$

Moreover, the predicted resonant vibrational frequency in water $\omega_{r,w,p}(L)$ for length L μm is obtained using the damping ratios for the 800μm cilia (in Table 2.2) in Eq. 2.44 along with the predicted natural frequency $\omega_{n,w,p}(L)$ from Eq. 2.49. The parameters of the experimentally obtained model (in Eq. 2.2), found by minimizing the least-squares-error between the predicted model response and measured frequency responses, are presented in Table 2.3. Moreover, the predictions (based on the 800μm cilia) and experimental values of the natural and resonant-vibrational frequencies are compared in Table 2.3, which shows that the model parameters from the 800μm cilia can be used to predict the natural frequency and resonant vibrational frequencies of the cut cilia to within 7.5% error where the error is defined as

$$E_{n,w} \ = \frac{(\omega_{n,w} - \omega_{n,w,p})}{\omega_{n,w}} \times 100, \qquad E_{r,w} \ = \frac{(\omega_{r,w} - \omega_{r,w,p})}{\omega_{r,w}} \times 100 \tag{2.50}$$

where the subscript p represents predicted values.

L (μm)	ζ_1	ζ_2	$\omega_{n,w}$ (Hz)	$\omega_{r,w}$ (Hz)	$\omega_{n,w,p}$ (Hz)	$E_{n,w}$ (%)	$\omega_{r,w,p}$ (Hz)	$E_{r,w}$ (%)
480	0.452	0.470	335.6	312.75	324.14	3.5	304.23	2.7
540	0.448	0.462	264.2	246.98	256.11	3.2	240.38	2.7
670	0.441	0.458	178.4	166.94	166.37	7.2	156.15	6.5
760	0.441	0.453	136.8	128.28	129.30	5.8	121.36	5.4
800	0.438	0.450	116.70	109.54	N/A	N/A	N/A	N/A

Table 2.3: Columns 2-5: experimental fit of the parameters in Eq. 2.2 for cilia with different lengths L actuated in DI water with $K = 1.566$. Columns 6-9: predicted natural frequencies $\omega_{n,w,p}$ and resonant vibrational frequencies $\omega_{r,w,p}$ using parameters for the 800μm cilia (in Table 2.2), and prediction errors $E_{n,w}, E_{r,w}$ as in Eq. 2.50. The predictions are not applicable (N/A) for the 800μm case.

The fluid damping ratio $\zeta_f = \zeta_1$ (see Eq. 2.33) is proportional to the square of the length L since it is inversely proportional to β_1^2 (see Eq. 2.29), where β_1 is inversely proportional to the length L (Eq. 2.24). However, the fluid damping ratio ζ_f is also proportional to the damping parameter B_f (in Eq. 2.29), which depends on the flow conditions such as flow velocities — flow velocities tend to be lower at the lower vibrational frequencies investigated with longer cilia. Hence the fluid damping ratio $\zeta_1 = \zeta_f$ is not expected to vary proportionally with the square of the cilia length L in Table 2.3.

2.5.4 Added mass increases the resonance amplitude

In addition to the reduction of the natural (and resonant vibrational) frequencies with the added-mass effect (as in Eq. 2.28), from Eqs. 2.29,2.30, the fluid and internal damping ratios ζ_f, ζ_i are also reduced by the same factor $\kappa = 0.345$ in Eq. 2.48. Therefore, the damping ratios ζ_f^*, ζ_i^* without the added-mass effect (denoted by the superscript $*$) tend to be about three times ($1/\kappa = 2.898$ times) larger when com-

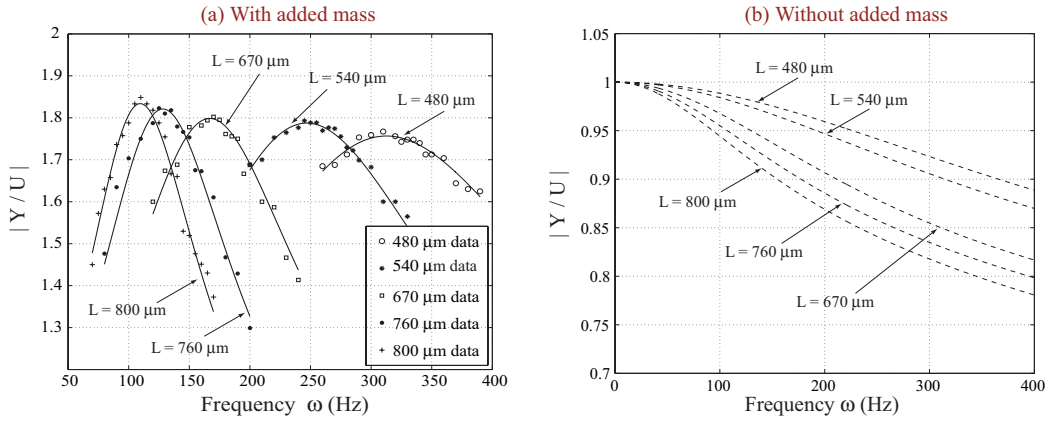

Figure 2.4: Frequency response prediction in water for models of cilia (with different lengths): (a) with the added-mass effect (solid lines); and (b) without the added-mass effect (dashed lines). Experimentally measured data points are shown in the left plot.

pared to the case with the added-mass effect. In particular, for the 800µm cilia the damping ratios ζ_1^*, ζ_2^* without the added-mass effect are estimated to be (from Eqs. 2.29,2.30,2.33)

$$\zeta_1^* = \zeta_f^* = \frac{\zeta_f}{\kappa} = \frac{\zeta_1}{\kappa} = \frac{0.438}{0.345} = 1.27 \tag{2.51}$$

$$\zeta_2^* = \zeta_i^* + \zeta_f^* = \frac{(\zeta_i + \zeta_f)}{\kappa} = \frac{\zeta_2}{\kappa} = \frac{0.45}{0.345} = 1.3\ . \tag{2.52}$$

The added-mass effect effectively decreases the damping ratio (when compared to the model without the added mass), and thereby, increases the vibrational response at the resonance. In particular, without the added-mass effect, the system is overdamped with damping ratio greater than one (i.e., $\zeta_2^* = 1.3$) — the maximum expected amplitude of vibration is then one (i.e., the same as the applied base motion). In contrast, with the added-mass effect, the system is underdamped with damping ratio less than one (i.e., $\zeta_2 = 0.45$) — the ensuing maximum amplitude at resonance is expected to be greater than one. This increase in the amplitude at the resonance frequency with the added-mass effect is seen in Figure 2.4, which compares the models with and without the added-mass effect for different cilia lengths. Note that the model with

the added-mass effect captures the experimental data well as opposed to the model without the added mass (that predicts an overdamped system). Thus, the added-mass effect is needed in the model to capture both (i) the substantial reduction of the resonant vibrational frequency of the cilia in liquid when compared to air; and (ii) the relatively large amplitude at resonance even in the presence of substantial fluid damping due to an effective reduction in the damping ratio.

2.6 Conclusions

This chapter showed that the added-mass, due to fluid-structure interaction, significantly affects the vibrational dynamics of cilia-based (vibrating cantilever-type) devices proposed for handling micro/nano-scale fluid flows. Furthermore, it showed that damping effects of the hydrodynamic interaction between the cilia-based actuators and fluid cannot fully explain the substantial reduction (by about a third) in the resonant frequency of the cilia actuators in liquid when compared to the natural frequency in air. The work showed that an added-mass effect explains (i) this reduction in the resonant frequency due to an increase in the effective inertia; as well as (ii) the relatively large amplitude at resonance, even in the presence of substantial fluid damping, due to an effective reduction in the damping ratio.

Chapter 3

DYNAMICS OF CILIA-BASED MICROFLUIDIC DEVICES

3.1 Overview

This chapter models the dynamics of cilia-based devices (soft cantilever-type, vibrating devices that are excited by external vibrations) for mixing and manipulating liquids in microfluidic applications. The main contribution of this chapter is to develop a model, which shows that liquid sloshing and the added mass effect play substantial roles in generating large-amplitude motion of the cilia. Additionally, experimental mixing results, with and without cilia, are comparatively evaluated to show more than an order-of-magnitude reduction in the mixing time with the use of cilia.

3.2 Introduction

This chapter models the dynamics of cilia-based devices (soft cantilever-type vibrating devices that are excited by external vibrations) for mixing and manipulating liquids in microfluidic applications. The behavior of biological cilia, discovered by Anton de Heide in 1684 [38], has been studied in, e.g., [38]- [43]. Bio-mimetic, cilia-like structures have been proposed for a variety of applications such as nasal filters [44] and sample transport [45]. In microfluidics, bio-mimetic actuators have been proposed for mixing and manipulation in liquid environments [46]- [50]. The main contribution of this chapter is to develop a model for a cilia-based device, which shows that liquid

sloshing (e.g., [51, 52]) and the added mass effect (e.g., [53]- [56]) play substantial roles in generating large-amplitude motion of the cilia in liquid when the chamber containing the cilia is oscillated to mechanically excite the cilia resonance. Additionally, experimental results are presented to show that the average mixing time with cilia is more than an order-of-magnitude lower than the average mixing time without cilia.

Mixing can be improved by generating complex flows in the fluid to overcome the mixing-rate limits of laminar flows that are typical at the micro scale. For example, passive techniques such as channels with patterned grooves can be used to generate chaotic folding (and refolding) of the liquid as it flows past the grooves to improve mixing [12]. Such flow-type mixing can be used when a sufficiently-large amount of sample is available to achieve the flow through the grooved channel. In contrast, if the amount of sample is limited, then batch-type mixing is sought in small chambers containing the sample. Batch mixing can be enhanced using a variety of actuation techniques such as high-frequency ultrasound excitation [13, 57] and time-varying external magnetic fields [15], [21]- [59]. In the current work, cilia are excited by low-frequency oscillations (compared to higher-frequency acoustic excitation) of the chamber containing the sample. This low-frequency mechanical excitation of cilia is advantageous for mixing samples that are susceptible to damage from high-frequency excitation and magnetic fields. The current chapter shows that batch mixing can be substantially improved by using cilia when compared to the case without cilia — for the same oscillatory actuation of the chamber.

The main contribution of the chapter is to develop a model that explains the large-amplitude cilia motion in the liquid. In general, it is difficult to generate large amplitude motion of cilia-type devices in the presence of substantial fluid damping [37, 66]. For example, the damping ratio ζ in liquid tends to be in the range of 0.05 to 0.5 [66], which leads to a small (1.7 to 1.9) amplification factor (i.e., ratio of the

cilia-tip motion to the excitation of the chamber) at the vibrational resonance of cilia. The current work shows that sloshing in the chambers containing the cilia can be exploited to achieve large (3 to 4) amplification factors. Previous work has shown that the sloshing phenomena, which is well studied in literature for large-scale systems (e.g., [51, 52]), is also important in microsystems [75]. In the current chapter, such sloshing models are used to explain the large-amplitude motion of cilia observed in the experiments.

The proposed model is used to show that the added-mass effect in fluid-structure interactions should be considered to capture the excitation of the cilia resonance by the sloshing. It is noted that the added-mass effect is important in other applications such as underwater vehicles [71] and atomic force microscopy [66], and was introduced in early works on pendulum oscillations initiated by Dubuat — an early history of the added mass by Stokes can be found in [53]. In cilia-based devices, the added mass has been shown to reduce the resonance frequency of the cilia in liquid when compared to cilia in air [1]. The current chapter shows that the lowering of the cilia's vibrational frequency to be close to the sloshing resonance frequency of the chamber results in increased excitation of the cilia resonance by the sloshing. Thereby, the added mass effect plays a significant role in achieving large-amplitude, cilia motion.

3.3 Modeling the Cilia Dynamics

3.3.1 System Description

The displacement along the length (x) of a cilium is excited by the motion ($u_b(t)$) of the cilia base by using a piezoactuator (Burleigh PZS200) as shown in Figure 3.1. The soft cilia are fabricated from polydimethylsiloxane (PDMS) using a silicon mold. Detailed information on cilia fabrication and material properties can be found in [32]. The nominal dimensions of the silicon mold used to fabricate the cilia used in the experiments are length ($L = 800\mu$m), height ($H = 45\mu$m), and depth ($D = 10\mu$m).

An oscillatory motion

$$u_c(t) = Asin(\omega t)$$

of the chamber containing the cilia is achieved by using a piezoactuator as shown in Figure 3.1 where A and ω are the amplitude and the frequency of the oscillation respectively. The input $u_b(t)$ of the system is the motion of the base of the cilia, which is the same as the oscillatory motion of the chamber because the cilia base is attached to the chamber with a relatively stiff structure, i.e.,

$$u_b(t) = u_c(t).$$

The output of the system is the motion

$$y(t) = \hat{y}(L, t),$$

of the cilia tip, i.e., at the free end with $x = L$, as shown in Figure 3.1(c).

The input (cilia-base motion $u_b(t)$) and the output (cilia-tip motion $y(t)$) are observed by using an optical microscope with an attached digital color charge-coupled-device (CCD) camera and the displacement amplitude of the vibrating cilia is measured using captured still images (Pinnacle Studio Version 12). A typical image of the resulting cilia vibration (due to the chamber oscillation) is shown in Figure 3.1(b).

3.3.2 Euler-Bernoulli Model of Cilia Vibration

The Euler-Bernoulli beam approach, e.g., [73] is used to model the vibrational response of the cantilever-type cilia device — such standard beam theory has been used in the past to model the dynamics of micro-scale cantilevers in liquid [1, 37, 66]. In particular, the dynamics of the net motion $\hat{y}(x, t)$ of a vibrating cilium (beam) is given by

$$\rho_b A_b \frac{\partial^2 \hat{y}(x,t)}{\partial t^2} + EI \frac{\partial^4 \hat{y}(x,t)}{\partial x^4} = f(x,t) \tag{3.1}$$

where the subscript b represents a property of the beam, ρ_b is the mass density, $A_b = DH$ is the cross sectional area, E is the Young's modulus, and $I = HD^3/12$ is

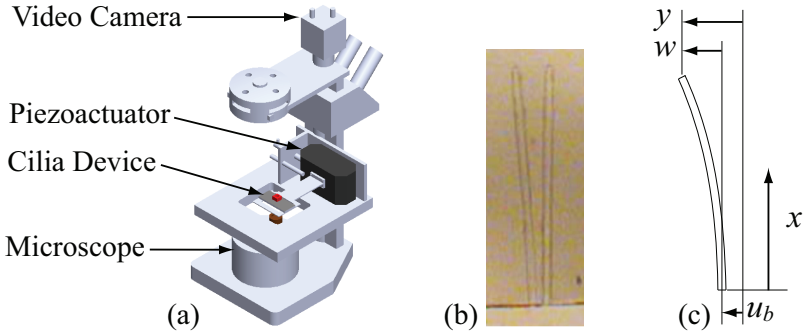

Figure 3.1: Schematics of experiment for evaluating the frequency response of cilia. (a) Experimental setup. (b) Image of a cilium in water excited by the piezoactuator. (c) Input $u_b(t)$ and output $y(t)$ motions of the cilium.

the area moment of inertia. The net motion $\hat{y}(x,t)$ is composed of the base motion, i.e., the input $u_b(t)$, and the elastic deflection, $\hat{w}(x,t)$ of the cilium (beam)

$$\hat{y}(x,t) \ = \hat{w}(x,t) + u_b(t) \tag{3.2}$$

as illustrated in Figure 3.1(c), and standard cantilever boundary conditions:

$$\hat{w}(0,t) = 0, \quad \frac{\partial \hat{w}(0,t)}{\partial x} = 0, \quad \frac{\partial^2 \hat{w}(L,t)}{\partial x^2} = 0, \quad \frac{\partial^3 \hat{w}(L,t)}{\partial x^3} = 0. \tag{3.3}$$

The first term on the left hand side of Eq. (3.1) represents the inertial effects, the second term on the left hand side of Eq. (3.1) represents the elastic effects and $f(x,t)$ (on the right hand side) represents the total external force (per unit length) on the cilium. The external forces acting on the cilium are described next.

External Forces

The external force f acting on the cilium (in Eq. 3.1) has four parts: (i) the drag (friction) force f_f between the cilium and the fluid; (ii) the internal damping force f_i; (iii) the inertial load f_m due to the added mass effect; and (iv) the buoyancy-like

force f_b due to the fluid acceleration

$$f(x,t) = f_f(x,t) + f_i(x,t) + f_m(x,t) + f_b(x,t). \tag{3.4}$$

Drag Force The first term in Eq. (3.4), the distributed drag force f_f due to hydrodynamic interaction, depends on the relative velocity between the structure and the fluid; it is approximated as (similar to [35, 36])

$$f_f(x,t) = -B_f \left[\frac{\partial \hat{y}(x,t)}{\partial t} - \dot{u}_f \right] = -B_f \left[\frac{\partial \hat{w}(x,t)}{\partial t} + \dot{u}_b - \dot{u}_f \right] \tag{3.5}$$

where B_f is the fluid damping parameter that depends on the flow conditions, and $\dot{u}_f$ is the fluid velocity.

Internal Damping The second term in Eq. (3.4), the internal damping force f_i, depends on the rate of change of the beam's elastic deflection and is described by

$$f_i(x,t) = -B_i \left[\frac{\partial \hat{w}(x,t)}{\partial t} \right] \tag{3.6}$$

where B_i is the internal damping parameter that depends on the beam properties.

Inertial Loading The third term in Eq. (3.4), the inertial load f_m, arises because of the need to accelerate the fluid around an object when the object is accelerated through a fluid [53]- [56]. The inertia of the fluid exerts a resistive force on the object; this resistive force is termed as the *added-mass effect* because the object responds as if its mass has increased. This added-mass effect can be modeled as an inertial forcing term (f_m) that depends on the relative acceleration between the beam and the fluid as

$$\begin{aligned} f_m(x,t) &= -\rho_f A_f \left[\frac{\partial^2 \hat{y}(x,t)}{\partial t^2} - \ddot{u}_f(t) \right] \\ &= -\rho_f A_f \left[\frac{\partial^2 \hat{w}(x,t)}{\partial t^2} + \ddot{u}_b(t) - \ddot{u}_f(t) \right] \end{aligned} \tag{3.7}$$

where A_f is the effective hydrodynamic area of the fluid that affects the inertial force f_m (per unit length) and ρ_f is the fluid density. The hydrodynamic mass $\rho_f A_f$ of the fluid (per unit length) that affects the inertial loading can be described in terms of the corresponding beam mass $\rho_b A_b$ (per unit length) in terms of an added-mass coefficient C_m as [1]

$$\rho_f A_f = C_m \rho_b A_b. \tag{3.8}$$

Thus, the the inertial load f_m (in Eq. 3.7) can be rewritten in terms of the added-mass coefficient C_m by using Eq. (3.8) as

$$f_m(x,t) = \quad = -C_m \rho_b A_b \left[\frac{\partial^2 \hat{w}(x,t)}{\partial t^2} + \ddot{u}_b(t) - \ddot{u}_f(t) \right] \tag{3.9}$$

Buoyancy-Like Force The last term in Eq. (3.4), f_b, called the buoyancy force in [76] (chapter 6, page 120) is also referred to as the Froude-Krylov force in [74] (chapter 4, page 131). This force arises due to the pressure gradient P' across the depth D of the cilium due to the fluid acceleration $\ddot{u}_f(t)$ which is given by

$$P' \quad = \quad -\rho_f \ddot{u}_f(t). \tag{3.10}$$

This pressure gradient results in a difference in forces acting on the cilium due to the variations in the pressure P as shown in Figure 3.2 for a small length L_b of the cilium — this is similar to the net buoyancy force due to the standard gravity-related pressure gradient.

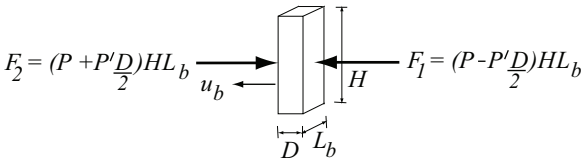

Figure 3.2: Pressure gradient due to accelerating fluid generates buoyancy-like force across the thickness of a cilium.

The resulting force (per unit length) acting on the cilium is given by

$$\begin{aligned} f_b(x,t) &= \frac{F_1 - F_2}{L_b} = \frac{(P - P'D/2)HL_b - (P + P'D/2)HL_b}{L_b} \\ &= -P'DH \quad = -P'A_b \\ &= \rho_f A_b \ddot{u}_f(t). \end{aligned} \tag{3.11}$$

Substituting the different terms in the external force f (Eq. 3.4) into the the Euler-Bernoulli equation for the cilium dynamics (Eq. 3.1) — i.e., the drag (friction) force f_f from Eq. (3.5), the internal damping force f_i from Eq. (3.6), the inertial load f_m from Eq. (3.9) and the buoyancy-like force f_b from Eq. (3.11) — and then collecting similar terms in the cilium deflection w, input u_b and fluid motion u_f leads to

$$\frac{\partial^2 \hat{w}(x,t)}{\partial t^2} + \frac{(B_f + B_i)}{\rho_b A_b (1 + C_m)} \frac{\partial \hat{w}(x,t)}{\partial t} + \frac{EI}{\rho_b A_b (1 + C_m)} \frac{\partial^4 \hat{w}(x,t)}{\partial x^4} = r(t) \tag{3.12}$$

with the forcing term $r(t)$ given by

$$r(t) = -\ddot{u}_b(t) - \frac{B_f}{\rho_b A_b (1 + C_m)} \dot{u}_b(t) + \frac{\rho_b C_m + \rho_f}{\rho_b (1 + C_m)} \ddot{u}_f(t) + \frac{B_f}{\rho_b A_b (1 + C_m)} \dot{u}_f(t). \tag{3.13}$$

The First Vibrational Mode

As in previous models of vibrating micro-scale cantilevers in liquid [1,37,66], the main dynamics can be captured through the first vibrational mode of the cilium. Towards this, the cilium deflection $\hat{w}$ is split into its modal components, with separated spatial X and temporal T parts, as

$$\hat{w}(x,t) = \sum_{n=1}^{\infty} X_n(x) T_n(t) \tag{3.14}$$

and substituted into Eq. (3.12) to obtain

$$\sum_{n=1}^{\infty} X_n(x) \ddot{T}_n(t) + \frac{(B_f + B_i)}{\rho_b A_b (1 + C_m)} \sum_{n=1}^{\infty} X_n(x) \dot{T}_n(t) + \frac{EI}{\rho_b A_b (1 + C_m)} \sum_{n=1}^{\infty} X_n''''(x) T_n(t) = r(t). \tag{3.15}$$

Note that $X_n(x)$ represents the shape of the nth vibrational mode, which is obtained by considering the homogeneous equation with $r(t) = 0$ in Eq. (3.15). The homogeneous equation is satisfied if each mode satisfies

$$X_n(x)\ddot{T}_n(t) + \frac{(B_f + B_i)}{\rho_b A_b (1 + C_m)} X_n(x)\dot{T}_n(t) + \frac{EI}{\rho_b A_b (1 + C_m)} X_n''''(x) T_n(t) = 0 \quad (3.16)$$

which can be re-written as a spatial (position x dependent) function on one side and a temporal (time t dependent) function on the other side that are, hence, both equal to a constant $(-z_n^2)$, i.e.,

$$\frac{\ddot{T}_n(t)}{T_n(t)} + \frac{(B_f + B_i)}{\rho_b A_b (1 + C_m)} \frac{\dot{T}_n(t)}{T_n(t)} = -\frac{EI}{\rho_b A_b (1 + C_m)} \frac{X_n''''(x)}{X_n(x)} = -z_n^2.$$

This yields two equations for the spatial X_n and temporal T_n portions of the mode

$$\ddot{T}_n(t) + \frac{(B_f + B_i)}{\rho_b A_b (1 + C_m)} \dot{T}_n(t) + z_n^2 T_n(t) = 0 \quad (3.17)$$

$$X_n''''(x) - \frac{\rho_b A_b (1 + C_m)}{EI} z_n^2 X_n(x) = 0. \quad (3.18)$$

The mode shape X_n can be obtained from Eq. (3.18) as [73]

$$X_n(x) = \cosh(\beta_n x) - \cos(\beta_n x) - \sigma_n(\sinh(\beta_n x) - \sin(\beta_n x)) \quad (3.19)$$

where

$$X_n''''(x) = \beta_n^4 X_n(x) \quad (3.20)$$

$$\beta_n = \left[\frac{\rho_b A_b (1 + C_m)}{EI} z_n^2\right]^{1/4}. \quad (3.21)$$

For the first mode ($n = 1$) of vibration, the parameters in the mode shape ($X_1(x)$ in Eq. 3.19) can be found from the boundary conditions (in Eq. 3.3) as [73]

$$\beta_1 L = 1.875 \quad \text{and} \quad \sigma_1 = 0.7341 \quad \text{with} \quad X_1(L) = 2. \quad (3.22)$$

Multiplying the non-homogeneous Eq. (3.15) with the first mode $X_1(x)$, using the the mode shape property in Eq. (3.20) and integrating with respect to the length dx

results in

$$\sum_{n=1}^{\infty}\int_0^L X_1(x)X_n(x)dx\ddot{T}_n(t)+\frac{(B_f+B_i)}{\rho_b A_b\,(1+C_m)}\sum_{n=1}^{\infty}\int_0^L X_1(x)X_n(x)dx\dot{T}_n(t)+$$
$$\frac{EI}{\rho_b A_b\,(1+C_m)}\sum_{n=1}^{\infty}\int_0^L \beta_n^4 X_1(x)X_n(x)dxT_n(t)=r(t)\int_0^L X_1(x)dx.$$

The orthogonality of the mode shapes results in only the first mode remaining after the integration in the above equation to yield

$$\ddot{T}_1(t)+\frac{(B_f+B_i)}{\rho_b A_b\,(1+C_m)}\dot{T}_1(t)+\frac{EI}{\rho_b A_b\,(1+C_m)}\beta_1^4 T_1(t)=r(t)K_1 \tag{3.23}$$

$$K_1=\frac{\int_0^L X_1(x)dx}{\int_0^L X_1(x)X_1(x)dx}=\frac{0.783L}{L}=0.783 \tag{3.24}$$

which can be rewritten (using the forcing term r from Eq. 3.13) as

$$\ddot{T}_1(t)+2(\zeta_f+\zeta_i)\omega_n\dot{T}_1(t)+\omega_n^2 T_1(t)=0.783r(t) \tag{3.25}$$

where the natural frequency ω_n, fluid damping ratio ζ_f and internal damping ratio ζ_i are given by

$$\omega_n = \left[\beta_1^2\sqrt{\frac{EI}{\rho_b A_b}}\right]\frac{1}{\sqrt{(1+C_m)}} = \frac{\omega_n^*}{\sqrt{(1+C_m)}} \tag{3.26}$$

$$\zeta_f = \frac{1}{2\omega_n}\left[\frac{B_f}{\rho_b A_b\,(1+C_m)}\right] = \frac{B_f}{2\beta_1^2\sqrt{EI\rho_b A_b}}\frac{1}{\sqrt{(1+C_m)}} = \frac{\zeta_f^*}{\sqrt{(1+C_m)}} \tag{3.27}$$

$$\zeta_i = \frac{1}{2\omega_n}\left[\frac{B_i}{\rho_b A_b\,(1+C_m)}\right] = \frac{B_i}{2\beta_1^2\sqrt{EI\rho_b A_b}}\frac{1}{\sqrt{(1+C_m)}} = \frac{\zeta_i^*}{\sqrt{(1+C_m)}} \tag{3.28}$$

where $\omega_n^*, \zeta_f^*, \zeta_i^*$ are the natural frequency, fluid damping ratio, and internal damping ratio, respectively, without the added-mass effect. Moreover, the output tip displacement, due to the first vibrational mode X_1 and the base motion $u_b(t)$ is

$$y(t)=X_1(L)T_1(t)+u_b(t) = 2T_1(t)+u_b(t). \tag{3.29}$$

since $X_1(L)=2$ (as in Eq. 3.22).

3.3.3 Effect of Sloshing on Cilia Vibration

The effect of the external forcing (chamber oscillation) on the cilia vibration consists of two parts: (i) the direct forcing due to the motion of the chamber (or cilia base u_b) and (ii) the forcing due to fluid motion u_f, which can be different from the chamber/base motion u_b because of fluid sloshing. In particular, these two components (u_b and u_f) arise in the forcing term $r(t)$ (Eq. 3.13) and, thereby, appear on the right hand side of the cilium vibration Eq. (3.25), which can be rewritten in the frequency domain as

$$\begin{aligned}\left[s^2 + 2\zeta_2\omega_n s + \omega_n^2\right] T_1(s) &= 0.783 r(s) \\ &= -0.783\left[s^2 + 2\zeta_1\omega_n s\right] u_b(s) \\ &\quad + 0.783\left[\frac{\rho_b C_m + \rho_f}{\rho_b\left(1 + C_m\right)} s^2 + 2\zeta_1\omega_n s\right] u_f(s). \quad (3.30)\end{aligned}$$

where $\zeta_1 = \zeta_f$, and $\zeta_2 = \zeta_f + \zeta_i$. If the chamber motion and the accompanying sloshing amplitude are not too large, then the additional motion of the fluid u_f over the motion of the chamber u_b can be captured using linear models, e.g., [52, 77] such as a second-order model of the form [52]

$$\begin{aligned}u_f(s) &= \frac{-K_{sl} s^2}{s^2 + 2\omega_{sl}\zeta_{sl} s + \omega_{sl}^2} u_b(s) \quad + u_b(s) \quad (3.31) \\ &= \left[G_{sl}(s) + 1\right] u_b(s) \quad (3.32)\end{aligned}$$

where G_{sl} is the sloshing transfer function that quantifies the additional motion u_f of the fluid (at the level of the cilia in the chamber) over the motion u_b of the chamber, and $K_{sl}, \zeta_{sl}, \omega_{sl}$ are the gain, damping ratio, and natural frequency of sloshing in the chamber, respectively. These parameters depend on the fluid properties, the geometry of the chamber and the height of the cilia location from the base of the chamber.

Note that if there is no sloshing, then displacement of the fluid u_f is equal to that of the chamber u_b. In that case, the sloshing gain K_{sl} is zero, e.g., at the base of the

chamber. Similarly, at a low frequency, ω the amplification factor, $|G_{sl}|_{s=j\omega}$ of the sloshing transfer function G_{sl} tends to be small due to the s^2 term in the numerator and the fluid motion u_f becomes close to the chamber motion u_b.

Transfer Function Model

The vibrational response of the cilium's tip y (in Eq. 3.29) can be rewritten using the sloshing dynamics (in Eq. 3.32) and the cilium vibrational model (in Eq. 3.30) as

$$\frac{y(s)}{u_b(s)} = G_y(s) = 2\frac{T_1(s)}{u_b(s)} + 1 \tag{3.33}$$

$$= G_1(s) + G_{sl}(s)G_2(s) + 1 \tag{3.34}$$

where

$$G_1(s) = 1.566\frac{\frac{(\rho_f-\rho_b)}{\rho_b(1+C_m)}s^2}{s^2 + 2\zeta_2\omega_n s + \omega_n^2} \tag{3.35}$$

$$G_2(s) = 1.566\frac{\frac{\rho_b C_m+\rho_f}{\rho_b(1+C_m)}s^2 + 2\zeta_1\omega_n s}{s^2 + 2\zeta_2\omega_n s + \omega_n^2}. \tag{3.36}$$

This completes the theoretical modeling of the cilia-motion dynamics.

3.4 Experimental Results and Discussions

Experimental data in this section is used to highlight the need to capture the added-mass effect and the sloshing effect in the theoretical model developed in the previous section. Additionally, issues that affect the amplitude of cilia motion, such as the liquid height and cilia length, are investigated experimentally. Finally, it is shown that cilia can be used to achieve faster mixing by comparing mixing results with and without cilia.

3.4.1 Added-Mass and Sloshing Effects on Cilia Response

The following experimental results show the importance of including both, the added mass effect and the sloshing effect to capture the frequency response of the cilia. Towards this, the frequency responses of cilia are comparatively evaluated for three cases as illustrated in Figure 3.3. In the first case (a), the cilia are oscillated in air as in Figure 3.3(a). In the second case (b), the same cilia (as in case a) are oscillated in de-ionized (DI) water to comparatively evaluate the effect of moving the cilia in a dense fluid (water) instead of air. In this second case, the chamber containing the water is stationary — therefore, sloshing is not present. In the final case (c), the entire chamber is oscillated (which leads to liquid sloshing) to comparatively evaluate the cilia dynamics with and without sloshing. All the cilia in the three sets of experiments have identical dimensions.

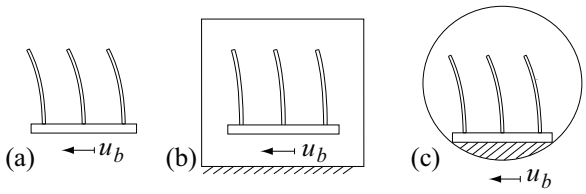

Figure 3.3: Schematic experimental setup (images not to scale) for evaluating the effects of added mass and sloshing on the frequency response of cilia. Case (a) the cilia are oscillated in air; case (b) the cilia are oscillated in water (inside a stationary, relatively-large 60mm×115mm chamber); and case (c) the chamber (3mm diameter) containing the cilia is oscillated. In each case, three cilia are used.

Experimental Frequency Response Data

The frequency response of the cilia dynamics is obtained by varying the frequency of oscillation. The amplitude of the piezoactuator's motion, which generates cilia oscillation (in cases a and b) and the chamber/cilia oscillation (in case c), is kept fixed at 10μm for all the three sets of experiments. The amplitudes of the cilia-tip

motion y and the cilia-base motion u_b are measured from images obtained from the video camera. The experimentally obtained frequency responses for the three cases are shown in Figure 3.4. Each data point in these figures represents the average amplification, of the cilia motion y over the base motion u_b, of the three cilia in each experimental run.

Model Parameters for Cases (a) and (b)

When the cilia are oscillated in a stationary fluid (as in cases a and b), the nominal velocity of the fluid is set to zero ($u_f = 0$ in Eq. 3.30) and the system transfer G_y^* becomes, from Eqs. (3.30,3.33)

$$\frac{y(s)}{u_b(s)} = G_y^*(s) = 2\frac{T_1(s)}{u_b(s)} + 1 = -1.566\frac{s^2 + 2\zeta_{1,i}\omega_{n,i}s}{s^2 + 2\zeta_{2,i}\omega_{n,i}s + \omega_{n,i}^2} + 1 \quad (3.37)$$

where the subscript i is either a or b to denote the two cases (a or b). The model parameters (damping $\zeta_{1,i}, \zeta_{2,i}$ and natural frequency $\omega_{n,i}$) for cilia oscillated in air (case a, $i = a$) and in water (case b, $i = b$) were obtained by minimizing the least-square of the error between the experimental and predicted frequency responses for each cilium. The parameters obtained through this fit of the experimental data are provided in Table 3.1 for case (a) and in Table 3.2 for case (b). It is noted that the parameters (in Tables 3.1, 3.2) are similar for the different cilia in each experimental run. The resulting frequency responses predicted by the models (using the mean values in Tables 3.1, 3.2 for cases a and b) are shown in Figure 3.4.

Effect of Added Mass on Frequency Response of Cilia

The added-mass effect leads to a substantial reduction in the resonant-vibrational frequency in water, $\omega_{r,b}$ when compared to air (for the same set of three cilia) as seen in Figure 3.4 and in Tables 3.1 and 3.2. In particular, the mean, resonant-vibrational frequency in water $\omega_{r,b} = 110.14$Hz (Table 3.2) is substantially lower than the mean resonant-vibrational frequency in air $\omega_{r,a} = 334.13$Hz (Table 3.1). Damping

Case (a)	$\zeta_{1,a}$	$\zeta_{2,a}$	$\omega_{n,a}$ (Hz)	$\omega_{r,a}$ (Hz)
Cilium 1	0.149	0.166	335.84	333.27
Cilium 2	0.149	0.165	338.11	335.52
Cilium 3	0.151	0.167	336.26	333.61
Mean	0.150	0.166	336.74	334.13

Table 3.1: Parameters for three cilia (length $L = 800\mu$m) actuated in air, i.e., case (a), with the transfer function given in Eq. (3.37). The resonance frequency of the fitted model is $\omega_{r,a}$.

effects (in water as opposed to air) cannot explain the substantial reduction in the resonant-vibrational frequency of the cilia oscillated in water when compared to the cilia oscillated in air. For example, a standard second-order model for cantilever structures would yield a resonant-vibrational frequency expression of

$$\omega_{r,w} = \omega_{n,a}\sqrt{1 - 2\zeta^2} \tag{3.38}$$

where ζ is the damping ratio (e.g., see [70], Section 10.8). With a damping ratio ζ in water ranging from 0.05 to 0.5 (e.g., [66]), the anticipated, resonant-vibrational frequency $\omega_{r,b}$ in a water is expected to be between $0.997\omega_{n,a} = 335.73$Hz to $0.707\omega_{n,a} = 238.08$Hz from Eq. (3.38). Note that this range for the anticipated, resonant-vibrational frequency (from 238.08Hz to 335.73Hz) is much larger than the mean, resonant-vibrational frequency in water from experiments of $\omega_{r,b} = 110.14$Hz (Table 3.2). Thus, damping alone is not sufficient to capture the substantial reduction in the resonant vibrational frequency of cilia actuators when oscillated in liquids when compared to oscillation in air.

The added-mass effect (that accounts for the inertial loading of the fluid) can account for the substantial reduction in the resonant vibrational frequency when operating cantilever-type devices in liquids [1]. Note that the mean, natural frequency in water $\omega_{n,b} = 117.40$Hz (Table 3.2) is substantially lower than the mean, natural frequency

Case (b)	$\zeta_{1,b}$	$\zeta_{2,b}$	$\omega_{n,b}$ (Hz)	$\omega_{r,b}$(Hz)
Cilium 1	0.441	0.457	115.08	107.74
Cilium 2	0.442	0.451	120.16	112.80
Cilium 3	0.432	0.446	116.95	109.87
Mean	0.438	0.451	117.40	110.14

Table 3.2: Parameters for three cilia (the same cilia as in Table 3.1 in air) actuated in water, i.e., case (b), with the transfer function given in Eq. (3.37). The resonance frequency of the fitted model is $\omega_{r,b}$.

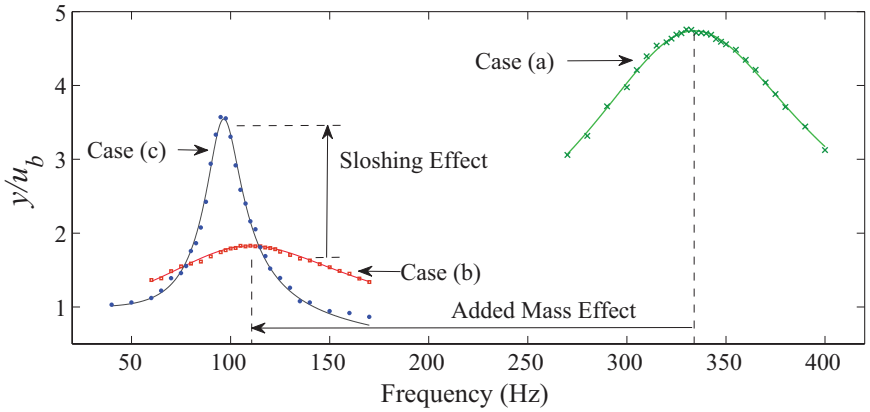

Figure 3.4: Frequency responses for three cases. The frequency responses of the fitted models are shown using solid lines, and experimental mean values (for three cilia in each case) are represented by dots. Case (a) the cilia are oscillated air; case (b) the cilia are oscillated in water (inside a stationary chamber); and case (c) the chamber containing the cilia is oscillated. The same set of cilia is used in case (a) and case (b) to capture the added mass effect. The estimated added mass is used to model the cilia response with sloshing in case (c).

in air $\omega_{n,a} = 336.74$Hz (Table 3.1). The natural frequency should not be affected by the fluid damping, and can be used to estimate the added-mass coefficient C_m from Eq. (3.26) as

$$C_m = \left[\frac{{\omega_n^*}^2}{{\omega_{n,b}}^2} - 1\right] \approx \left[\frac{{\omega_{n,a}}^2}{{\omega_{n,b}}^2} - 1\right] = \left[\frac{336.74^2}{117.40^2} - 1\right] = 7.23 \tag{3.39}$$

where the added mass effect in air (which has low density compared to water) is neglected. By increasing the effective mass (due to the need to accelerate the surrounding fluid), the model with the added mass has a substantially lower natural frequency (as in Eq. 3.26), and thereby, captures the substantially lower resonant-vibrational frequency [1]. This value 7.23 for the added-mass coefficient is used in the rest of the chapter since all cilia, used in the experiments, are made from the same silicon mold using the same fabrication procedures.

Effect of Sloshing on Frequency Response of Cilia

The model parameters (in Eq. 3.31) for the liquid sloshing, obtained by minimizing the least-square of the error between the model's predicted frequency response and the mean experimental frequency response in Figure 3.4, are given by

$$K_{sl} = 0.489, \quad \zeta_{sl} = 0.095, \quad \omega_{sl} = 96.63\text{Hz}. \tag{3.40}$$

When finding the sloshing parameters, the cilia-related terms (G_1, G_2) in the dynamics G_y (Eq. 3.34) were kept the same as the mean values for case (b) in Table 3.2 when the cilia were oscillated in a stationary chamber, i.e.,

$$\zeta_1 = 0.438, \quad \zeta_2 = 0.451, \quad \omega_n = 117.40\text{Hz}, \quad C_m = 7.23. \tag{3.41}$$

Moreover, the density of the water is $\rho_f = 1000\text{kg/m}^3$ and the density of the PDMS cilium is $\rho_b = 950\text{kg/m}^3$. The resulting frequency response predicted by the model for case (c) with the parameters in Eqs. (3.40, 3.41) is shown in Figure 3.4. It is noted that there is a substantial increase in the cilia motion with sloshing (i.e., when the chamber is oscillated) when compared to the case (b) when the chamber is stationary.

To summarize, both, the sloshing effect and the added mass effect are important when modeling the cilia dynamics — the added mass reduces the natural frequency ω_n of the cilia vibration (compare case a and case b in Figure 3.4) and sloshing increases the amplitude of cilia motion (compare case b and case c in Figure 3.4).

3.4.2 Experimental Study of Sloshing Dynamics

The importance of sloshing dynamics to achieve large amplitude cilia motion is studied in this subsection by comparatively evaluating the cilia motion with and without sloshing for the oscillating chamber (case c). Additionally, the effect of liquid height on the sloshing dynamics (and therefore the cilia motion) is experimentally investigated.

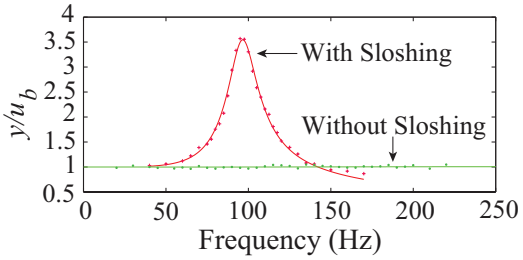

Figure 3.5: Experimental frequency responses (mean value of three cilia) with and without sloshing, i.e., free surface is constrained from sloshing with a glass cover. The same set of three cilia were used for both experiments, with and without sloshing.

Response with and without Sloshing for Oscillating Chamber

Sloshing is important to generate the large-amplitude, cilia motion when the entire chamber is oscillated (case c). To illustrate this, sloshing was experimentally suppressed by using a glass slide to cover the chamber (which is filled with DI water) and thereby constraining the sloshing of the water surface. The response of the same set of cilia, with and without the glass-slide cover, i.e., without and with sloshing, is shown in Figure 3.5. Note that the amplitude of cilia motion is substantially reduced when sloshing is suppressed as opposed to the case when the water surface is free to slosh. When sloshing is suppressed, the sloshing gain K_{sl} in the transfer function G_y (see Eqs. 3.31, 3.34) becomes close to zero.

Cilia Motion without Sloshing Even without sloshing, vibrational resonance could lead to large-amplitude, cilia motion when the entire chamber is oscillated

(case c). However, such large amplitudes should not be expected, as discussed below. Note that the dynamics of the cilia motion without sloshing ($G_{sl} = 0$ in Eq. 3.34) reduces to the term G_1 in the transfer function in Eq. (3.34). The numerator of this term G_1 contains the difference between the density of the liquid ρ_f and the density of the cilium ρ_b, which implies that the transfer function gain tends to zero when the two densities become close. In the current experimental system the two densities are close — the density of the water is $\rho_f = 1000\text{kg/m}^3$ and the density of the PDMS cilium is $\rho_b = 950\text{kg/m}^3$. Therefore, the amplification of the cilia motion due to cilia resonance without sloshing, represented by the term G_1, is small. This implies that the cilia and the fluid tend to move together with the chamber when the chamber is oscillated without sloshing. Thus, large cilia motion is not achieved without sloshing, and therefore, sloshing plays an important role in achieving large cilia motion as illustrated by the experimental results in Figure 3.5.

Effect of Liquid Height on Cilia Dynamics

The sloshing dynamics, modeled by a linear second order system in Eq. (3.31), depends nonlinearly on the geometric properties of the chamber such as its diameter and the liquid height. For example, the variation of the frequency response when the liquid height is varied for the same set of cilia is shown in Figure 3.6. As the liquid height increases, the distance of the cilia (which is at a fixed height from the base of the chamber) from the free surface of the sloshing water also increases. The sloshing parameters corresponding to each height experiment are obtained by minimizing the least-square of the error between the model's predicted frequency response and the mean experimental frequency response in Figure 3.6, where the cilia-related terms (G_1, G_2) in the dynamics G_y (Eq. 3.34) were kept the same as the mean values for case (b) given in Eq. (3.41). The resulting sloshing parameters are given in Table 3.3.

The variation in the sloshing response with different liquid heights in the chamber,

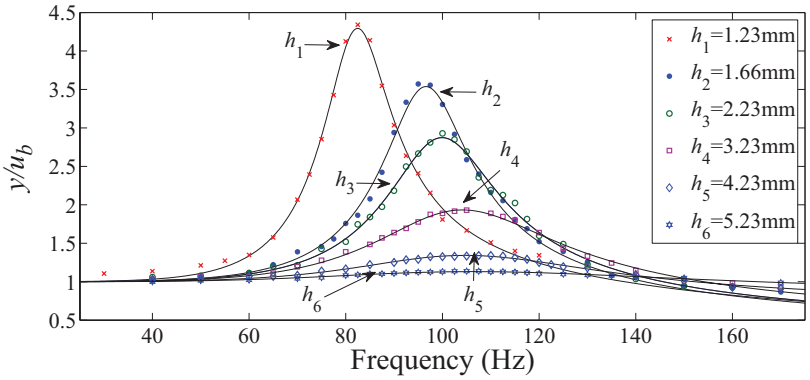

Figure 3.6: Frequency responses for cilia in an oscillating chamber when the height of water is varied. Each data point (dot) represents the average value for the three cilia used in each experiment. The same cilia are used in all these experiments. The frequency responses of the fitted models are given by solid lines.

Water Level h (mm)	ω_{sl} (Hz)	ζ_{sl}	K_{sl}
$h_1 = 1.23$	82.26	0.085	0.631
$h_2 = 1.66$	96.63	0.095	0.489
$h_3 = 2.23$	100.11	0.119	0.448
$h_4 = 3.23$	104.67	0.198	0.376
$h_5 = 4.23$	106.41	0.287	0.209
$h_6 = 5.23$	107.23	0.471	0.136

Table 3.3: Variation of sloshing parameters with water height in the chamber.

which also increases the distance of the cilia from the free surface, is expected. In particular, the liquid near the free surface has a larger sloshing amplitude compared to the liquid farther below the free surface [52]. Therefore, the sloshing gain K_{sl} is expected to decrease with an increase in the liquid height above the cilia. Moreover, the reduction in the sloshing natural-frequency ω_{sl} in Table 3.3 with liquid height is also expected in standard sloshing models, which predict that the sloshing natural-

frequency, for cylindrical containers, is proportional to the square root of a hyperbolic tangent function of the depth of water [52]. Although standard sloshing models are developed for relatively larger containers [52], the sloshing in the chamber has a similar functional dependence on the liquid height in the range of the operating conditions. In particular, the natural frequency variation with height, in Table 3.3 and shown in Figure 3.7, has the form

$$\omega_{sl}^2 = \frac{A}{(2\pi)^2}\left[\tanh\left(B\frac{h}{R}\right)\right] \tag{3.42}$$

where h is the water level, R is the radius of the chamber, ω_{sl} is the sloshing natural frequency in Hz, and with the least-squares fit to reduce the error between the model and the experimental values resulting in parameters

$$A = 454460, \quad B = 0.9.$$

The resulting prediction of the variation in the sloshing natural-frequency in Eq. (3.42) is shown in Figure 3.7, which indicates that the frequency-variation with liquid-height meets the expected hyperbolic tangent relation. It is noted that such models can be used to predict the sloshing frequencies for other water levels in the chamber, e.g., to optimize the interaction between the cilia dynamics (G_2 term in Eq. 3.34) and the sloshing dynamics (G_{sl} term in Eq. 3.34) for maximizing the cilia response.

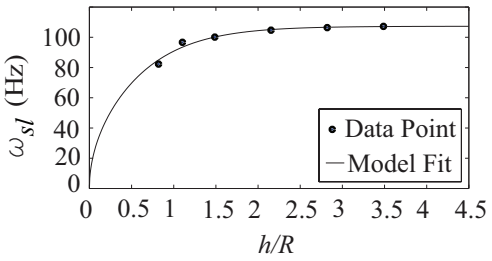

Figure 3.7: Variation of the sloshing natural-frequency ω_{sl} with the ratio of the water height h to the chamber radius R. The dots represent the experimental data and the solid line represents the prediction by the fitted model in Eq. (3.42) .

3.4.3 Fluid-Structure Interaction

The interaction between the liquid dynamics (sloshing) and the structural dynamics (cilia vibrations) predicted by the model is experimentally investigated in this subsection.

Fluid-Structure Interaction in the Model

For a given sloshing dynamics $(K_{sl}, \zeta_{sl}, \omega_{sl})$, the cilia motion will be excited the most when the cilia resonance $\omega_{r,b}$ in water gets close to the sloshing natural frequency ω_{sl}. This is because the increase in the cilia motion y compared to the chamber oscillation u_b depends on the product $G_{sl}G_2$ (in Eq. 3.34) — especially since the term G_1 is small when the liquid density ρ_f is close to the cilia density ρ_b as discussed before. The product $G_{sl}G_2$ becomes large when each term becomes large. More precisely, the cilia-motion amplitude will be maximized when the resonance frequency of the structural-vibration term G_2 is the same as the resonance frequency of the sloshing term G_{sl} and the cilia motion will be maximized if both these resonance frequencies (of structural-vibrations G_2 and sloshing G_{sl}) are the same. Thus, the interaction of the sloshing dynamics (G_{sl} term) with the structural-vibration dynamics (G_2 term) is important in determining the cilia motion.

Interaction of Sloshing and Added-Mass Effects The added-mass effect plays a key role in the interaction between structural-vibrational resonance and sloshing resonance by lowering the vibrational-resonance frequency. For example, without the added mass effect, the resonance frequency would be at 334.13Hz (see Table 3.1). The ensuing excitation of structural vibrations by sloshing with such a high vibrational-resonance frequency (without the added mass effect) would not be as much as the case when the vibrational-resonance frequency of the cilia is lowered by the added-mass effect. This re-emphasizes the importance of considering both effects, added-mass and sloshing, to capture the response of the cilia.

Experimental Results for Varying Cilia Length

For a given sloshing response, increased cilia motion should be expected when the natural frequency of the cilia in water ω_n gets closer to the natural frequency ω_{sl} of the sloshing dynamics — note that the resonance frequencies are close to the natural frequencies due to small damping. To illustrate this, the frequency responses of cilia with different lengths (i.e., different vibrational response G_2 and natural frequencies) are excited with the same sloshing dynamics G_{sl}, i.e., a fixed natural frequency for sloshing. One expects the motion to be largest for cilia whose resonance frequency of structural vibration is closest to the resonance frequency of sloshing.

Procedure and Results Cilia were cut with a sharp blade, and the lengths were measured using images acquired with the microscope where the length of the uncut cilia is known a-priori. The frequency responses of the different-length cilia were measured when the cilia were oscillated in a stationary chamber (case b) and when the chamber was oscillated (case c). The same cilia were used in both the experiments. The experimental frequency responses for each case (shown in Figures 3.8,3.9) were fitted using least-squares error minimization as discussed before (for cases b and c) and the resulting model parameters are shown in Tables 3.4, 3.5.

Discussion of Length Effect As anticipated, when the chamber is oscillated, the sloshing tends to excite the cilia substantially more if the sloshing resonance is close to the cilia resonance. For example, the 800μm cilium has the largest amplitude (seen in Figure 3.9 as well as Table 3.5) because its vibrational-resonance frequency in water $\omega_{r,w} = 108.40$Hz (see Table 3.4) is closest to the sloshing resonance-frequency that is, in turn, close to the sloshing natural-frequency ω_{sl} that lies between 95Hz and 98Hz (see Table 3.5). Note that even with different lengths, the maximum (input-to-output) amplifications of the different-length cilia are about the same when the cilia are oscillated in the fixed chamber — see Figure 3.8 and Table 3.4 — the short-

est 425μm cilium has a maximum amplification A_{max} of 1.75 which is close to the maximum amplification of 1.85 for the longest 800μm cilium in Table 3.4.

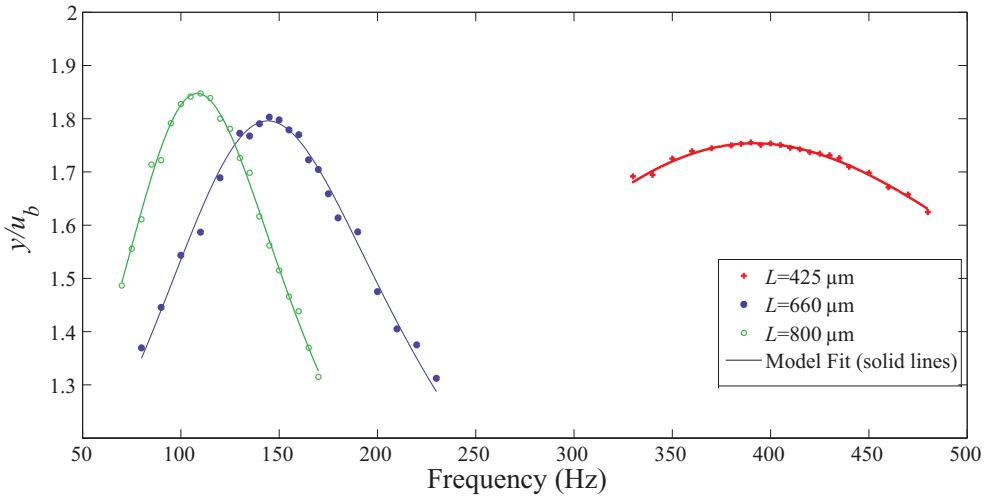

Figure 3.8: Stationary chamber (case b): frequency responses for different-length cilia. Experimental values are represented by dots. Responses of models with parameters fitted by least-squares error minimization is presented with solid lines.

In contrast, the amplification ratios are substantially lower for the two, shorter cilia than the longest cilium in the sloshing case — the shortest 425μm cilium has a maximum amplification of 1.83 which is much smaller than the maximum amplification of 3.58 for the longest 800μm cilium in Table 3.5.

Predictive Capabilities of the Model The model can predict the variation in the dynamics with the change in length, e.g., for the cut cilia. To illustrate, the parameters found for the intact (not cut) 800μm cilium were used to predict the response of cut cilia in the oscillating chamber. In particular, the natural frequencies of the shorter cilia (in a stationary chamber) were predicted as

$$\begin{aligned} \omega_{n,w,660} &= \omega_{n,w,800} * (800/660)^2 = 169.46\text{Hz} \\ \omega_{n,w,425} &= \omega_{n,w,800} * (800/425)^2 = 408.68\text{Hz} \end{aligned} \tag{3.43}$$

since the natural frequency of a vibrating cantilever is inversely proportional to the square of the length, where the lengths of the cilia are added as subscripts for clarity. The damping ratios (ζ_1, ζ_2) do not change significantly with length (as seen in Table 3.4 as well as in previous work [1]); therefore, the damping ratios for the cut cilia were chosen to be the same as the damping ratios for the uncut 800μm cilium, i.e., $\zeta_1 = 0.435$ and $\zeta_2 = 0.446$ from Table 3.4. The sloshing parameters in the predicted models for the cut cilia were kept the same as those for the uncut 800μm cilium, i.e., $K_{sl} = 0.482$, $\zeta_{sl} = 0.094$, $\omega_{sl} = 97.07$ from Table 3.5.

The predicted frequency response is close to the frequency response of the fitted models and the experimental data of the frequency response as shown in Figure 3.9. The maximum errors E_{fit}, E_{pred} in the frequency response between the fitted and predicted models, provided in Table 3.5, are defined as

$$E_{fit} = \max_{\omega_k} \left| \frac{A_{fit}(\omega_k) - A_{exp}(\omega_k)}{A_{exp}(\omega_k)} \right| \times 100, \quad E_{pred} = \max_{\omega_k} \left| \frac{A_{pred}(\omega_k) - A_{exp}(\omega_k)}{A_{exp}(\omega_k)} \right| \times 100 \tag{3.44}$$

where A_{exp}, A_{fit}, and A_{pred} represent the amplification factors of the frequency responses (at each frequency ω_k where the experimental data is available) from the experiments, fitted models, and predicted models, respectively. Note that the maximum error E_{pred} with the predicted model (e.g., 9.12 for the 660μm cilium) is similar to the maximum error E_{fit} of the fitted model, e.g., 6.46 for the 800μm cilium that is used to predict the model of the cut cilia. Hence, the model can be used to evaluate the effect of changing cilia length. For example, with a given chamber geometry (i.e., given sloshing dynamics), the model could be used to optimize the cilia length for maximizing the cilia motion.

The validity of using the above models for predicting the effect of parameter variations such as cilia stiffness and fluid viscosity has not been investigated in this work. For example, previous work [52] (pages 166-167) has shown that the main sloshing frequency tends to be relatively insensitive to large changes in fluid viscosity.

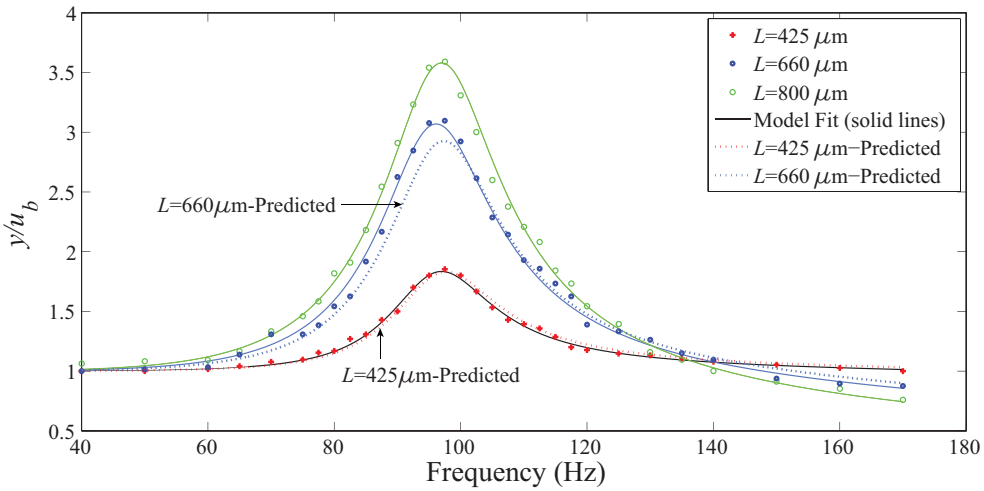

Figure 3.9: Oscillating chamber (case c): frequency responses for different-length cilia. Experimental values are represented by dots. Response of models with parameters fitted by least-squares error minimization is presented with solid lines. Dashed lines represent responses of predicted models.

L (μm)	ζ_1	ζ_2	$\omega_{n,w}$ (Hz)	$\omega_{r,w}$ (Hz)	A_{max}
425	0.458	0.472	420.42	391.68	1.75
660	0.443	0.459	154.21	144.28	1.80
800	0.435	0.446	115.34	108.40	1.85

Table 3.4: Stationary chamber: parameters and maximum amplification A_{max} of fitted models for different-length cilia corresponding to Figure 3.8.

Nevertheless, such studies were for relatively large-sized chambers. Additional work is needed to validate the currently proposed models for such parameter variations.

L (μm)	ζ_{sl}	ω_{sl} (Hz)	K_{sl}	A_{max}	E_{fit}	E_{pred}
425	0.093	96.47	0.478	1.83	3.70	5.36
660	0.095	95.98	0.492	3.07	4.82	9.12
800	0.094	97.07	0.482	3.58	6.46	N/A

Table 3.5: Oscillating chamber: parameters and maximum amplification A_{max}, of fitted models for different-length cilia corresponding to Figure 3.9 along with maximum error (Eq. 3.44) in fitted and predicted models.

3.4.4 Mixing with and without Cilia

The mixing results of ink and water in an oscillating chamber with-and-without cilia (but with liquid sloshing in each case) are comparatively evaluated to show that the use of cilia leads to faster mixing.

Procedure for Mixing Experiments

The procedure of the mixing experiment with cilia is described below. The procedure for the mixing experiments without cilia (i.e., vibration only) is the same as the case with cilia except that cilia are not present in the chamber. For mixing experiments with cilia, three cilia are arranged in the mixing chamber as shown in Figure 3.10. The cilia mixing device is attached to the piezoactuator as shown in Figure 3.1(a). The cilia mixer system is positioned above an inverted microscope. After positioning the cilia mixer, de-ionized (DI) water (11μL) is added to the chamber using a pipette. Collapsed cilia, if any, are straightened by using tweezers. Next, 0.25μL of black ink (Drawing ink A, Pelikan, Hannover, Germany that is diluted 80 times with DI water) is released gently using a pipette at the center of the chamber under the water surface. The initial image of the ink drop (at time $t = 0$s) is shown in Figure 3.11. A thin PDMS sheet is placed above the chamber to enclose the mixing chamber to

avoid evaporation of the solution during the mixing experiments. The PDMS cover does not suppress sloshing of the free surface because the solution volume together with the cilia-support structure creates a maximum water height of 1.66mm, which does not reach the top of the chamber. Additionally, a support for the cover is added (as in Figure 3.10) to prevent the cover from sagging and touching the water surface. Subsequently, the piezoactuator is used to oscillate the chamber perpendicular to the length of the cilia with an amplitude of 10μm as in Figure 3.3(c). The oscillation frequency is chosen as the maximum-amplitude resonance frequency with the cilia that was measured for each run before the ink was introduced — this oscillation frequency is kept the same for both cases, with and without cilia, for that particular run.

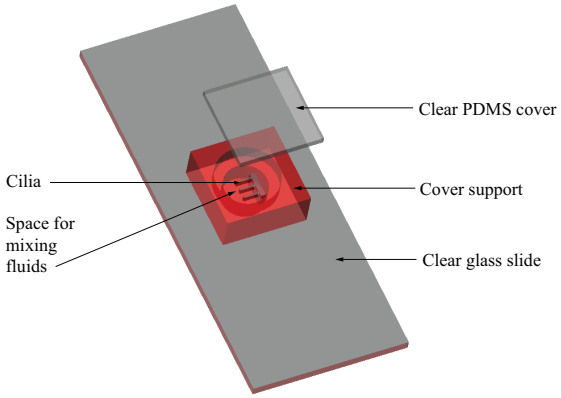

Figure 3.10: Schematic setup of cilia device shown in Figure 3.1(a) for mixing experiments in a 3mm diameter chamber.

Each mixing experiment (with and without cilia) was repeated seven times. For each mixing experiment, the initial image is captured after the addition of ink and after the thin PDMS sheet is used to cover the chamber but just before the start of the chamber oscillations with the piezoactuator. Preliminary experiments were performed to choose a sufficiently large time for the mixing experiments such that the mixing index (described in the section below) reaches a steady state value. Based on these

preliminary studies, the time t_N for the final image was chosen as 50s for the case with cilia and 600s for the case without cilia. (Additionally, the images were inspected to visually verify that they do not change change significantly when the last images were collected.) The time for the mixing index to reach and stay within 90% of its final value is used to quantify and comparatively evaluate the mixing performance with and without cilia. A CCD camera, attached to the microscope (see Figure 3.1(a)), is used to video-record the mixing process for evaluation and samples of the acquired images are shown in Figure 3.11.

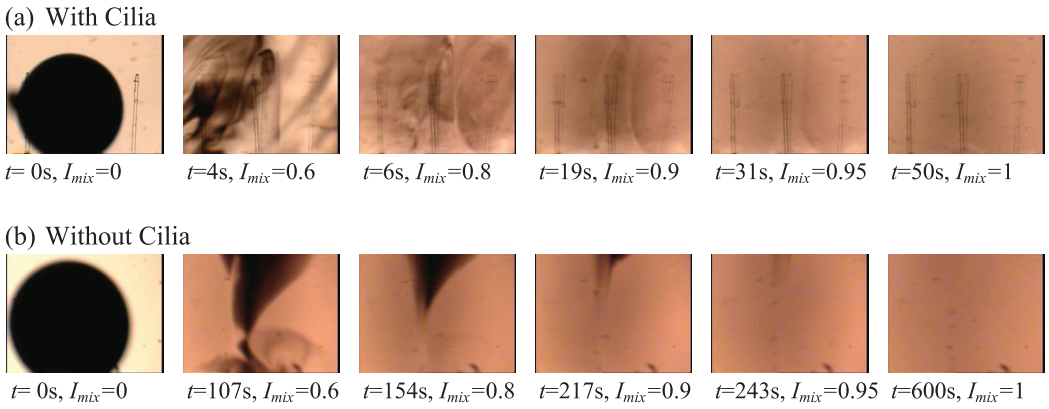

Figure 3.11: Sample images of the mixing process at different time instants t and corresponding mixing indices, I_{mix} as in Eq 3.45 : (a) with cilia, run 1 in Table 3.6 ; and (b) without cilia, run 1 in Table 3.6.

Quantifying Mixing

The mixing was quantified by comparing images from the video recording of the mixing process using a mixing index I_{mix} developed in [60], which is a discrete version of the continuous time mixing index defined in [78]. The mixing index, which is a measure of relative mixing is initially 0 and approaches 1 when the fluids become fully

mixed, is given by

$$I_{mix}(t_k) = \frac{1}{I_{ss}} \left[1 - \frac{\sum_{p=1}^{P} |C_p(t_k) - C_p(t_N)|}{\sum_{p=1}^{P} |C_p(t_0) - C_p(t_N)|} \right] \tag{3.45}$$

where $[t_k]_{k=1}^{N}$ represents the different time instants when the images are evaluated, N is the total number of images, P is the number of pixels in each of the images, $C_p(t_k)$ is the color of pth pixel at time instant t_k and the normalization factor I_{ss} is given by

$$I_{ss} \;=\; \left| 1 - \frac{\sum_{p=1}^{P} |C_p(t_{N-1}) - C_p(t_N)|}{\sum_{p=1}^{P} |C_p(t_0) - C_p(t_N)|} \right|. \tag{3.46}$$

Each image used in this analysis is composed of an array of 352 pixels by 240 pixels, and the color of each pixel C is a vector of three values

$$C \;=\; [R \;\; G \;\; B]$$

that represents red, green, and blue (RGB) color with values between 0 and 255. Given any two pixel colors C_i and C_j, the difference between them (used in Eqs. 3.45, 3.46) is defined as

$$|C_i - C_j| \;=\; |R_i - R_j| + |G_i - G_j| + |B_i - B_j|.$$

As the mixing progresses and reaches a steady state (i.e., as t_k approaches t_N), the difference between the color of the corresponding pixels in the images becomes small, which tends to increase the values of I_{mix} from an initial value of zero towards one. The normalization factor I_{ss} in Eq. (3.46) uses the last two images to make the mixing index close to one when the mixing process reaches steady state and the images become similar. This is necessary because noise in the image (partly due to the oscillation) prevents the final value from reaching one without the normalization, i.e., when $I_{ss} = 1$ in Eq. (3.45).

Mixing Results and Discussions

The mixing time is substantially reduced with cilia when compared to the case without cilia even though liquid sloshing occurs in both cases. The reduction in mixing time

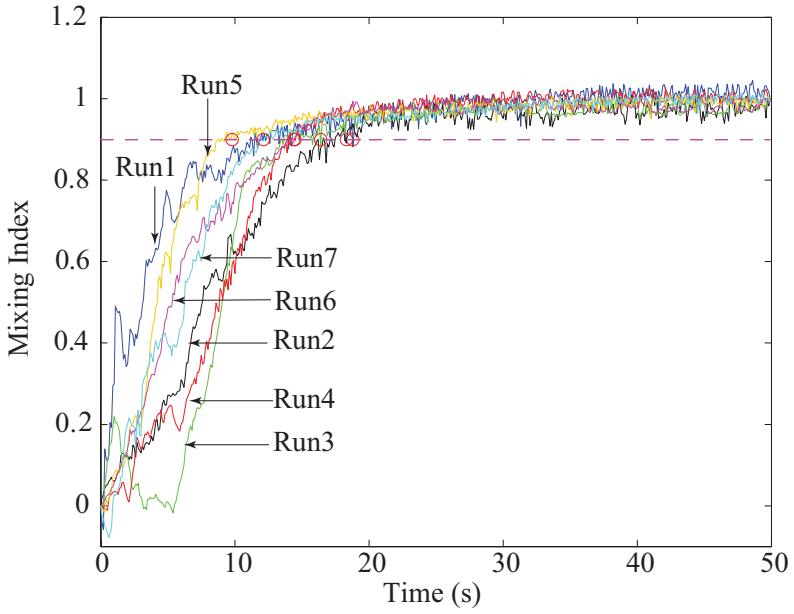

Figure 3.12: Time profiles of the mixing index I_{mix} in Eq. (3.45) for seven experimental runs with cilia. The 90% mixing time is indicated with circles.

is visually observable in the images (with and without cilia) shown in Figure 3.11. For example, to reach the 90% mixing time (corresponding to the images on the 4th column), the mixing takes 19s with the cilia whereas it takes 217s for the case without the cilia. To quantify the mixing rate, the variation of the mixing index for the seven experimental runs (with and without cilia) are shown in Figures 3.12, 3.13 and the 90% mixing times for the different experiments are presented in Table 3.6.

It is noted that the average mixing time of 14.9s with cilia is about 12 times lower than the average mixing time of 176.4s without cilia. Therefore, the use of cilia can substantially decrease the mixing time, by more than an order of magnitude, when compared to the case without cilia. The mixing performance could be improved further with the use of more general inputs (chamber oscillations); the current model (with its relatively-low-order dynamics) is well suited for controller development in

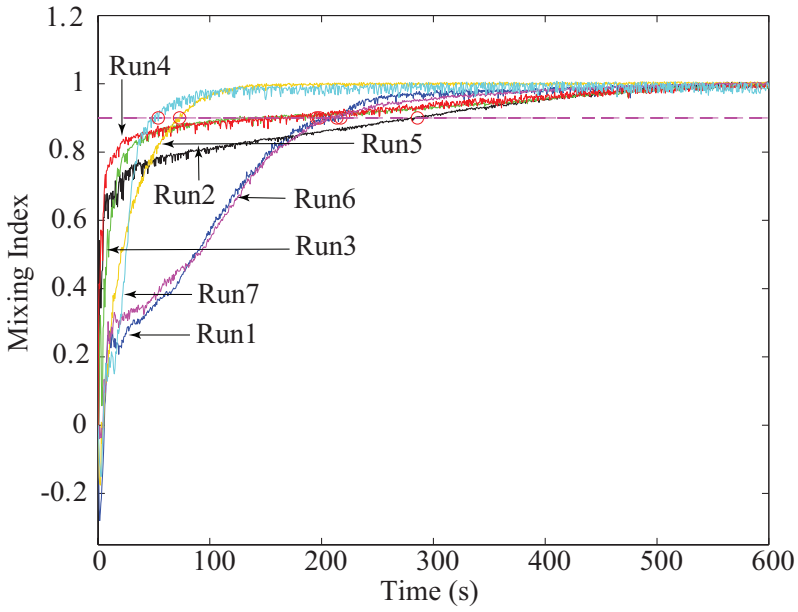

Figure 3.13: Time profiles of the mixing index I_{mix} in Eq. (3.45) for seven experimental runs without cilia. The 90% mixing time is indicated with circles.

such future studies.

Potential Use of Model in Mixing Optimization The current work shows that large cilia motion can be used to reduce the time needed for mixing. The experiments used sinusoidal excitation of the chamber; however, it is possible that a more general input (oscillation of chamber) can lead to even faster mixing. The low order of the current model makes it well suited to design such optimal control for the mixing process. Moreover, by providing insight into effects, such as the interaction between added mass and sloshing in determining cilia motion amplitudes, the model can be used to provide guidelines for optimizing the cilia design, such as the choice of the cilia length for a given chamber geometry. An advantage of the current model is the low order of the dynamics, which does not pose substantial computational burden in optimization studies and controller development. Further work is needed to evaluate

Run Number	Oscillation Frequency (Hz)	Mixing Time with Cilia (s)	Mixing Time without Cilia (s)
1	95	18.8	217
2	97	18.3	285.5
3	96	16.4	193.5
4	96	14.5	198
5	98	9.8	73
6	95	14.4	213.5
7	98	12.1	54
Mean	96.43	14.9	176.4
σ	1.27	3.248	83.02

Table 3.6: Mixing time(s) quantified by the time for the mixing index I_{mix} in Eq. (3.45) to reach and stay within 90% of its final value, with and without cilia.

these models for such control and design approaches to optimize cilia-based devices.

3.5 Conclusions

This chapter modeled the dynamics of cilia-based devices for mixing and manipulating liquids in microfluidic applications. The models showed that, both, sloshing and added-mass effects play substantial roles in generating large-amplitude cilia motion in liquid. Additionally, experimental results, with and without cilia, were comparatively evaluated to show more than an order-of-magnitude reduction in the mixing time with the use of cilia.

Chapter 4

ITERATIVE CONTROL OF PIEZOACTUATOR FOR EVALUATING BIOMIMETIC, CILIA-BASED MICROMIXING

4.1 Overview

This work evaluates the use of different excitation waveforms to improve biomimetic-cilia-based mixing in microfluidic applications. A challenge in such studies is that, at high frequencies, vibrations in the piezoactuator can distort the achieved excitation waveform. An iterative approach is used in this work to account for the vibrational dynamics and avoid unwanted vibrations in the achieved excitation waveforms, and thereby enable the evaluation of different excitation waveforms on mixing. The main contribution of this work is to use these controlled, excitation waveforms for showing that (i) mixing time is substantially reduced (by more than an order of magnitude) with the use of cilia when compared to the case without cilia and (ii) mixing time with cilia can be further reduced (by more than half) by using an asymmetric excitation waveform when compared to symmetric (sinusoidal) excitation.

Based on biological cilia systems, e.g., [40–43], biomimetic, cilia-type, compliant actuators have been proposed for mixing and manipulation in liquid environments, e.g., see [15, 32, 46–50]. Recent works have shown that mechanical (sinusoidal) excitation of the cilia by using a piezoactuator to oscillate the cilia-chamber can improve mixing in microfludic devices [2, 60]. The current work aims to evaluate potential improvements in cilia-based mixing with different excitation waveforms of the cilia-chamber. A challenge in such evaluation studies is that, at high frequencies, vibrations in the piezoactuator can distort the achieved motion (excitation waveform) of

the cilia-chamber, and thereby, limit the ability to evaluate the effect of a desired excitation waveform on mixing. An iterative feedforward approach [61] is used in this work to account for the vibrational dynamics of the piezoactuator, and reduce unwanted vibrations in the achieved excitation waveforms. The main contribution of this work is to use these controlled, excitation waveforms for showing that: (i) the average (90%) mixing time is substantially reduced with the use of cilia when compared to the case without cilia by 13 times from 175s to 13.56s (with sinusoidal excitation) and (ii) the average (90%) mixing time with cilia can be further reduced (about 2.6 times from 13.56s to 5.17s) by using an asymmetric excitation waveform when compared to symmetric (sinusoidal) excitation. Thus, the chapter shows that the choice of the excitation waveform can improve mixing performance with cilia, which suggests the need for further efforts in excitation-waveform optimization.

In general, micromixing can be improved by generating complex flows in the fluid to overcome the mixing-rate limits of laminar flows that are typical at the microscale. For example, passive techniques such as grooves can be used to generate chaotic folding (and refolding) of the liquid as it flows past the grooves to improve mixing, e.g., in [12]. Such flow-type mixing can be used when a sufficiently-large amount of sample is available to achieve the flow through the grooved channel. In contrast, if the amount of sample is limited, then batch-type mixing needs to be achieved in small chambers containing the sample. Batch mixing can be enhanced using a variety of actuation techniques such as high-frequency ultrasound excitation [13, 57, 62] and time-varying external magnetic fields [15, 21, 58, 59]. In the current work, cilia are excited by relatively-low-frequency oscillations of the chamber containing the sample when compared to higher-frequency ultrasound excitation. It is noted that the low-frequency excitation used in this chapter is advantageous for mixing samples that are susceptible to damage from high-frequency excitation [63–65]. Similarly, sample damage is a concern with the use of rapidly varying external magnetic fields, which

is also avoided with the present approach. The current chapter shows that batch mixing can be substantially improved by using low-frequency excitation with soft cilia — this use of low-frequency excitation with soft actuators has the potential to reduce the damage of fragile samples during micromixing.

4.2 Problem Formulation

4.2.1 System Description

The displacement transverse to the length (x) of a cilium was excited by using a piezoactuator (Burleigh PZS200) as shown in Figure 4.1a,b. The soft cilia were fabricated from polydimethylsiloxane (PDMS) using a silicon mold; detailed information on cilia fabrication and material properties can be found in [32]. The dimensions of the silicon mold used to fabricate the cilia were length ($L = 800\mu m$), height ($H = 45\mu m$), and width ($W = 10\mu m$) as in Figure 4.1c. The cilia and the fluid motion (Figure 4.1d) in the chamber were observed and evaluated using videos obtained with an optical microscope and an attached, digital, color CCD camera, as well as, still images (Pinnacle Studio Version 12). An example image of the resulting cilia vibration (due to the chamber oscillation) is shown in Figure 4.1e.

4.2.2 The Positioning Problem

An oscillatory excitation u_c of the cilia-chamber is achieved by using a piezo-based positioning system (referred to as the piezoactuator in the following) as shown in Figure 4.1. The motion of the base of each cilium is also u_c since the cilium base is attached to the chamber through a relatively-stiff PDMS structure. To evaluate the mixing achieved with different types of excitation waveforms (i.e., time profile of u_c), the piezoactuator needs to position the chamber precisely along the desired waveform u_c. At high oscillation frequencies, vibrations in the piezoactuator positioning system can lead to distortions in the achieved position trajectory (excitation waveform),

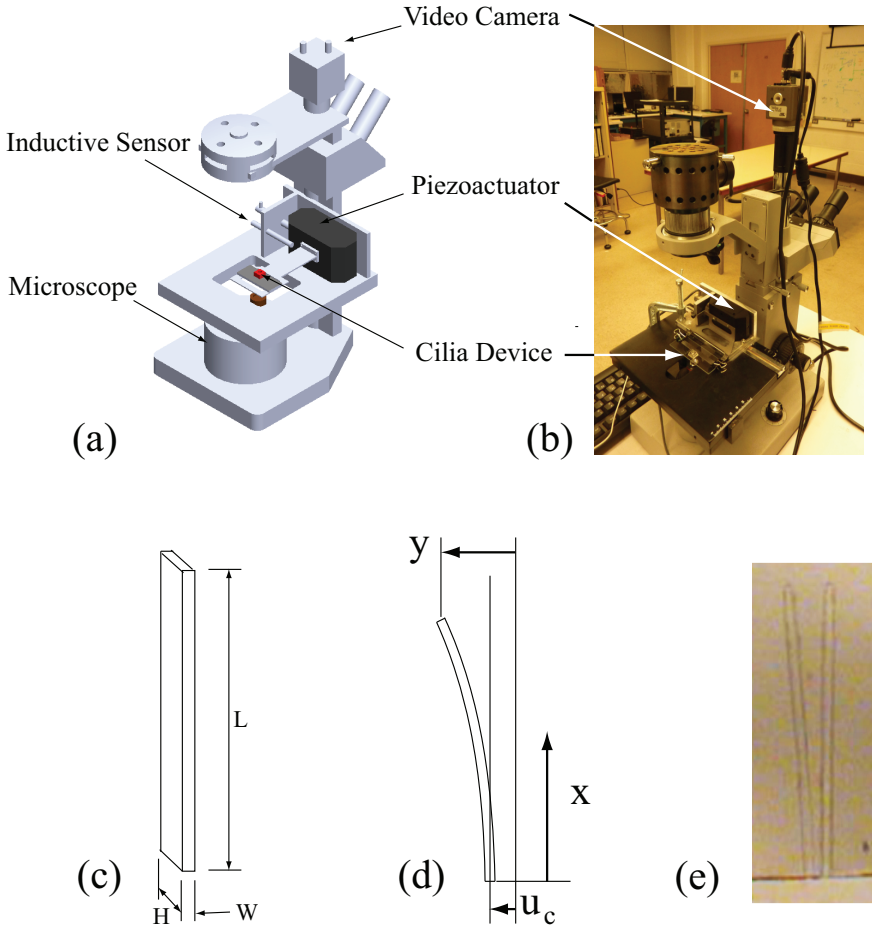

Figure 4.1: Schematics of experiment for evaluating micromixing with cilia. Experimental setup: (a) schematic; and (b) photo. (c) Nominal cilium dimensions are length $L = 800\mu m$, width $W = 10\mu m$, and height $H = 45\mu m$. (d) Base motion $u_c(t)$ at $x = 0$ and tip motion $y(t)$ at the free end $x = L$ of a cilium. (e) Photo of a cilium in water excited by piezoactuator.

which make it challenging to evaluate specific excitation waveforms. The control goal is to correct for such vibration-caused distortions.

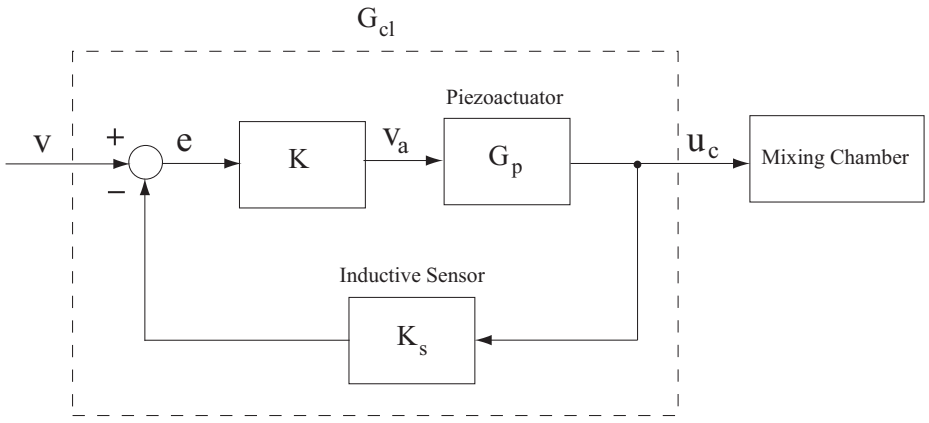

Figure 4.2: Block diagram of the positioning system. The piezoactuator is represented by G_p, the achieved chamber motion u_c is measured with an inductive sensor with gain $K_s = 0.2$ (V/μm), and G_{cl} represents the closed-loop system.

4.3 Iterative Control of Piezoactuator

The model of the piezoactuator system, the design of the excitation frequency and waveforms, and iterative control to achieve the desired excitation waveform are discussed in this section.

4.3.1 Piezoactuator Model

A schematic of the positioning system is shown in Figure 4.2, where G_p represents the piezoactuator, the achieved chamber motion u_c is measured with an inductive sensor with gain $K_s = 0.2$ (V/μm), and G_{cl} represents the closed-loop system. The model of the closed-loop positioning system (G_{cl}) is obtained experimentally. Example experimental frequency responses of the closed loop system, obtained by using a dynamic signal analyzer (SRS Model SR785), are shown in Figure 4.3 for two cases: small amplitude; and large amplitude. For the small amplitude case, the input voltage V to the closed loop system was kept fixed at amplitude (0.1V) over different frequencies, which corresponds to a chamber-motion amplitude of 0.6μm (at low frequencies). For

the large amplitude case, the displacement amplitude was fixed at a relatively-larger value of 5μm over different frequencies by varying the amplitude of the input voltage V. The substantial difference in the experimental frequency responses (in Figure 4.3) can be attributed to the significant hysteresis present in the system illustrated in Figure 4.4. This variation in the frequency response implies that linear models used to find feedforward inputs can have substantial error, which needs to be corrected.

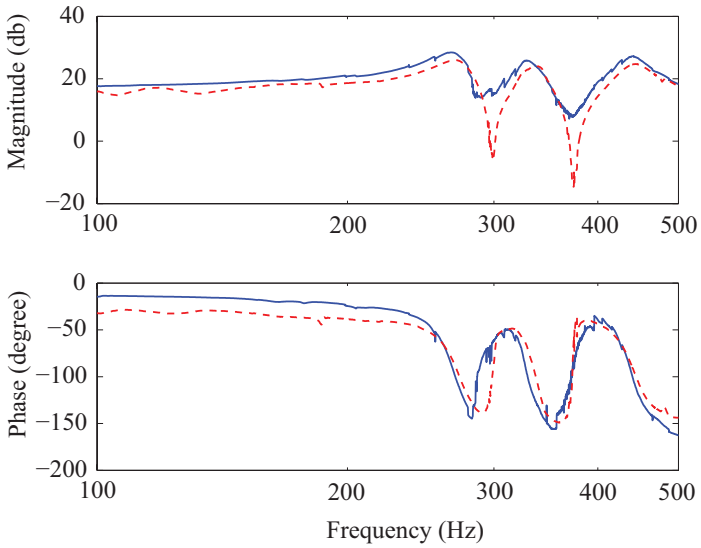

Figure 4.3: Experimental frequency responses of the closed-loop system, G_{cl} in Figure 4.2 for two cases: small amplitude (dashed line); and large amplitude (solid line).

4.3.2 Choice of Control Method: Iterative Feedforward

Given a desired, excitation waveform $u_{c,d}$, the current chapter uses an iterative feedforward method to find the input V to achieve precision tracking of the desired waveform. It is noted that previous works have shown that iterative feedforward approaches can yield the highest tracking precision in piezoactuator systems [79, 80]. In general, this approach can be applied with any feedback controller. In this work, the feedback was chosen as a simple proportional controller — its gain $K = 5$ was chosen to be

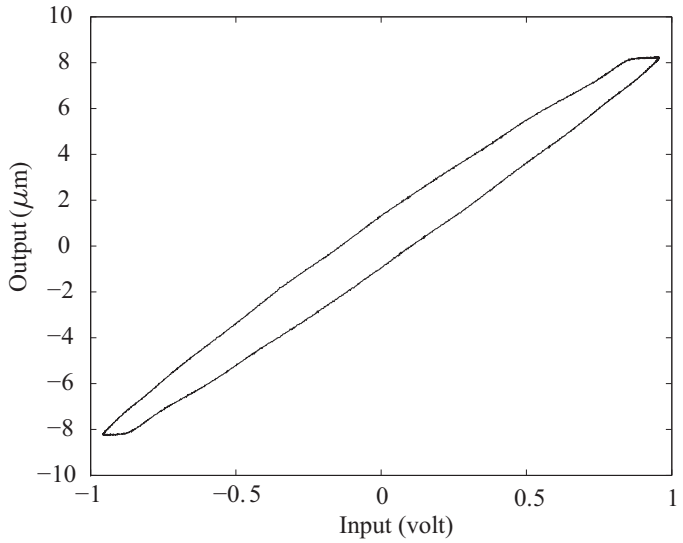

Figure 4.4: Hysteresis in the closed-loop piezoactuator system obtained by applying sinusoidal input V to the closed-loop system at 20Hz and measuring the resulting output position u_c.

as large as possible while maintaining sufficient gain and phase margins. However, the iterative approach used in this chapter can be used with more advanced feedback techniques as well.

4.3.3 Choice of Chamber Oscillation Frequency

The chamber oscillation frequency should be close to the cilia resonance frequency (in liquid) to achieve maximum excitation of the cilia [2]. To determine the chamber oscillation frequency (operating frequency) for mixing, the resonant frequencies of the cilia in liquid are found from the experimental frequency responses as shown in Figure 4.5 and Table 4.1. As seen from Figure 4.5, the maximum amplitude of cilia response does not change significantly, if the operating frequency is varied from the mean value of 96.43Hz by one standard deviation. In particular, with one standard deviation of the excitation frequency from the resonance, i.e., at 96.43Hz-1.27Hz and 96.43Hz+1.27Hz, the values of the response are $y/u_c = 3.50$ and $y/u_c =$

3.487 respectively, which represents no more than a 1.1% change from the maximum value of $y/u_c = 3.525$ at the resonance frequency 96.43Hz. Therefore, the associated change in the cilia response (because of potential variation in the resonance frequency from the mean value of 96.43Hz) is not expected to be substantial. Hence, in all experiments, the frequency ω_d of the periodic excitation trajectories was kept fixed at (approximately) the resonance frequency — $\omega_d = 96$Hz.

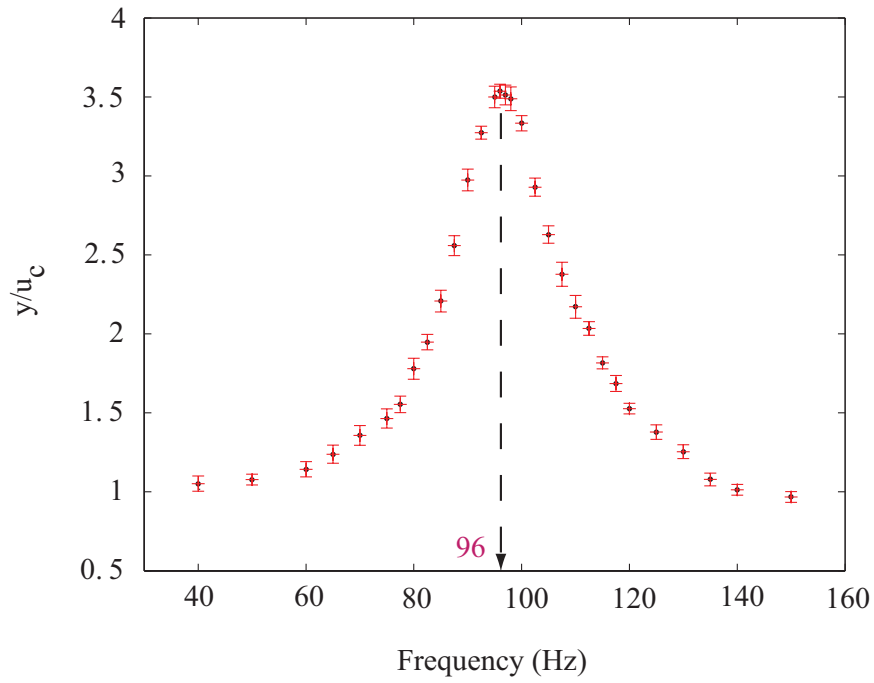

Figure 4.5: Frequency response of seven runs of cilia. Dots represent the experimental data (mean values of seven runs of cilia), and bars represent the standard deviation $\pm\sigma$. Detailed models can be found in Refs. [1, 2].

4.3.4 Desired Excitation Waveforms

Two types of excitation waveforms are considered as shown in Figure 4.6: a symmetric sinusoidal excitation (used in previous studies [2, 60]); and a preliminary asymmetric (triangular) excitation. Tracking the preliminary triangular waveform $u_{c,p}$, with sharp

Run Number	Resonant Frequency (Hz)
1	95
2	97
3	96
4	96
5	98
6	95
7	98
Mean	96.43
σ	1.27

Table 4.1: Resonant Frequencies of cilia (seven runs)

changes in velocity at the turnarounds can be challenging because the corresponding velocity profile is discontinuous and the acceleration profile will be unbounded, which can require an infinite-bandwidth, unbounded input voltage V to perfectly track the waveform. Therefore, a filtered version of the preliminary triangular waveform $u_{c,p}$ is sought as the desired asymmetric waveform $u_{c,d}$ to meet actuator bandwidth and saturation limits.

Optimal Inversion

A compromise between the goals of exactly tracking the preliminary triangular waveform $u_{c,p}$, and handling actuator bound and bandwidth limitations can be achieved using the optimal-inversion approach developed in [79]. The optimal inverse $V = V_{opt}$ is obtained by minimizing the following cost function

$$J(V) = \int_{-\infty}^{\infty} \{V^*(\omega)R(\omega)V(\omega) + E_P^*(\omega)Q(\omega)E_P(\omega)\}d\omega, \tag{4.1}$$

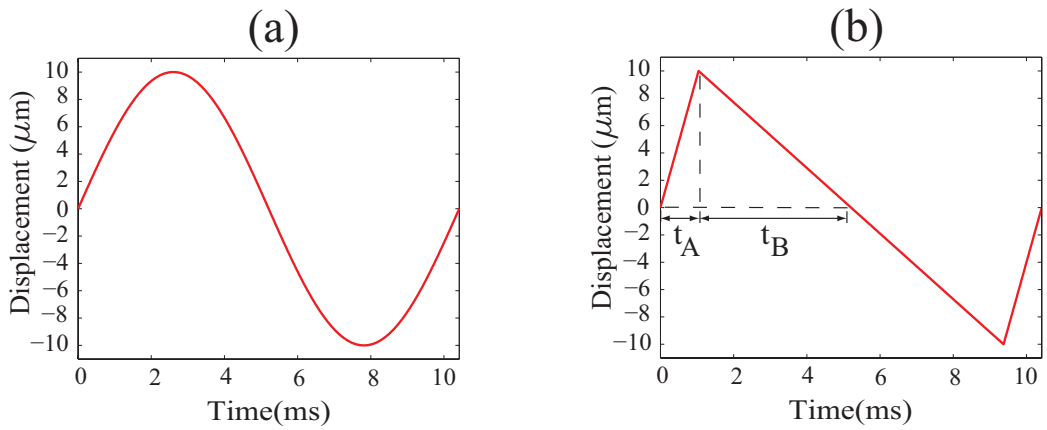

Figure 4.6: Excitation waveforms u_c for one time period: (a) desired symmetric, sinusoidal waveform $u_{c,d}$, (b) preliminary asymmetric triangular waveform $u_{c,p}$, where the ratio $\alpha = t_A/t_B = 0.25$ is a measure of the asymmetry.

where $*$ denotes the complex conjugate transpose, the input V and output u_c are related through the system dynamics G_{cl}, and

$$E_P = u_{c,p} - u_c$$

is the positioning error with respect to the given preliminary excitation waveform $u_{c,p}$.

Choosing the Weights in the Cost Function

The terms $R(\omega)$ and $Q(\omega)$ (in Eq. 4.1) can be used to account for model uncertainty and piezoactuator-bandwidth limits by appropriately choosing the input-energy weight, $R(\omega)$ and the tracking-error E_P weight, $Q(\omega)$. In particular, the weights can be chosen such that good tracking is achieved in the low-frequency range (till 100Hz for the cilia-based mixing device) and to reduce the emphasis on tracking at high frequencies where the model G_{cl} tends to become less accurate, e.g., beyond 500Hz for the current piezoactuator. This implies that the tracking-error weight Q should be larger than the input energy weight R in the low-frequency range and vice versa in the high-frequency range, as shown in Figure 4.7.

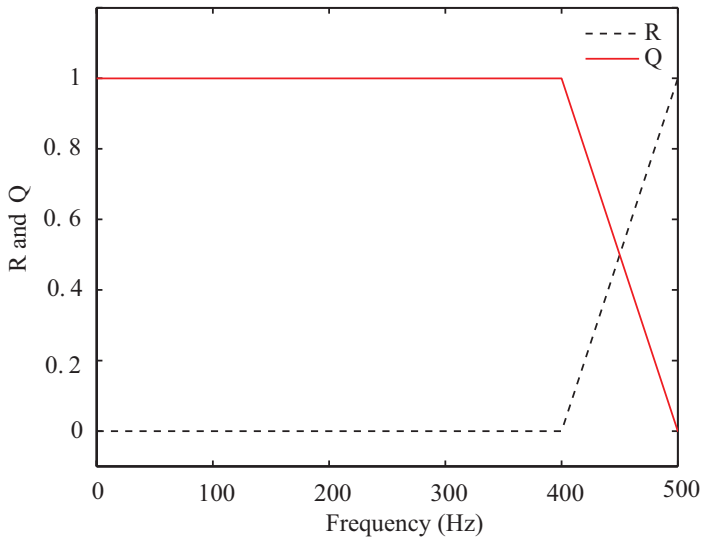

Figure 4.7: Input energy weight, $R(\omega)$ and tracking-error weight, $Q(\omega)$ used in the cost function (in Eq. 4.1) to find the optimal inverse V_{opt} and the optimally filtered bandwidth-limited asymmetric waveform $u_{c,opt}$.

Optimal Inverse Feedforward

The optimal inverse input V_{opt} minimizing the cost function (in Eq. 4.1) can be found, for the single-input-single-output (SISO) case as [79]

$$\begin{aligned} V_{opt}(\omega) &= \left[\frac{{G_{cl}}^*(\omega)Q(\omega)}{R(\omega)+{G_{cl}}^*(\omega)Q(\omega)G_{cl}(\omega)}\right] u_{c,p}(\omega) \\ &= G_{cl,opt}^{-1}(\omega)u_{c,p}(\omega) \end{aligned} \tag{4.2}$$

and the time-domain signal for the feedforward input

$$V(t) = V_{opt}(t)$$

is then obtained through an inverse Fourier transform of $V_{opt}(\omega)$.

Optimal Asymmetric Waveform

The resulting optimal output $u_{c,opt}$ is given by

$$\begin{aligned} u_{c,opt}(\omega) &= G_{cl}(\omega)V_{opt}(\omega) \\ &= \left[\frac{{G_{cl}}^*(\omega)Q(\omega)G_{cl}(\omega)}{R(\omega)+{G_{cl}}^*(\omega)Q(\omega)G_{cl}(\omega)}\right]u_{c,p}(\omega) \\ &= \left[F_{opt}(\omega)\right]u_{c,p}(\omega) \end{aligned} \tag{4.3}$$

Therefore, the optimal waveform $u_{c,opt}$ can be considered as a filtered version (passing through filter $F_{opt}(\omega)$ determined by the frequency-dependent weights $R(\omega)$ and $Q(\omega)$) of the preliminary triangular waveform $u_{c,p}$ — the original and filtered waveforms are compared in Figure 4.8. The desired asymmetric waveform $u_{c,d}$ is then chosen to be the optimally-filtered waveform, i.e., $u_{c,d} = u_{c,opt}$, and the control objective is to track this optimally-filtered, desired, asymmetric waveform. Note from Eq. (4.3), that the chosen asymmetric waveform $u_{c,d}$ has finite bandwidth since the tracking weight is zero, $Q(\omega) = 0$, for higher frequencies $\omega \geq 500$Hz.

4.3.5 Implementation: Iterative Inversion-Based Control

To account for modeling errors, the optimal inverse feedforward V_{opt} is computed (and corrected) iteratively as [3]

$$\begin{aligned} V_{opt,k}(\omega) = V_{opt,k-1}(\omega) \\ + \rho(\omega)G_{cl,opt}^{-1}(\omega)\left[u_{c,p}(\omega) - u_{c,k-1}(\omega)\right] \end{aligned} \tag{4.4}$$

for $k \geq 2$, where the initial input $V_{opt,1}(\omega)$ is

$$V_{opt,1}(\omega) = G_{cl,opt}^{-1}(\omega)\left[u_{c,p}(\omega)\right], \tag{4.5}$$

$\rho(\omega) \in \Re$ is the iteration gain, $u_{c,p}(\omega)$ is the Fourier transform of the preliminary trajectory, and $u_{c,k-1}(\omega)$ is the Fourier transform of the actual trajectory (experimentally) measured in the $(k-1)^{th}$ iteration step.

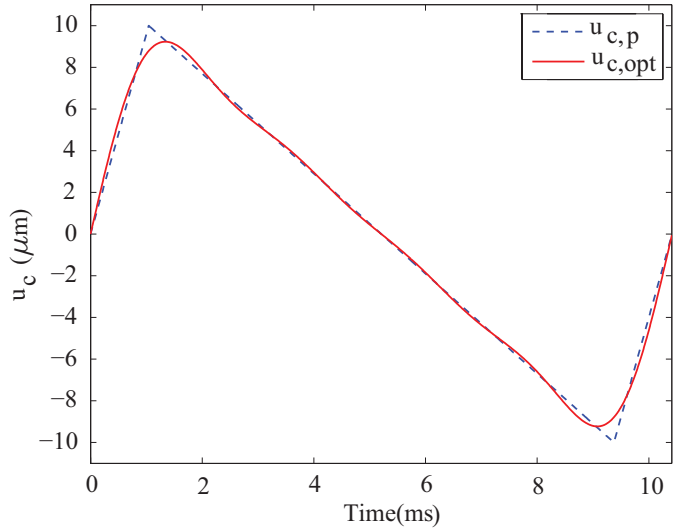

Figure 4.8: Asymmetric waveform: (dashed line) original, infinite-bandwidth, triangular waveform; and (solid line) optimally-filtered, bandwidth-limited waveform.

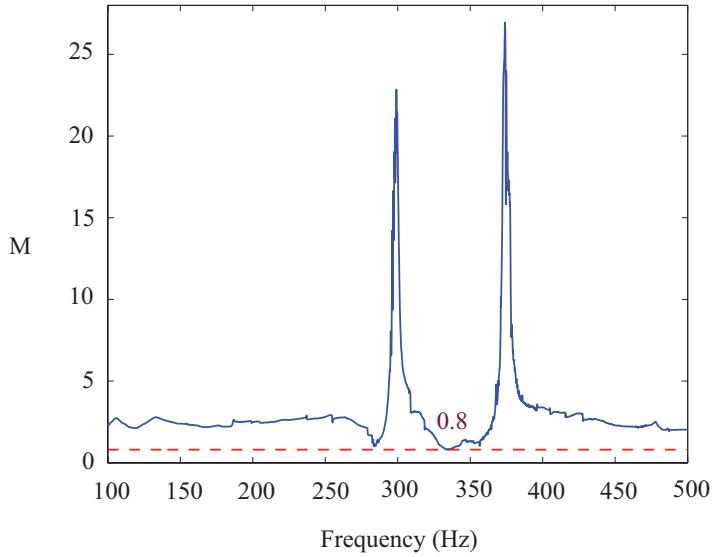

Figure 4.9: The frequency dependent bound $M(\omega)$ (solid line) on the iteration gain $\rho(\omega)$ as in [3]. The minimum value (0.8) is shown as a dashed line.

The iteration gain $\rho(\omega)$ should be chosen as large as possible to enable fast convergence; the maximum possible value can be estimated based on the anticipated modeling errors. The main criterion is to ensure that the iterative correction is in the right direction (phase criterion) — as shown in [3], the iteration gain $\rho(\omega)$ should satisfy

$$0 < \rho(\omega) < \frac{2cos(\triangle_\theta(\omega))}{\triangle_r(\omega)} = M(\omega) \tag{4.6}$$

where $\triangle_\theta(\omega)$ is the estimated phase error (difference in phase between the model and the actual system) and $\triangle_r(\omega)$ represents the estimated magnitude error (in terms of the ratio between the magnitudes of the model and the actual system) in the frequency response. These estimated errors are found using the two frequency responses (shown in Figure 4.3), and the estimated bound $M(\omega)$ on the iteration gain is shown in Figure 4.9, which has a minimum value of 0.8 in the computed frequency range. The actual bound (and the minimum) could be lower since the estimate is based on two measurements; moreover, noise can reduce the iteration gain as well as shown in [3]. Therefore, in the following, the iteration gain is chosen as a smaller value of 0.3 at all frequencies.

4.3.6 Iterative Control Results

The results of the iterations are shown in Figure 4.10 and tabulated in Table 4.2, which show that the iteration process substantially reduces the tracking error

$$E_k(t) = u_{c,opt}(t) - u_{c,k}(t). \tag{4.7}$$

In particular, the maximum tracking error

$$E_{k,max} = \max_{n\in[0,1,\ldots,N]} |E_k(t_n)|\,, \tag{4.8}$$

over all sampled time instants (t_n with $n \in [0, 1, \ldots, N]$) in a time period $[0, 1/\omega_d]$, is reduced from an initial value of 2.71μm to a final value of 0.37μm in six iteration

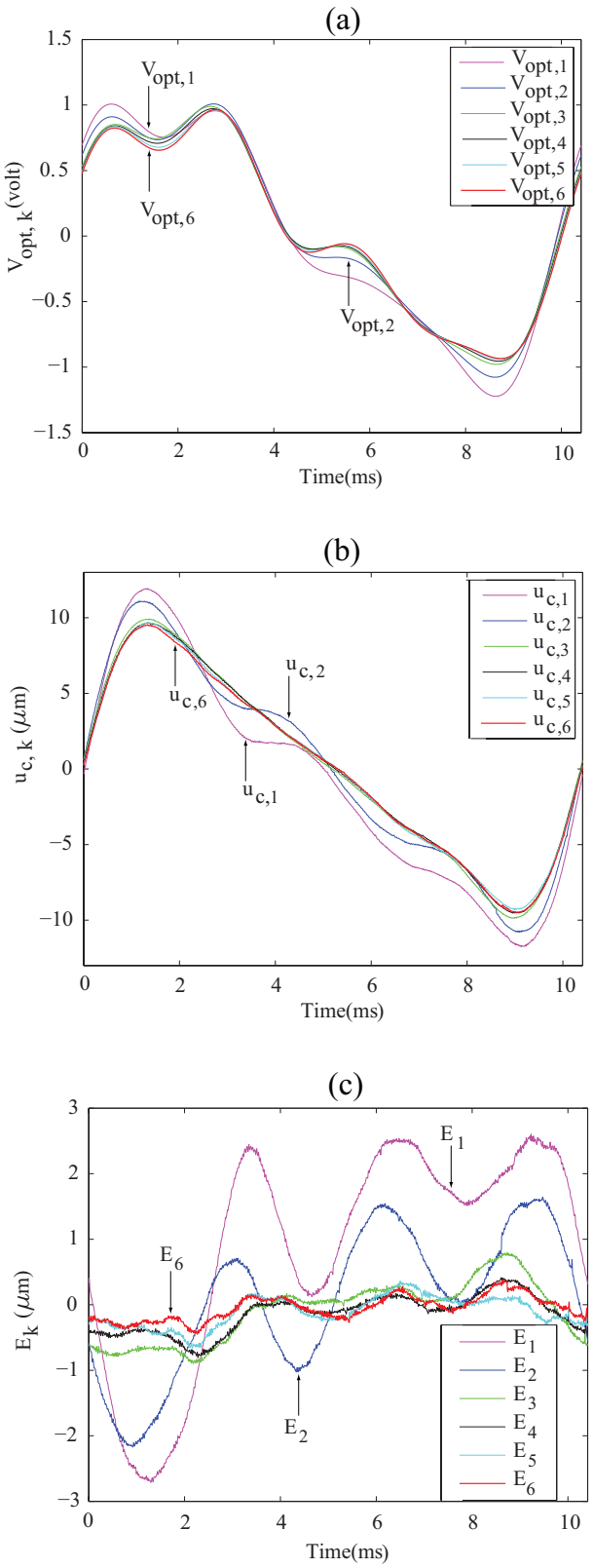

Figure 4.10: Iteration results for iteration steps k from 1 to 6: (a) optimal inverse input $V_{opt,k}$; (b) experimentally measured waveform $u_{c,k}$; and (c) error in waveform $E_k(t) = u_{c,opt}(t) - u_{c,k}(t)$.

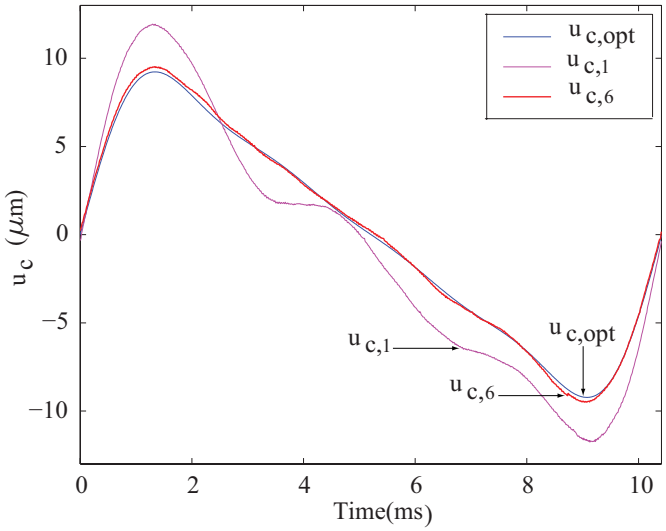

Figure 4.11: Comparison of initial $u_{c,1}$ and final ($u_{c,6}$ at iteration step 6) waveforms with the desired, optimal, asymmetric waveform $u_{c,d} = u_{c,opt}$.

Iteration Step k	$E_{k,max}$ μm	$E_{k,rms}$ μm
1	2.71	82.82
2	2.17	47.98
3	0.90	21.01
4	0.81	14.27
5	0.66	11.45
6	0.37	8.51

Table 4.2: Maximum $E_{k,max}$ and rms $E_{k,rms}$ tracking error

steps. Note that the final maximum error $E_{6,max}$ at the sixth iteration is small (1.85%) compared to the 20μm magnitude of the desired motion. Similarly, the root mean

squared (rms) of the tracking error

$$E_{k,rms} = \sqrt{\frac{\sum_{i=1}^{N}[E_k(t_n)]^2}{N}} \tag{4.9}$$

is reduced from an initial value of 82.82μm to a final value of 8.51μm in six iteration steps. For clarity, the initial $u_{c,1}$ and final ($u_{c,6}$ at iteration step 6) waveforms are compared with the desired optimal waveform $u_{c,d} = u_{c,opt}$ in Figure 4.11.

4.4 Experimental Evaluation of Mixing

The mixing of ink and water in an oscillating chamber is evaluated to show that (i) mixing time is substantially reduced with the use of cilia when compared to the case without cilia and (ii) mixing time with cilia can be further decreased by using an asymmetric excitation waveform when compared to a symmetric sinusoidal excitation.

4.4.1 Procedure for Mixing Experiments

The procedure for the mixing experiment with cilia is described below. The procedure for the mixing experiments without cilia (i.e., vibration only) is the same as the case with cilia — except that cilia are not present in the chamber. For mixing experiments with cilia, three cilia were arranged in the mixing chamber as shown in Figure 4.12. The cilia mixing device was attached to the piezoactuator as shown in Figure 4.1a,b. The cilia mixer system was positioned above an inverted microscope. After positioning the cilia mixer, de-ionized (DI) water (11μL) was added to the chamber using a pipette. Collapsed cilia, if any, were straightened by using tweezers. Next, 0.25μL of black ink (Drawing ink A, Pelikan, Hannover, Germany that is diluted 80 times with DI water) was released gently using a pipette at the center of the chamber under the water surface. The initial image of the ink drop (at time $t = 0s$) is shown in Figure 4.13. A thin PDMS sheet was placed above the chamber to enclose the mixing chamber to avoid evaporation of the solution during the mixing experiments. The

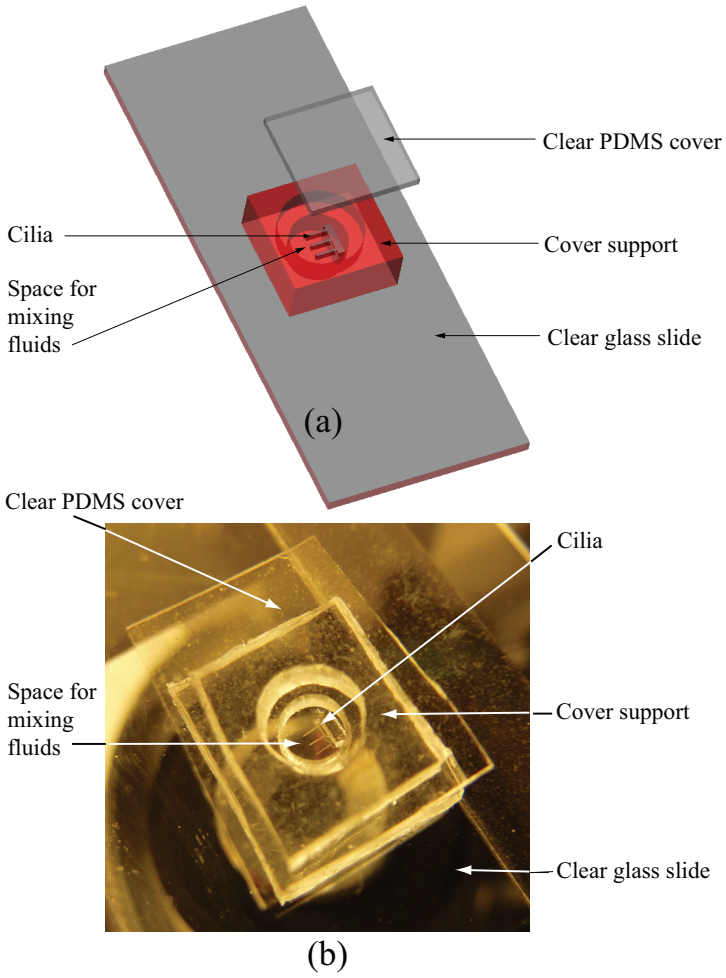

Figure 4.12: (a) Schematic and (b) photo of setup of cilia device for mixing experiments in a 3mm diameter chamber.

PDMS cover did not suppress sloshing of the free surface because the solution volume together with the cilia-support structure created a maximum water height of 1.66mm, which did not reach the top of the chamber. Additionally, a support for the cover was added (as in Figure 4.12) to prevent the cover from sagging and touching the water surface.

Subsequently, the piezoactuator was used to oscillate the chamber perpendicular to

the length of the cilia at an oscillation frequency of 96Hz. For the symmetric excitation case, the input V was chosen as a sinusoid, and for the asymmetric excitation case, the input V was chosen as the input $V_{opt,6}$ from the final (sixth) iteration step. In general, the mixing rate can be affected by the magnitude of the excitation. To enable comparisons between the different scenarios, the amplitudes of the waveforms were kept the same for all the experiments. Towards this, the amplitude of the input V to the closed-loop system (for each waveform) was scaled to ensure that the amplitude of the chamber oscillation u_c was kept the same (10μm) for both the excitation waveforms.

Each mixing experiment (with and without cilia for the two different waveforms) was repeated seven times. During each mixing experiment, the initial image was captured after the addition of ink and after the thin PDMS sheet was used to cover the chamber but just before the start of the chamber oscillations with the piezoactuator. Preliminary experiments were performed to choose a sufficiently large time for the mixing experiments such that the mixing index (described in the section below) reaches a steady state value. Based on these preliminary studies, the time t_N for the final image was chosen as 50s for the case with cilia and 600s for the case without cilia. Additionally, the images were inspected to visually verify that they do not change significantly when the last images were collected.

The time for the mixing index to reach and stay within 90% of its final value is used to quantify and comparatively evaluate the mixing performance with and without cilia for the two different waveforms. A CCD camera, attached to the microscope (see Figure 4.1a), was used to video-record the mixing process for evaluation — samples of the acquired images are shown in Figure 4.13.

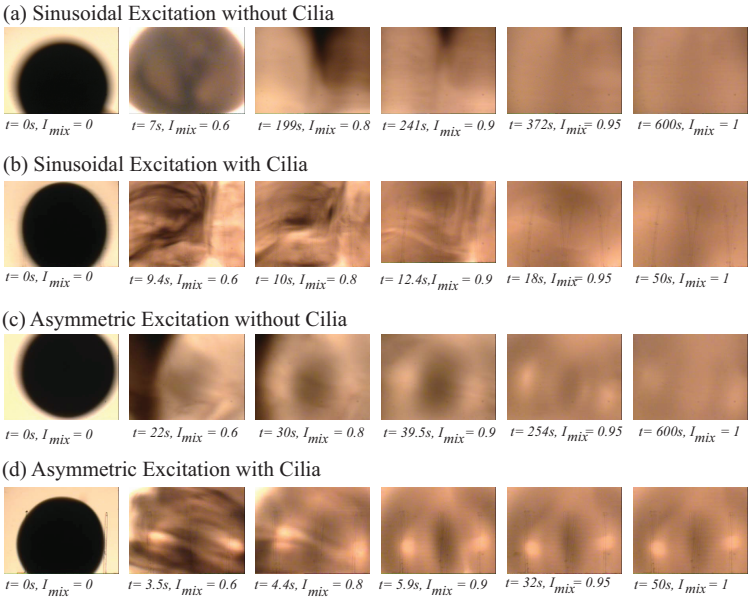

Figure 4.13: Sample images of the mixing process at different time instants t for Run 1: (a) sinusoidal excitation without cilia (b) sinusoidal excitation with cilia; (c) asymmetric excitation without cilia; and (d) asymmetric excitation with cilia.

4.4.2 Quantifying Mixing

The mixing was quantified by comparing images from the video recording of the mixing process using a mixing index I_{mix} developed in [60], which is a discrete version of the continuous time mixing index defined in [78]. The mixing index, which is a measure of relative mixing, is initially 0 and approaches 1 when the fluids become fully mixed, is given by

$$I_{mix}(t_k) = \frac{1}{I_{ss}} \left[1 - \frac{\sum_{p=1}^{P} |C_p(t_k) - C_p(t_N)|}{\sum_{p=1}^{P} |C_p(t_0) - C_p(t_N)|} \right] \tag{4.10}$$

where $[t_k]_{k=1}^{N}$ represents the different time instants when the images are evaluated, N is the total number of images, P is the number of pixels in each of the images, $C_p(t_k)$ is the color of pth pixel at time instant t_k, and the normalization factor I_{ss} is given by

$$I_{ss} = \left| 1 - \frac{\sum_{p=1}^{P} |C_p(t_{N-1}) - C_p(t_N)|}{\sum_{p=1}^{P} |C_p(t_0) - C_p(t_N)|} \right|. \tag{4.11}$$

Each image used in this analysis is composed of an array of 720 pixels by 480 pixels, and the color of each pixel C is a vector of three values

$$C \;=\; [R \;\; G \;\; B]$$

that represents red, green, and blue (RGB) color with values between 0 and 255. Given any two pixel colors C_i and C_j, the difference between them (used in Eqs. 4.10, 4.11) is defined as

$$|C_i - C_j| \;=\; |R_i - R_j| + |G_i - G_j| + |B_i - B_j|.$$

As the mixing progresses and reaches a steady state (i.e., as t_k approaches t_N), the difference between the color of the corresponding pixels in the images becomes small, which tends to increase the values of I_{mix} from an initial value of zero towards one. The normalization factor I_{ss} in Eq. (4.11) uses the last two images to make the mixing index close to one when the mixing process reaches steady state and the images become similar. This is necessary because noise in the image (partly due to the oscillation) prevents the final value from reaching one without the normalization, i.e., when the normalization factor is chosen as $I_{ss} = 1$ in Eq. (4.10). To evaluate the mixing performance and determine the effect of the input waveform, two different excitation waveforms (symmetric and asymmetric) are used to oscillate the mixing chamber for each case: with and without cilia.

4.4.3 Mixing Results

The mixing time is substantially reduced with cilia when compared to the case without cilia and it is further decreased by using asymmetric excitation compared to the case with symmetric sinusoidal excitation. The reduction in mixing time with the cilia is visually observable in the images shown in Figure 4.13 for Run 1. For example, to reach the 90% mixing time for Run 1 (corresponding to the images on the 4th column), the mixing takes 12.4s with the cilia whereas it takes 241s for the case without

the cilia for the sinusoidal excitation. The mixing time is further decreased by using asymmetric excitation compared to the case with symmetric sinusoidal excitation. For example, in Figure 4.13 with the use of the symmetric sinusoidal excitation, the mixing for Run 1 takes 12.4s with the cilia whereas with the use of the asymmetric excitation it takes 5.9s for the case with the cilia to reach the 90% mixing time.

The trends in the reduction in mixing time is also seen in averaged values over several experiments. The time variation of the mixing index (without and with cilia) are shown in Figures 4.14, 4.15 and the 90% mixing time for the different experiments are presented in Tables 4.3 and 4.4. In particular, (i) the mixing time (90%) is substantially reduced with the use of cilia when compared to the case without cilia by 13 times from $175s$ to $13.56s$ (with sinusoidal excitation) and (ii) the mixing time (90%) with cilia is further reduced (about 2.6 times from $13.56s$ to $5.17s$) by using the asymmetric excitation waveform when compared to the symmetric (sinusoidal) excitation. Thus, the experimental results show that the mixing time is substantially reduced with cilia when compared to the case without cilia. Moreover, the mixing time is further decreased by applying the asymmetric excitation waveform to oscillate the mixing chamber when compared to the case of the symmetric (sinusoidal) excitation in previous studies [2, 60].

It is noted that mixing with cilia,for both symmetric excitation and asymmetric excitation cases, can significantly reduce both the mean and the standard deviation of the 90% mixing time compared to mixing without cilia because the interfacial length between water and ink is rapidly extended by the complex flow [60].

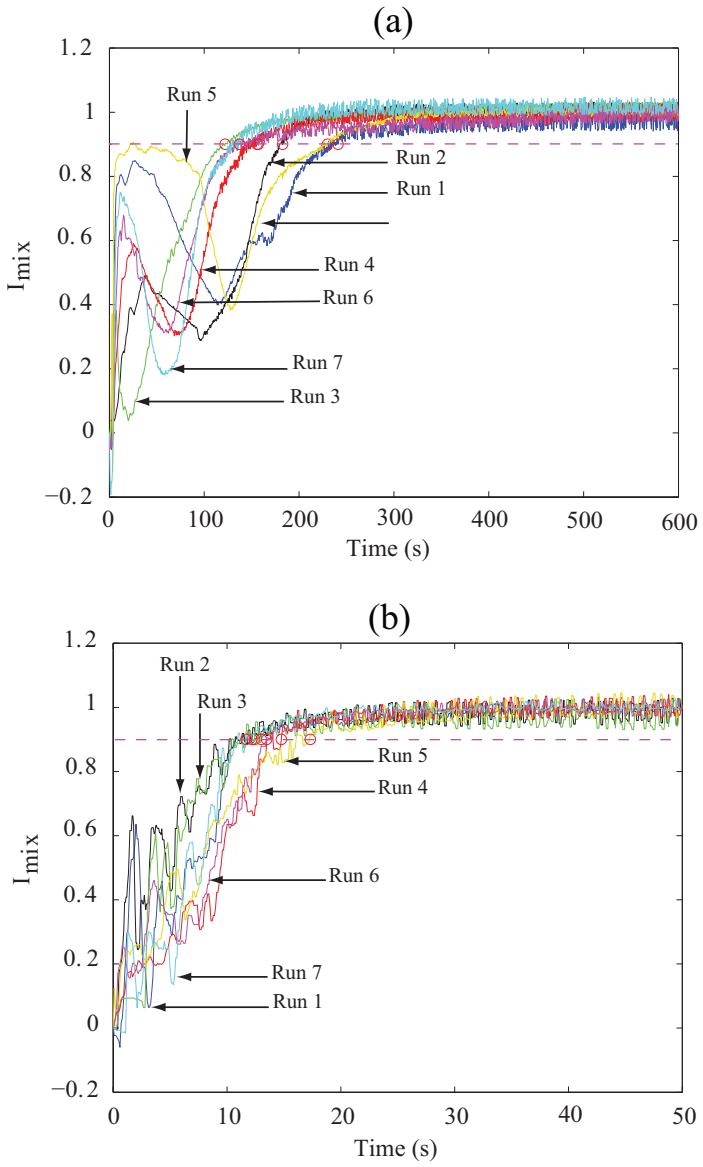

Figure 4.14: Mixing indices for devices with : (a) sinusoidal excitation without cilia, (b) sinusoidal excitation with cilia.

4.4.4 Discussion of Results

Although the asymmetric excitation leads to faster mixing, it cannot be caused by a substantial change in the cilia motion between the symmetric and asymmetric ex-

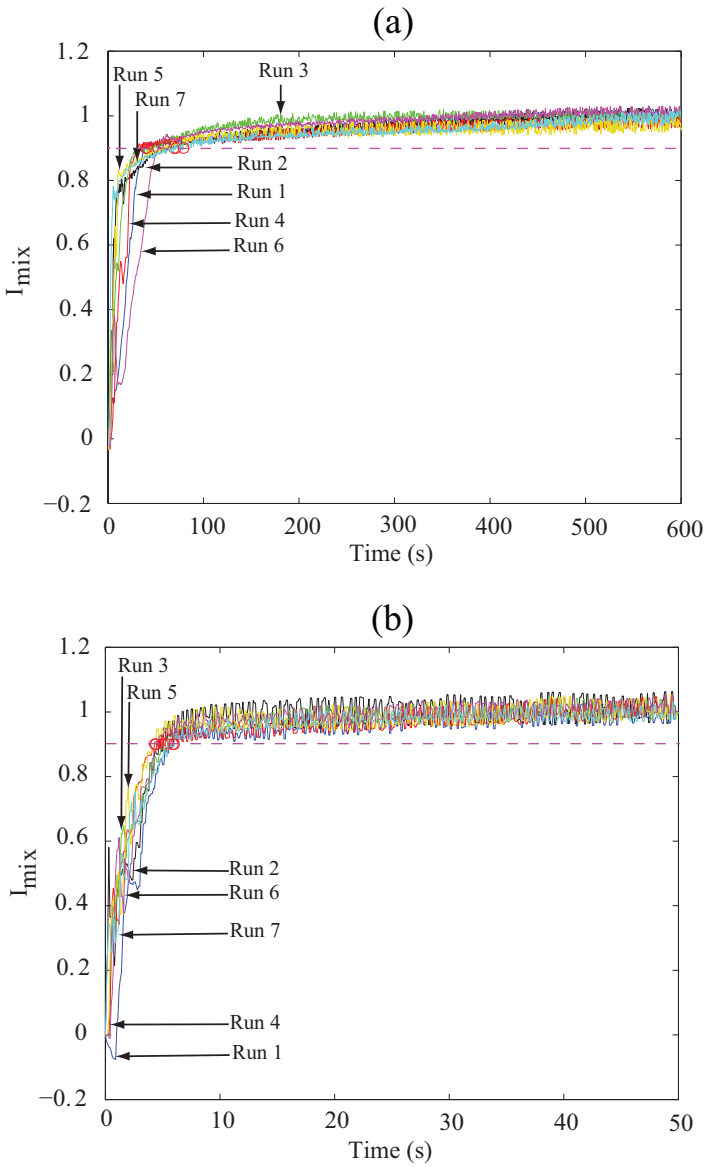

Figure 4.15: Mixing indices for devices with : (a) asymmetric excitation without cilia, (b) asymmetric excitation with cilia.

citation waveforms. This is because the cilia dynamics is only substantial near the first resonance (at around 96Hz) and therefore, the higher harmonics in the excitation waveform does not lead to substantial cilia vibration — the cilia motion is expected to remain sinusoidal due to the response caused by the main harmonic in the excitation

Run Number	Mixing Time without Cilia (s)	Mixing Time with Cilia (s)
1	241.0	12.4
2	182.5	12.2
3	122.0	13.0
4	155.5	14.8
5	230.0	17.3
6	157.0	13.5
7	137.0	11.7
Mean	175.0	13.56
σ	45.45	1.94

Table 4.3: Mixing time(s) for sinusoidal excitation, quantified by the time for the mixing index I_{mix} in Eq. (4.10) to reach and stay within 90% of its final value, without and with cilia

waveform at 96Hz. Nevertheless, the asymmetric excitation can lead to increased velocities of particles in the fluid when compared to the symmetric excitation due to increased net forcing in each period of oscillation. This can lead to faster mixing. To evaluate this, the motion of particles in the flow was evaluated using polymer microspheres (crosslinked poly(styrene/divinylbenzene), mean diameter of 18.97μm, PS07N/1733, Bangs Laboratories, Inc.) with the same operating conditions as the ink-mixing experiment (without the ink) for all four cases: (a) sinusoidal excitation without cilia; (b) sinusoidal excitation with cilia, (c) asymmetric excitation without cilia, and (d) asymmetric excitation with cilia. The results show that the microspheres actuated by the asymmetric excitation waveform have greater average speed compared to the ones with the symmetric excitation waveform as shown in Table 4.5

Run Number	Mixing Time without Cilia (s)	Mixing Time with Cilia (s)
1	39.5	5.9
2	69.0	5.0
3	48.0	5.4
4	41.0	5.2
5	71.0	4.4
6	52.5	4.3
7	79.0	6.0
Mean	57.14	5.17
σ	15.74	0.67

Table 4.4: Mixing time(s) for asymmetric excitation, quantified by the time for the mixing index I_{mix} in Eq. (4.10) to reach and stay within 90% of its final value, without and with cilia

for both cases — with and without cilia. This is to be expected since asymmetric excitation leads to a nonzero impulse over each time period when compared to symmetric excitation. Similarly, cilia also lead to increased speed of the particles, for both cases, symmetric and asymmetric excitation. Thus, there appears to be two effects: (i) the use of asymmetric excitation waveform increases the speed of particles — the increased particle speed can lead to faster mixing, with mixing time reduced by more than half; and (ii) the use of cilia increases the rate of mixing further for, both, symmetric and asymmetric excitation cases — the mixing time is reduced further by about more than an order of magnitude in each case.

In summary, the results show that the choice of the excitation waveform can improve the mixing performance, further, for cilia-based devices. This suggests the need for

Excitation Waveform	Speed without Cilia (μm/s)	Speed with Cilia (μm/s)
Sinusoidal	335.67±47.01	1026.35±214.46
Asymmetric	616.13±151.06	2317.16±304.22

Table 4.5: Speed, mean value and standard deviation for 10 microspheres for each of the four cases — without and with cilia, and symmetric (sinusoidal) and asymmetric excitation

additional research in excitation-waveform optimization for the future work.

4.5 Conclusions

An iterative, optimal-inversion-based control was used to achieve precision control of excitation waveforms applied to a novel biomimetic cilia-based mixer. Experimental results were presented to show that (i) the mixing time was substantially reduced with the use of cilia when compared to the case without cilia by 13 times (with sinusoidal excitation) and (ii) the mixing time with cilia can be further reduced (about 2.6 times) by using an asymmetric excitation waveform when compared to the previous use of symmetric (sinusoidal) excitation. The results illustrate the need for additional optimization studies of the excitation waveform to further improve the mixing rate in cilia-based devices.

Chapter 5

CONCLUSIONS AND FUTURE WORKS

5.1 Conclusions

This research proposed and investigated biomimetic cilia-based devices (cantilever-type vibrating devices) for handling micro-scale fluid mixing. This research developed models and control methods for such devices. Three challenging research issues were addressed:

1) Added mass effect

2) Sloshing effect

3) Exploring the effect of different excitation waveforms on mixing time.

This research began with modeling the added mass effects to explain the substantial reduction in the resonant frequency and damping when shaking the cilia in otherwise still water compared to shaking the cilia in air. In the middle stage of the research project, the sloshing model was developed to explain the substantial increase in the amplitude of the cilia tip motions despite the presence of large damping in water when the whole chamber containg cilia and water was oscillated. The research finally evaluated the effect of applying the two different excitation waveforms on mixning time and found that:

(i) mixing time is substantially reduced (by more than an order of magnitude) with the use of cilia when compared to the case without cilia and

(ii) mixing time with cilia can be further reduced (by more than half) by using an asymmetric excitation waveform when compared to symmetric (sinusoidal) excitation.

5.1.1 Advantage

The mixing with the use of cilia holds several advantages. For example,
1) The use of the low actuation frequency, which leads to low shear rate, can reduce the possible damage to sensitive biosamples.
2) The soft cilia can reduce the mechanical damage to reagents.
3) The mixing with the use of cilia can reduce the mixing time.

5.1.2 Disadvantage

However, the mixing with the use of cilia has some disadvantages. For example,
1) The mixing with the use of cilia has the potential for the damage to sensitive biosamples, but the damage seems to be less. Further study on the damage is needed.
2) The manufacturing remains an issue. A large array of hundreds of cilia mixing devices needs to be manufactured for high-throughput applications and a fully automated platform is to be developed and implemented for the precise and fast handling.

5.2 Future Works

Even though this research was satisfactorily done, there are still many fascinating topics/issues that remain unexplored. For example, optimizations can be investigated to accelerate the mixing and further reduce the mixing time.
The optimization problems could be:

(i) Cilia cross section : This research used the microfabricated cilia with rectangular cross sections. The change in the cross section profile could modify the added mass effect, and thereby shifting the resonant frequency. Concave and convex cross-section cilia can be investigated to evaluate the change in the resonant frequency. The change

can be adjusted by varying the radius of the curvature of the cross section to match the sloshing resonant frequency, thereby minimzing the mixing time.

(ii) Excitation amplitude : The excitation amplitude of $20\mu m$ was set to drive the piezoactuator. Varying the excitation amplitude could lead to the minimized mixing time.

(iii) Geometry of the mixing chamber : The geometry of the mixing chamber could be optimized. For example, changing the chamber diameter can adjust the sloshing resonant frequency to match the cilia resonant frequency. Also a sloped bottom chamber could facilitate sloshing. This would provide the larger cilia tip motion that helps speed up the mixing.

(iv) Water level : Water level varies with the sloshing resonant frequency. Adjusting the water level can change the resonant frequency to match the cilia resonant frequency.

(v) Cilia floor level : At a fixed water level, adjusting the elevation of cilia floor, or support can change the cilia tip amplitude. The larger cilia tip amplitude is desired to optimize the mixing time.

(vi) Measure of time asymmetry, α as described in Figure 1.7 caption : $\alpha = 0.25$ was used in this research. It is likely that a smaller value of α could lead to faster mixing.

(vii) Cilia length: Cilia with the length of $800\mu m$ were used in the mixing experiments. The length of cilia could effect the mixing time.

(viii) Cilia spacing and configurations : The spacing between two adjacent cilia was $500\mu m$. Adjusting the spacing could find the minimized mixing time. The different configurations or arrangements of cilia in the chamber could also effect the flow pattern and the mixing time.

(ix) Phase difference between the fluid and the cilia: Phase difference between the fluid and the cilia could be maximized to possibly reduce the mixing time.

(x) Individual cilia excitation : Individaully actuated cilium is desired to provide phase/magnitude difference for each cilium. The cilia can be actuated in a coordi-

nated way as found in biological cilia to optimize the mixing time.

All of these proposed themes are worth exploring in the future works and the results could make significant contributions to accelerating micromixing and could benefit the development of the mixing device in the micro world.

BIBLIOGRAPHY

[1] J. Kongthon, B. Mckay, D. Iamratanakul, K. Oh, J.-H. Chung, J. J. Riley, and S. Devasia. Added-mass effect in modeling of cilia-based devices for microfluidic systems. *ASME Journal of Vibration and Acoustics*, 132:024501–1–024501–7, April 2010.

[2] J. Kongthon, J.-H. Chung, J. J. Riley, and S. Devasia. Dynamics of cilia-based microfluidic devices. *ASME Journal of Dynamic Systems, Measurement and Control*, 133:051012–1–051012–11, September 2011.

[3] S.Tien, Q. Zou, and S. Devasia. Iterative control of dynamics-coupling-caused errors in piezoscanners during high-speed AFM operation. *IEEE Transactions on Control Systems Technology*, 13(6):921–931, November, 2005.

[4] R. A. Johnson. *Miller and Freund's Probability and Statistics for Engineers*. Prentice-Hall, New Jersey, 6th edition, 2000.

[5] R. L. Manns. Necessity is the mother of invention–the history of microplates. *Business Briefing:Future Drug Discovery*, 2003.

[6] N.M. Cooke and P. H. Hall. Disposable microtitration plate. *Cooke Engineering Company*, December,5 1967. United States Patent US3356462.

[7] A. Smith. How small should you go? *Nature*, 418:457, July,25 2002.

[8] G. S. Jeong, S. Chung, C.-B. Kima, and S.-H. Lee. Applications of micromixing technology. *Analyst*, 135(DOI: 10.1039/b921430e):460473, January 2010.

[9] Y. Wang, J. Zhe, P. Dutta, and B. T. Chung. A microfluidic mixer utilizing electrokinetic relay switching and asymmetric flow geometries. *Journal of Fluids Engineering*, 129:395–403, April 2007.

[10] V. Hessel, H. Lowe, and F. Schonfeld. Micromixers - a review on passive and active mixing principles. *Chemical Engineering Science*, 60:2479–2501, 2005.

[11] R. H. Liu, M. A. Stremler, K. V. Sharp, M. G. Olsen, J. G. Santiago, R. J. Adrian, H. Aref, and D. J. Beebe. Passive mixing in a three-dimensional serpentine microchannel. *Journal of Microelectromechanical Systems*, 9(2), June 2000.

[12] A.D. Stroock, S.K.W. Dertinger, A. Ajdari, I. Mezic, H.A. Stone, and G.M. Whitesides. Chaotic mixer for microchannels. *Science*, 295(5555):647–651, January 25 2002.

[13] J.J. Hawkes, R.W. Barber, D.R. Emerson, and W.T. Coakley. Continuous cell washing and mixing driven by an ultrasound standing wave within a microfluidic channel. *Lab on a Chip*, 4(5):446–452, 2004.

[14] G. A. Mensing, T. M. Pearce, M. D. Graham, and D. J. Beebe. An externally driven magnetic microstirrer. *Royal Society*, 362:1059–1068, 2004.

[15] V. V. Khatavkar, P. D. Anderson, J. M. J. den Toonder, and H. E. H. Meijer. Active micromixer based on artificial cilia. *Physics of Fluids*, 19(8):083605–1–083605–13, August 2007.

[16] B. D. Storey and B. S. Tilley. Electrokinetic instabilities in thin microchannels. *Physics of Fluids*, 17:1–4, December 2005.

[17] S. M. Shin, I. S. Kang, and Y.-K . Cho. Mixing enhancement by using electrokinetic instability under time-periodic electric field. *Journal of Micromechanics and Microengineering*, 15(3), March 2005.

[18] S. K. Sia and G. M. Whitesides. Microfluidic devices fabricated in poly(dimethylsiloxane) for biological studies. *Electrophoresis*, 24:3563–3576, 2003.

[19] A. Wixforth. Acoustically driven programmable microfluidics for biological and chemical applications. *Journal of the Association for Laboratory Automation*, 11(6):399–405, December 2006.

[20] R.H.Liu, J. Yang, M.Z. Pindera, M. Athavale, and P. Grodzinski. Acoustic microstreaming for biological sample mixing enhancement. pages 545–550, Madison, WI , USA, August 2002. Microtechnologies in Medicine and Biology 2nd Annual International IEEE/EMB Special Topic Conference, IEEE.

[21] M. Grumann, A. Geipe, L. Riegger, R. Zengerle, and J. Ducree. Batch-mode mixing on centrifugal microfluidic platforms. *Lab on a Chip*, 5(5):560–565, 2005.

[22] S.-C. Wang, Y.-W. Lai, Y. Ben, and H.-C. Chang. Microfluidic mixing by dc and ac nonlinear electrokinetic vortex flows. *Journal of Industrial and Engineering Chemistry Research,American Chemical Society*, 43:2902–2911, March 2004.

[23] C. R. Thomas and D. Geer. Effects of shear on proteins in solution. *Biotechnol Lett*, 33(DOI 10.1007/s10529-010-0469-4):443–456, November 2011. Springer Science+Business Media B.V. 2010.

[24] O. Tabata, H. Hirasawa, S. Aoki, R. Yoshida, and E. Kokufuta. Ciliary motion actuator using self-oscillating gel. *Sensors and Actuators a-Physical*, 95:234–238, January 2002.

[25] Y. Tanaka, K. Morishima, A. Kikuchi T. Shimizu, M. Yamato, T. Okano, and T. Kitamori. Demonstration of a PDMS-based bio-microactuator using cultured cardiomyocytes to drive polymer micropillars. *Lab on a Chip*, 6:230–235, February 2006.

[26] B. A. Evans, A. R. Shields, R. Lloyd Carroll, S. Washburn, M. R. Falvo, and R. Superfine. Magnetically actuated nanorod arrays as biomimetic cilia. *Nano Letters*, 7:1428–1434, 2007.

[27] H. Lai and N. P. Singh. Acute exposure to a 60 Hz magnetic field increases DNA strand breaks in rat brain cells. *Bioelectromagnetics*, 18:156–165, 1997.

[28] J. Toonder, F. Bos, D. Broer, L. Filippini, M. Gillies, J. Goede, T. Mol, M. Reijme, W. Talen, H. Wilderbeek, V. Khatavkar, and P. Andersson. Artificial cilia for active micro-fluidic mixing. *Lab on a Chip*, 8:533–541, 2008.

[29] S. W. Lee and Y. C. Tai. A micro cell lysis device. *Sensors and Actuators A-Physical*, 73:74–79, March 1999.

[30] T. L. Sounart, T. A. Michalske, and K. R. Zavadil. Frequency-dependent electrostatic actuation in microfluidic MEMS. *Journal of Microelectromechanical Systems*, 14:125–133, February 2005.

[31] H.-B. Lee, K. Oh, W.-H. Yeo, T.-R. Lee, Y.-S. Chang, J.-B. Choi, K.-H. Lee, J. Kramlich, J. J. Riley, Y.-J. Kim, and J.-H. Chung. Enhanced bioreaction efficiency of a microfluidic mixer toward high-throughput and low-cost bioassays. *Microfluid Nanofluid*, (DOI 10.1007/s10404-011-0857-7), July 2011. Springer-Verlag 2011.

[32] K.Oh, J.-H.Chung, S. Devasia, and J.J.Riley. Bio-mimetic silicone cilia for microfluidic manipulation. *Lab on a Chip by the Royal Society of Chemistry*, 9(11):1561–1566, 2009.

[33] J. Kongthon and S. Devasia. Feedforward control of piezoactuator for evaluating cilia-based micro-mixing. *18th IFAC World Congress, Milan, Italy, (Also Submitted to IEEE/ASME Transactions on Mechatronics)*, August 28 - September 2 2011.

[34] J. Kongthon and S. Devasia. Iterative control of piezoactuator for evaluating biomimetic, cilia-based micromixing. *IEEE/ASME Transactions on Mechatronics*. Submitted on October 05,2011.

[35] K. Yum, Z. Wang, A. P. Suryavanshi, and M.-F. Yu. Experimental measurement and model analysis of damping effect in nanoscale mechanical beam resonators in air. *Journal of Applied Physics*, 96(7):3933–3938, October 2004.

[36] C. Zhang, G. Xu, and Q. Jiang. Analysis of the air-damping effect on a micromachined beam resonator. *Mathematics and Mechanics of Solids*, 8:315–325, 2002.

[37] W. Zhang and K. Turner. Frequency dependant fluid damping of micro/nano flexural resonators: Experiment, model and analysis. *Sensors and Actuators*, 2006.

[38] C. E. Miller. The kinematics and dynamics of ciliary fluid systems. *Journal of Experimental Biology*, 49:617–629, January 1968. Printed in Great Britain.

[39] A.M. Sleigh. *Cilia and Flagella*. Academic Press, New York, 1974.

[40] C. Brennen. An oscillating-boundary-layer theory for ciliary propulsion. *Journal of Fluid Mechanics*, 65(4):799–824, 1974.

[41] E. O. Tuck. A note on a swimming problem. *Journal of Fluid Mechanics*, 31:305–308, 1968.

[42] M. Ramia, D. L. Tullock, and N. Phanthien. The role of hydrodynamic interaction in the locomotion of microorganisms. *Biophysical Journal*, 65:755–778, 1993.

[43] S. Gueron and K. Levit-Gurevich. Computation of the internal forces in cilia: Application to ciliary motion, the effects of viscosity, and cilia interactions. *Biophysical Journal*, 74:1658–1676, 1998.

[44] C. R. Bovender. Nasal filter. *United States Patent*, (United States Patent 4052983), October 1977.

[45] M. Ataka, A. Omodaka, N. Takeshima, and H. Fujita. Fabrication and operation of polyimide bimorph actuators for a ciliary motion system. *Journal of Microelectromechanical Systems*, 2(4):146–150, December 1993.

[46] Z. Chen, S. Shatara, and X.B. Tan. Modeling of biomimetic robotic fish propelled by an ionic polymer-metal composite caudal fin. *IEEE-ASME Transactions on Mechatronics*, 15(3):448–459, June 2010.

[47] B. Behkam and M. Sitti. Design methodology for biomimetic propulsion of miniature swimming robots. *Journal of Dynamic Systems Measurement and Control*, 128(1):36–43, March 2006.

[48] P.V.Y. Alvarado and K. Youcef-Toumi. Design of machines with compliant bodies for biomimetic locomotion in liquid environments. *Journal of Dynamic Systems Measurement and Control*, 128(1):3–13, March 2006.

[49] M. T. A. Saif, B. E. Alaca, and H. Sehitoglu. Analytical modeling of electrostatic membrane actuator for micro pumps. *IEEE Journal of Microelectromechanical Systems*, 8(3):335–345, September 1999.

[50] R. Dreyfus, J. Baudry, M.L. Roper, M. Fermigier, H.A. Stone, and J. Bibette. Microscopic artificial swimmers. *Nature*, 437(7060):862–865, October 6 2005.

[51] D.E. Hill and J.R. Baumgarten. Control of spin-stabilized spacecraft with sloshing fluid stores. *Journal of Dynamic Systems Measurement and Control*, 114(4):728–731, December 1992.

[52] R.A. Ibrahim. *Liquid Sloshing Dynamics: Theory and Applications*. Cambridge University Press, New York, 2005.

[53] G. G. Stokes. On the effect of the internal friction of fluids on the motion of pendulums. *Transactions of the Cambridge Philosophical Society*, 9(2):8–106, December 1850.

[54] N. M Ferrers. *Researches on the Vibration of Pendulums in Fluid Media*. Chelsea Publishing, New York, 1970. Mathematical Papers of George Green.

[55] U.S. Lindholm, D.D. Kana, W.-H. Chu, and H.N. Abramson. Elastic vibration characteristics of cantilever plates in water. *Journal of Ship Research*, 9:11–22, June 1965.

[56] L. D. Landau and E. M. Lifshitz. *Fluid Mechanics, Section 24, 2nd ed.* Pergamon Press.

[57] G. G. Yaralioglu, I. O. Wygant, T. C. Marentis, and B. T. Khuri-Yakub. Ultrasonic mixing in microfluidic channels using integrated transducers. *Analytical Chemistry*, 76:3694–3698, 2004.

[58] M. Herrmann, T. Veres, and M. Tabrizian. Enzymatically-generated fluorescent detection in micro-channels with internal magnetic mixing for the development of parallel microfluidic elisa. *Lab on a Chip*, 6(4):555–560, 2006.

[59] M. Vilfan, A. Potočnik, B. Kavčič, N. Osterman, I. Poberaj, A. Vilfan, and D. Babič. Self-assembled artificial cilia. *Proceedings of the National Academy of Sciences of the USA*, 107(5):1844–1847, February 2 2010.

[60] K. Oh, B. Smith, S. Devasia, J.J. Riley, and J.-H. Chung. Characterization of mixing performance for bio-mimetic silicone cilia. *Microfluidics and Nanofluidics*, 9(4-5):645–655, February 2010. Springer-Verlag.

[61] S. Devasia, E. Eleftheriou, and S. O. Reza Moheimani. A survey of control issues in nanopositioning. *IEEE Transactions on Control Systems Technology*, 15(5):802–823, Sept, 2007.

[62] H. Monnier, A. M. Wilhelm, and H. Delmas. Effects of ultrasound on micromixing in flow cell. *Chemical Engineering Science*, 55:4009–4020, 2000.

[63] D. L. Miller, R. M. Thomas, and R. L. Buschbom. Comet assay reveals DNA strand breaks induced by ultrasonic cavitation in vitro. *Ultrasound in Med. and Biol.*, 21(6):841–848, 1995.

[64] E. A. Mansur, Y. Mingxing, W. Yundong, and D. Youyuan. A state-of-the-art review of mixing in microfluidic mixers. *Chinese Journal of Chemical Engineering*, 16(4):503–516, August 2008.

[65] M. M. Rageh, A. El-Lakkani, M. H.M.Ali, A. M. M. Abd El-Fattah, and A. El-Ghreeb Raafat. Effect of high power ultrasound on aqueous solution of DNA. *International Journal of Physical Sciences*, 4(2):063–068, February 2009.

[66] J.W.M. Chon, P. Mulvaney, and J.E. Sader. Experimental validation of theoretical models for the frequency response of atomic force microscope cantilever beams immersed in fluids. *Journal of Applied Physics*, 87(8):3978–3988, April 2000.

[67] D.W. Burns, J.D.Zook, R.D. Horning, W.R.Herb, and H.Guckel. Sealed-cavity resonant microbeam pressure sensor. *Sensors Actuators,A*, 48:179–186, 1995.

[68] D.W. Burns, R.D. Horning, W.R.Herb, J.D.Zook, and H.Guckel. Sealed-cavity resonant microbeam accelerometer. *Sensors Actuators,A*, 53:249–255, 1996.

[69] W. E. Newell. Miniturization of tuning forks. *Science*, 161:1320–1326, September 1968.

[70] N. S. Nise. *Control Systems Engineering, 4th ed.* Wiley, Hoboken,NJ, 4 edition, 2004.

[71] M.K.A Hosseini, O. Omidi, A. Meghdari, and G.Vossoughi. A composite rigid body algorithm for modeling and simulation of an underwater vehicle equipped with manipulator arms. *Journal of Offshore Mechanics and Arctic Engineering*, 128:119–132, May 2006.

[72] D.W.Dareing, T. Thundat, S. Jeon, and M. Nicholson. Modal analysis of microcantilever sensors with environmental damping. *Journal of Applied Physics*, 97:1–6, December 2005.

[73] D. J. Inman. *Engineering Vibration,2nd ed.* Prentice Hall, New Jersey, 2 edition, 2001.

[74] B. M. Sumer and J. Fredsoe. *Hydrodynamics around cylindrical structures, revised ed.* World Scientific.

[75] K.-L. Wang and T. B. Jones. Electrowetting dynamics of microfluidic actuation. *Langmuir*, 21(9):4211–4217, April 26 2005.

[76] R. D. Blevins. *Flow-Induced Vibration.* Van Nostrand Reinhold Company, New York, 1977.

[77] S. Mitra and K.P. Sinhamahapatra. Slosh dynamics of liquid-filled containers with submerged components using pressure-based finite element method. *Journal of Sound and Vibration*, 304(1-2):361–381, July 2007.

[78] N. L. Jeon, S. K. W. Dertinger, D. T. Chiu, I. S. Choi, A. D. Stroock, and G. M. Whitesides. Generation of solution and surface gradients using microfluidic systems. *Langmuir*, 16:8311–8316, July 2000.

[79] J.S. Dewey, K. Leang, and S. Devasia. Experimental and theoretical results in output- trajectory redesign for flexible structures. *ASME Journal of Dynamic Systems, Measurement, and Control*, 120(4):456–461, December, 1998.

[80] G. M. Clayton, S. Tien, K. K. Leang, Q. Zou, and S. Devasia. A review of feedforward control approaches in nanopositioning for high speed SPM. *ASME Journal of Dynamic Systems, Measurement and Control*, 131(6):1–19, Article 061001, November, 2009.

[81] S. Devasia. Should model-based inverse inputs be used as feedforward under plant uncertainty? *IEEE Transactions on Automatic Control*, 47(11):1865–1871, 2002.

Appendix A

OPTIMAL INVERSION-BASED FEEDFORWARD CONTROL OF PIEZOACTUATOR (WITHOUT FEEDBACK)

A.1 Introduction

This appendix demonstrates the application of the optimal inversion-based feedforward control scheme to track the desired trajectory or wave form without the integration of feedback control.

A challenge is that, at high frequencies, vibrations in the piezoactuator (that generates the excitation waveform) can distort the positioning achieved, and thereby, limit the ability to evaluate the effect of a desired excitation waveform on mixing. This work uses feedforward control to account for the vibrational dynamics and avoid unwanted vibrations in the achieved positioning.

The result shows that there is a bump on the wave form obtained from this technique as it is shown in Figure A.7c and the wave form may not be suitable for evaluating the effect of a desired excitation waveform on mixing time. Thus, the model-based optimal inverse without feedback loop may not be used to design and track an excitation waveform for this particular system.

The integration of the feedback loop into the feedforward control is implemented in Chapter 4 to improve the trajectory and to allow the evaluation of the effect of a desired excitation waveform on mixing time.

A.2 Problem Formulation

A.2.1 System Description

The displacement transverse to the length (x) of a cilium is excited by using a piezoactuator (Burleigh PZS200) as shown in Figure A.1. The soft cilia are fabricated from polydimethylsiloxane (PDMS) using a silicon mold and detailed information on cilia fabrication and material properties can be found in [32]. The dimensions of the silicon mold used to fabricate the cilia are length ($L = 800\mu m$), height ($H = 45\mu m$),

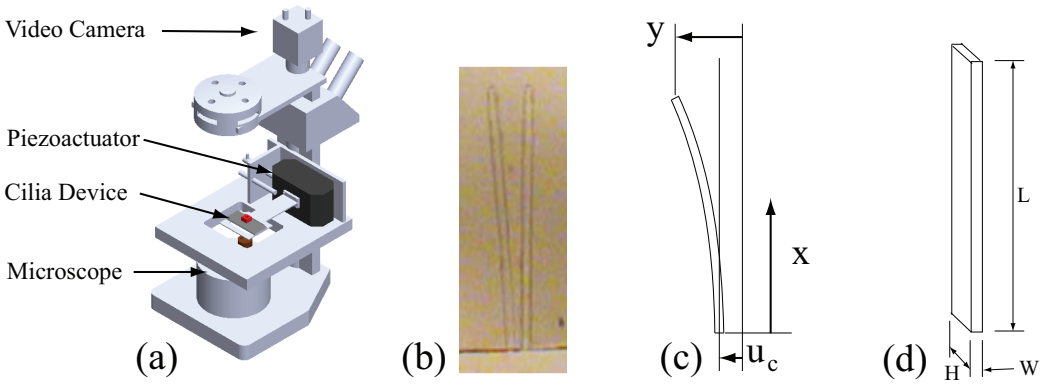

Figure A.1: Schematics of experiment for evaluating micro-mixing with cilia. (a) Experimental setup. (b) Image of a cilium in water excited by piezoactuator. (c) Base motion $u_c(t)$ at $x = 0$ and tip motion $y(t)$ at the free end $x = L$ of a cilium. (d) Nominal cilium dimensions are length $L = 800\mu m$, width $W = 10\mu m$, and height $H = 45\mu m$.

and width ($W = 10\mu m$). The cilia and the fluid in the chamber are observed and evaluated using videos obtained with an optical microscope and an attached, digital, color CCD camera, as well as, still images (Pinnacle Studio Version 12). An example image of the resulting cilia vibration (due to the chamber oscillation) is shown in Figure A.1b.

A.2.2 The Positioning Problem

An oscillatory excitation u_c of the cilia-chamber is achieved by using a piezo-based positioning system (referred to as the piezoactuator in the following) as shown in Figure A.1. The piezoactuator system is driven with input voltage V, which is amplified to V_a and applied to the piezoactuator as shown in Figure A.2. The motion of the base of each cilium is also u_c since the cilium-base is attached to the chamber through a relatively-stiff PDMS structure. To evaluate the mixing achieved with different types of excitation waveforms (i.e., time profile of u_c), the piezoactuator needs

to position the chamber precisely along the desired waveform u_c. At high oscillation frequencies, vibrations in the piezoactuator positioning system can lead to distortions in the achieved position trajectory (excitation waveform), which make it challenging to evaluate specific excitation waveforms. The control goal is to correct for such vibration-caused distortions.

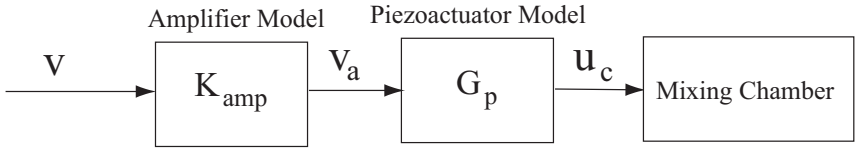

Figure A.2: Block diagram of the positioning system. An input voltage V is amplified by K_{amp} to V_a and applied to the piezoactuator (model G_p). The amplifier gain K_{amp} is adjusted to achieve a fixed-amplitude for the excitation waveforms u_c applied to the cilia-containing chamber. Such fixed-amplitude motion of the cilia chamber enables the comparative evaluation of mixing with different excitation waveforms u_c.

A.3 Feedforward Control of Piezoactuator

The modeling of the piezoactuator, the design of the excitation waveforms, and model-based feedforward control are discussed in this section.

A.3.1 Piezoactuator Model

The model of the piezoactuator (G_p in Figure A.2) is obtained experimentally. In particular, experimental frequency responses are obtained by using a dynamic signal analyzer (SRS Model SR785) at different input voltage V_a amplitudes as shown in Figure A.3. A fit of the experimental response is obtained using Matlab and the resulting model G_p is described by the following transfer function

$$G_p(s) = \frac{u_c(s)}{V_a(s)} = k\prod_i^N \frac{(s - z_i)}{(s - p_i)} \tag{A.1}$$

where the poles p_i, zeros z_i and gain k are listed in Table A.1. The frequency response of the model matches the experimentally obtained frequency responses till about 500Hz as seen in Figure A.3.

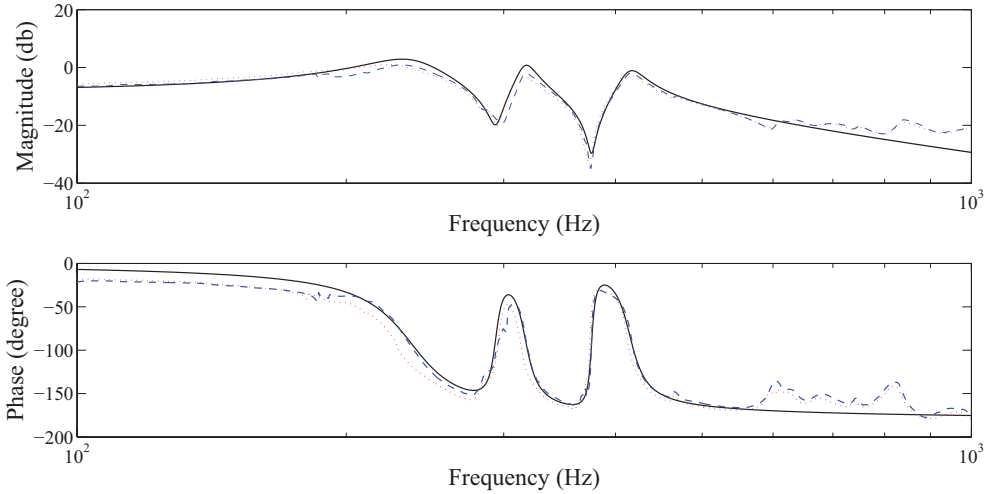

Figure A.3: Experimental and model-based frequency response of piezoactuator G_p in Figure A.2. Experimental responses are shown for two different input amplitude levels: the dashed line represents the response with input voltage $V_a = 11.2$V peak-peak; and the dotted line represents the response with $V_a = 16$V peak-peak. The response of the fitted model G_p (in Eq. A.1) is represented by the solid line.

A.3.2 Issues in Tracking the Desired Excitation Waveforms

Two types of excitation waveforms are considered; sinusoidal excitation (used in [2, 60]), and a nominal sawtooth excitation as shown in Figure A.4.

The sinusoidal excitation u_c is relatively easy to achieve. The input voltage V to the amplifier (in Figure A.2) can be chosen as the same sinusoidal excitation waveform u_c in Figure A.2 and the amplifier gain K_{amp} can be adjusted till the output position of the piezoactuator u_c has the desired peak-to-peak amplitude of $20\mu m$. On the

Poles, p_i	$(-23.95 \pm 235.56i)2\pi$
	$(-7.78 \pm 316.89i)2\pi$
	$(-13.25 \pm 414.64i)2\pi$
Zeros, z_i	$(-4.41 \pm 293.87i)2\pi$
	$(-3.01 \pm 376.16i)2\pi$
Gain, k	1206400

Table A.1: Parameters of piezoactuator model G_p in Eq. (A.1)

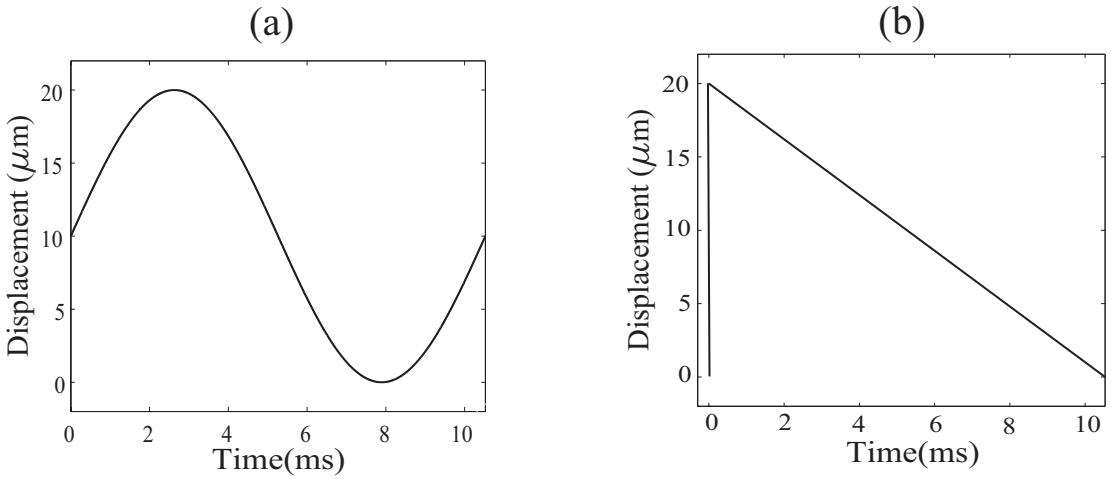

Figure A.4: Excitation waveforms u_c for one time period: (a) sinusoidal waveform, (b) sawtooth waveform.

other hand, if the nominal sawtooth profile in Figure A.4b is applied (after amplification) as a feedforward voltage V_a to the piezoactuator system (see Figure A.2), then substantial unwanted oscillations are to be expected in the achieved positioning u_c due to vibrations excited in the piezoactuator dynamics. Since vibrations distort the excitation waveform u_c, which makes it difficult to evaluate the mixing performance of a desired waveform (as discussed before). On the other hand, it is difficult to track

the sawtooth waveform since it has substantial high-frequency harmonics, which are beyond the positioning bandwidth of the piezoactuator. Therefore, in the following, an optimal inversion method is used to reduce the vibrational effects.

.

A.3.3 Optimal Inversion

Optimal inversion can be used to achieve a compromise between the goal of exact tracking the desired trajectory and handling actuator bandwidth limitations [79]. Moreover, the approach can be used to handle potential uncertainties in the model as shown in [81]. Most piezoactuators tend to have some frequency regions where plant uncertainty is unacceptably large — usually at high frequencies and close to the vibrational resonances. Moreover, the frequency response can be amplitude dependent due to hysteresis nonlinearities as seen in Figure A.3. The optimal inverse allows the inverse to be computed only in frequency regions where the uncertainty (in the linearized model G_p) is "sufficiently" small. The optimal inverse $v_a = v_{a,opt}$ is obtained by minimizing the following cost function

$$J(V_a) = \int_{-\infty}^{\infty} \{V_a^*(j\omega)R(j\omega)V_a(j\omega) + E_P^*(j\omega)Q(j\omega)E_P(j\omega)\}d\omega, \tag{A.2}$$

where $*$ denotes the complex conjugate transpose and

$$E_P = u_c - u_{c,d}$$

is the positioning error with respect to a given desired excitation waveform $u_{c,d}$. The terms $R(j\omega)$ and $Q(j\omega)$ are real-valued, frequency-dependent weightings that penalize the size of the input V_a and the positioning error E_P. If the model uncertainty is large at some frequency ω, then the choice of weights $R(j\omega) > 0$ and $Q(j\omega) = 0$ results in a minimum cost with zero input $V_a(j\omega) = 0$, i.e., no tracking at that frequency.

The optimal inverse input $V_{a,opt}$ minimizing the cost function can be found, for the single-input-single-output (SISO) case as [79]

$$\begin{aligned} V^*_{a,opt}(j\omega) = & \left[\frac{{G_p}^*(j\omega)Q(j\omega)}{R(j\omega)+{G_p}^*(j\omega)Q(j\omega)G_p(j\omega)}\right] u_{c,d}(j\omega) \\ = & \; G^{-1}_{p,opt}(j\omega)u_{c,d}(j\omega) \end{aligned} \tag{A.3}$$

and the time-domain signal for the feedforward input

$$V^*_a(t) = V^*_{a,opt}(t)$$

is then obtained through an inverse Fourier transform of $V^*_{a,opt}(j\omega)$. The optimal inverse (in Eq. A.3) can be expressed as

$$\begin{aligned} G^{-1}_{p,opt}(j\omega) = & \left[\frac{{G_p}^*(j\omega)Q(j\omega)G_p(j\omega)}{R(j\omega)+{G_p}^*(j\omega)Q(j\omega)G_p(j\omega)}\right] {G_p}^{-1}(j\omega) \\ = & \; \rho_{opt}(j\omega){G_p}^{-1}(j\omega) \end{aligned} \tag{A.4}$$

Therefore, the optimal inverse can be considered as a frequency weighted inverse.

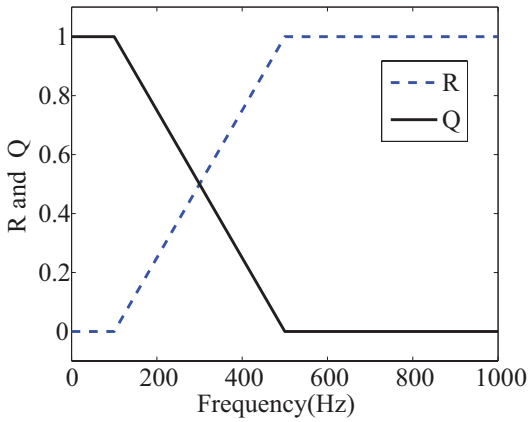

Figure A.5: Input energy weight, $R(j\omega)$ and tracking-error weight, $Q(j\omega)$ used in the cost function (in Eq. A.2) to find the optimal inverse.

A.3.4 Choosing the Weights in the Cost Function

The weights R, Q in the cost function (in Eq. A.2) can be used to account for model uncertainty and piezoactuator constraints by appropriately choosing the input-energy weight, $R(j\omega)$ and the tracking-error weight, $Q(j\omega)$. In particular, the weights can be chosen such that good tracking is achieved in the low- frequency range (till 100Hz for the cilia-based mixing device) and to reduce the emphasis on tracking at at high frequencies where the model G_p (in Eq. A.1) tends to become less accurate, e.g., beyond 500Hz for the piezoactuator model. This implies that the tracking-error weight Q should be larger than the input energy weight R in the low-frequency range and vice versa in the high-frequency range, as shown in Figure A.5.

A.3.5 Optimal Excitation Waveform

The optimal input $V^*_{a,opt}$ scaled by a factor K_{opt} , i.e.,

$$V_a = V_{a,opt} = V^*_{a,opt} K_{opt}$$

to achieve the desired peak-to-peak amplitude of $20\mu m$ of the corresponding excitation waveform $u_{c,opt}$ is shown in Figure A.6a. The resulting output of the piezoactuator, i.e., the optimal excitation waveform

$$u_{c,opt} \;=\; G_p V_{a,opt}$$

is shown in Figure A.6b. To illustrate the importance of accounting for the vibrational dynamics, the response $u_{c,DC}$ of the piezoactuator when the input V_a is chosen as a scaled version $V_{a,DC}$ of the optimal output $u_{c,opt}$, i.e.,

$$V_{a,DC} \;=\; K_{DC} u_{c,opt} \tag{A.5}$$

$$u_{c,DC} \;=\; G_p V_{a,DC} \;= G_p K_{DC} u_{c,opt} \tag{A.6}$$

is shown in Figure A.6a where the constant (DC-type) gain K_{DC} is chosen to achieve the desired peak-to-peak amplitude of $20\mu m$ of the corresponding excitation waveform $u_{c,DC}$ shown in Figure A.6b.

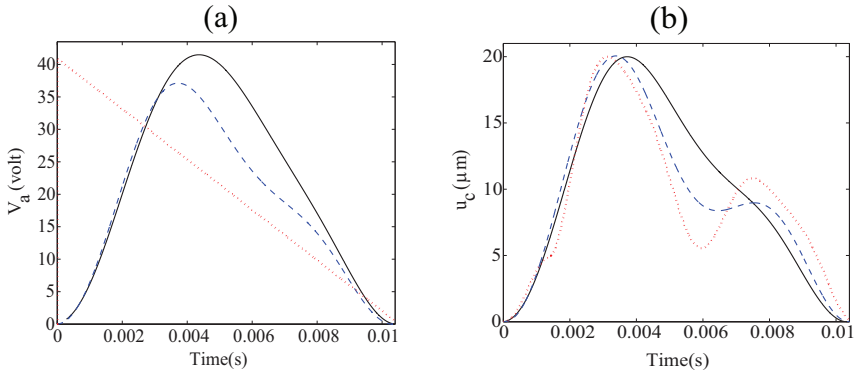

Figure A.6: Simulation results using the piezoactuator model G_p in Figure A.2. Input voltages V_a are shown in plot (a) and the corresponding responses u_c of the piezoactuator are in plot (b). Results are shown for three cases: (a) sawtooth excitation; (b) without correcting dynamics $V_{a,DC}, u_{c,DC}$; and (c) optimal input-output $V_{a,opt}, u_{c,opt}$.

Note that the achieved excitation waveform with the optimal inverse $V_{a,opt}$ has a similar asymmetry as the response achieved with the sawtooth input V_a — however, the optimal inverse reduces the oscillations due to vibrations excited in the piezoactuator as shown in Figure A.6b. The vibrational effects are reduced because the optimal inverse $V_{a,opt}$ accounts for the vibrational dynamics. In contrast, without considering the vibrational dynamics (e.g., the pair $V_{a,DC}, u_{c,DC}$), still has vibration-caused distortions — although such distortion is less when compared to the sawtooth input, which has substantially larger high-frequency content.

A.3.6 Comparison of Experimental and Simulated Waveforms

The optimal excitation waveform can be experimentally tracked without substantial distortions. For example, the simulated responses (solid lines) are compared with the experimental responses (dotted lines) in Figures A.7a-A.7c. For the sawtooth case (Figure A.7a) the experimental response has additional oscillations with period,

$T = 0.81ms$, which corresponds to a vibrational frequency of 1235Hz, which is not captured by the model G_p (in Eq. A.1). Such model errors (at high frequencies) are avoided with the optimal inverse through the choice of the input-output weights R, Q. For example, the predicted response is close to the experimental response ($u_{c,DC}$ in Figure A.7b) for the case without considering the vibrational dynamics because of smaller high-frequency components (see Eq. A.6) when compared to the sawtooth case. Note that the response to the optimal-inverse case, $V_{a,opt}$ in Figure A.7c, which takes the vibrational dynamics into account, is in a good agreement with the simulated response. The error between the simulated response and the experimental response for the optimal-inverse case is shown in Figure A.7d — the maximum error of $1.21\mu m$ is 6.05% of the $20\mu m$ peak-to-peak amplitude.

A.4 Conclusions

This appendix demonstrates the application of the optimal inversion-based feedforward control scheme to track the desired trajectory or wave form without the integration of feedback control.

The result shows that there is a bump on the wave form obtained from this technique as it is shown in Figure A.7c and the wave form may not be suitable for evaluating the effect of a desired excitation waveform on mixing time. Thus, the model-based optimal inverse without feedback loop may not be used to design and track an excitation waveform for this particular system.

The integration of the feedback loop into the feedforward control is implemented in Chapter 4 to improve the trajectory and to allow the evaluation of the effect of a desired excitation waveform on mixing time.

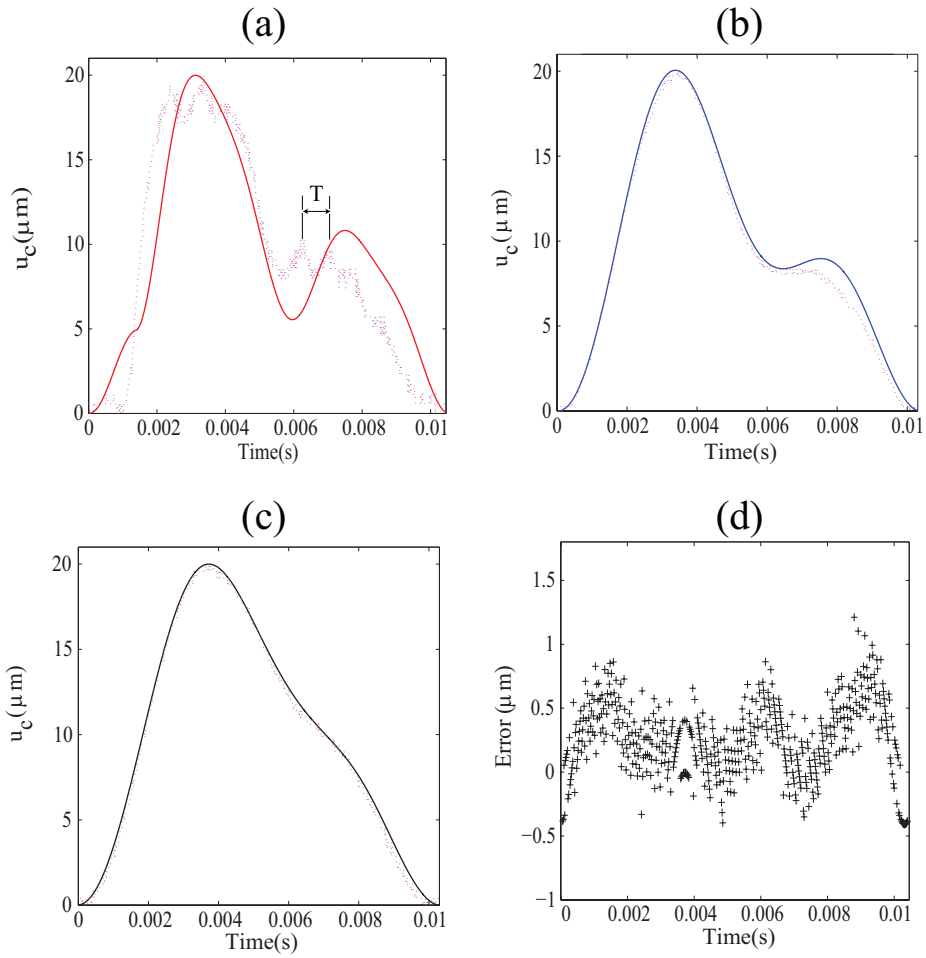

Figure A.7: Comparison of simulation and experimental results. Simulated response (solid line) and experimental response (dotted line) for three cases: (a) sawtooth excitation; (b) without correcting dynamics $V_{a,DC}, u_{c,DC}$; and (c) optimal input-output $V_{a,opt}, u_{c,opt}$. Plot (d) shows the error between the simulated response and and experimental response with the optimal input $V_{a,opt}$.

A.5 Matlab Code

The following Matlab code is used to fit the experimental frequency response in Figure A.3.

```
% this code models experimental data

close all; clear all; clc;
```

```
figure_no = 0; % figure number

Ka=10; % amplifier gain
Ks=0.2; % sensor gain
Kas=Ka*Ks;

load F5; % load the experimental frequency response data obtained from DSA
% the first column is frequency in Hz
% the second column is G(jw) a complex number
f_Hz   = f5(:,1); % frequency in Hz
f_rad  = 2*pi*f_Hz;  % frequency in radian
G      = f5(:,2); % these are complex numbers
% return
% extract the magnitude and phase information
m=(abs(G))/Kas; % the magnitude of G
m_db=20*log10(abs(G)/Kas);  % magnitude in db
p=unwrap(angle(G))*180/pi;

a1= (-0.2395e02)*2*pi;  % real part of pole 1
b1= (2.3556e02)*2*pi;  % imaginary part of pole 1
c1= (-0.0441e02)*2*pi; % real part of zero 1
d1= (2.9387e02)*2*pi;  % imaginary part of zero 1

a=a1; b=b1; c=c1; d =d1;
p1=a+b*i ; % pole 1
p2=conj(p1) ; % pole 2
z1=c+d*i ; % zero 1
z2=conj(z1); % zero 2
```

```
% transfer function 1 with dc gain adjusted
TF_1=((2.4128e+006)/Kas)*tf([1 -z1],[1 -p1])*(tf([1 -z2],[1 -p2]));

a3= (-0.0778e02)*2*pi;  % real part of pole 3
b3= (3.1689e02)*2*pi;  % imaginary part of pole 3
c3= (-0.0301e02)*2*pi; % real part of zero 3
d3= (3.7616e02)*2*pi;  % imaginary part of zero 3

a=a3; b=b3; c=c3; d =d3;
p1=a+b*i; % pole 1
p2=conj(p1); % pole 2
z1=c+d*i ; % zero 1
z2=conj(z1); % zero 2
% transfer function 2
TF_2=tf([1 -z1],[1 -p1])*(tf([1 -z2],[1 -p2]));

a5= (-0.1325e02)*2*pi;  % real part of pole 5
% one might need to tune the damping sometimes
b5= (4.1464e02)*2*pi;  % imaginary part of pole 5
c5= (-0.0034e02)*2*pi; % real part of zero 5
d5= (3.7611e02)*2*pi;  % imaginary part of zero 5

a=a5; b=b5;
p1=a+b*i ; % pole 1
p2=conj(p1); % pole 2
% transfer function 3
TF_3=tf([1],[1 -p1])*(tf([1],[1 -p2])); %
```

```
a7=-(0.1693e02)*2*pi;  % real part of pole 7
b7= (8.8382e02)*2*pi;  % imaginary part of pole 7
c7=-(0.1354e02)*2*pi; % real part of zero 7
d7= (8.7325e02)*2*pi;  % imaginary part of zero 7

a=a7; b=b7; c=c7; d =d7;
p1=a+b*i ;  % pole 1
p2=conj(p1); % pole 2
z1=c+d*i ; % zero 1
z2=conj(z1); % zero 2
% transfer function 4
TF_4=tf([1 -z1],[1 -p1])*(tf([1 -z2],[1 -p2]));

% syst_current=1; CASE=1;
syst_current=TF_1;   CASE=0;
syst_current=TF_1*TF_2;   CASE=0;
syst_current=TF_1*TF_2*TF_3;   CASE=0;
% syst_current=TF_1*TF_2*TF_3*TF_4;   CASE=0;

disp('syst_current')
GOL = syst_current % this is the model we obtain

if CASE~=1
% d=[1]
% n=[1]
% return
% let's compare the frequency responses (i.e., bode plots)
% the following generates the frequency response and store them
```

```
%H_sys1 = freqresp(GOL,f_rad); % obtain frequency response
H_sys1 = freqresp(GOL,f_rad); % obtain frequency response
Res_sys1=zeros(1,length(H_sys1(1,1,:))); Res_sys1(:)= H_sys1(1,1,:);

H_sys_current = freqresp(syst_current,f_rad); % obtain frequency response
Res_syst_current=zeros(1,length(H_sys_current(1,1,:)));
Res_syst_current(:)= H_sys_current(1,1,:);
% return
% magnitude in db and phase in degree
m_syst_current=20*log10(abs(Res_syst_current));
p_syst_current=unwrap(angle(Res_syst_current))*180/pi;

sys_extra=G./Res_syst_current(:);

else
sys_extra=G;
end

Wtfreq  =[0   160  161   200 220  245  250 255 290  295 299 300 310 ...
    312  335  340 400 450 550 551 850 855 2000];
Wtval   =[1    1    1    1   1   1   1   1  1   1   1    1   1   1 ...
    1   1  1   1   0   0   0   0   0];

Wtfreq  =[0  390 396 463 465 2000];
Wtval   =[0  0    1  1    0  0];
Wt_extra=interp1(Wtfreq, Wtval, f_Hz);

Wt_extra = ones(size(f_Hz));
```

```
% figure_no = figure_no +1; figure(figure_no)
% plot(f_Hz,Wt_extra);
% return

Nzeros_extra=2;
Npoles_extra=2;

[b,a]=invfreqs(sys_extra,f_rad,Nzeros_extra,Npoles_extra,Wt_extra);
sys_extra_tf = tf(b,a)
nume =b; dene =a;

save datamodel syst_current
% return

poles_new_Hz=pole(sys_extra_tf)/2/pi
zeros_new_Hz=tzero(sys_extra_tf)/2/pi
% return

sys_total= syst_current*sys_extra_tf
% return

poletotal_radpsec=pole(sys_total)
zerototal_radpsec=tzero(sys_total)

poletotal_Hz=pole(sys_total)/2/pi
zerototal_Hz=tzero(sys_total)/2/pi
% return
```

```
GOL = sys_total

% let's compare the frequency responses (i.e., bode plots)
% the following generates the frequency response and store them
H_sys1 = freqresp(GOL,f_rad); % obtain frequency response
Res_sys1=zeros(1,length(H_sys1(1,1,:))); Res_sys1(:)= H_sys1(1,1,:);
% magnitude in db and phase in degree
m_GOL=20*log10(abs(Res_sys1));
p_GOL=unwrap(angle(Res_sys1))*180/pi;

if CASE~=1
figure_no = figure_no +1; figure(figure_no)
subplot(2,1,1);
semilogx(f_Hz, m_db,'b:',f_Hz,m_syst_current ,'r');
title('Open Loop Frequency Response');
xlabel('Frequency (Hz)');
ylabel('Magnitude (db)');
subplot(2,1,2);
semilogx(f_Hz, p,'b:',f_Hz,p_syst_current,'r' );
xlabel('Frequency (Hz)');
ylabel('Phase (degree)');
legend('Experiment','Model',3);

else
figure_no = figure_no +1; figure(figure_no)
subplot(2,1,1);
semilogx(f_Hz, m_db,'b:');
```

```
title('Open Loop Frequency Response');
xlabel('Frequency (Hz)');
ylabel('Magnitude (db)');
subplot(2,1,2);
semilogx(f_Hz, p,'b:');
xlabel('Frequency (Hz)');
ylabel('Phase (degree)');
legend('Experiment','Model',3);
end
```

Appendix B

MAKING BIOMIMETIC CILIA AND CILIA DEVICES

This appendix describes steps on fabricating the biomimetic cilia.
The cilia are fabricated from polydimethylsiloxane (PDMS) using a microfabricated silicon mold. The nominal dimensions of the silicon mold used to fabricate the cilia used in the experiments are length ($L = 800\mu m$), height ($H = 45\mu m$), and depth ($D = 10\mu m$).
Step [1] : Weigh polydimethylsiloxane (PDMS) and curing agent (Sylgard 184 silicone elastomer curing agent) by using a scale and thoroughly mix them together with the ratio of $10 : 1$ by weight as shown in Figures B.1 and B.2.

Step [2] : Put the mixture in the vacuum chamber (as shown in Figure B.3) connected to the vacuum pump, run the pump for 2 minutes, close the valve, turn the pump off, leave the mixture in the vacuum chamber until the air bubbles induced by stirring in Step [1] are completely gone.

Step [3] : Fill and sweep the mixture onto the silicon mold in the area designed to be used as the base of cilia as shown in Figure B.4.

Step [4] : Precisely push the mixture through the view from the microscope using a clean stick till the mixture exactly touches the outlined groove connected to the grooves made for PDMS to fill up by capillary action to create the cilia structure as shown in Figure B.5.

Step [5] : Let the mixure on the mold stay at the room temperature for 20 minutes to allow the mixure to fill up the grooves completely as shown in Figure B.6 and then put it in the oven at 80 Celsius and leave it for 12 hours to have the mixture cured, as shown in Figure B.7.

Step [6] : Peel off the cured cilia structures from the mold using tweetzers as shown in Figure B.8 to get an array of cilia shown in Figure B.9.

Step [7] : Cut the array of cilia as shown in Figure B.10 to obtain a smaller array of 3 cilia and glue the cilia base support made by cured PDMS to the glass slide and cure it in the oven for 2 hours and then glue the array of 3 cilia using the mixure to the support and cure it in the oven for 2 hours to get the final assembly with the PDMS chamber, the PDMS cover support, and the cover as shown in Figure B.11.



Figure B.1: Weighing polydimethylsiloxane (PDMS) and curing agent

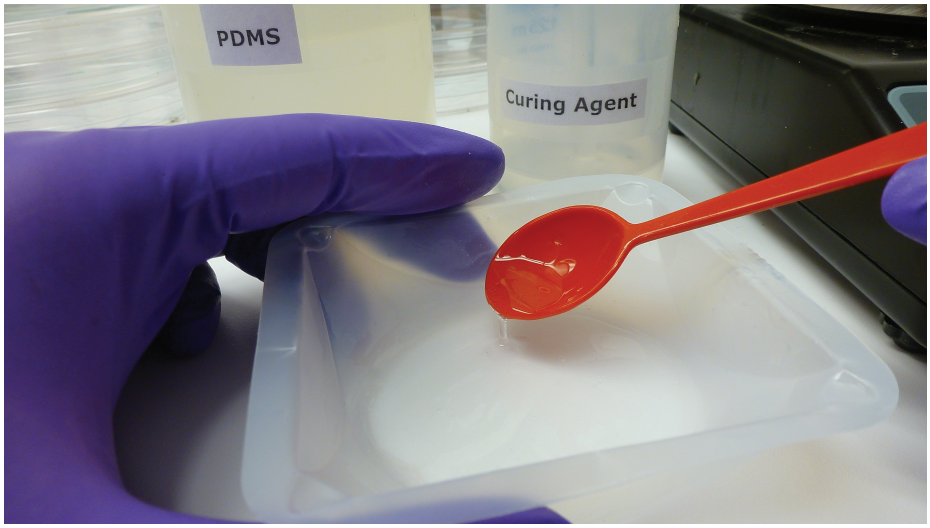

Figure B.2: Mixing polydimethylsiloxane (PDMS) with curing agent



Figure B.3: Mixture left in the vacuum chamber for air bubble removal

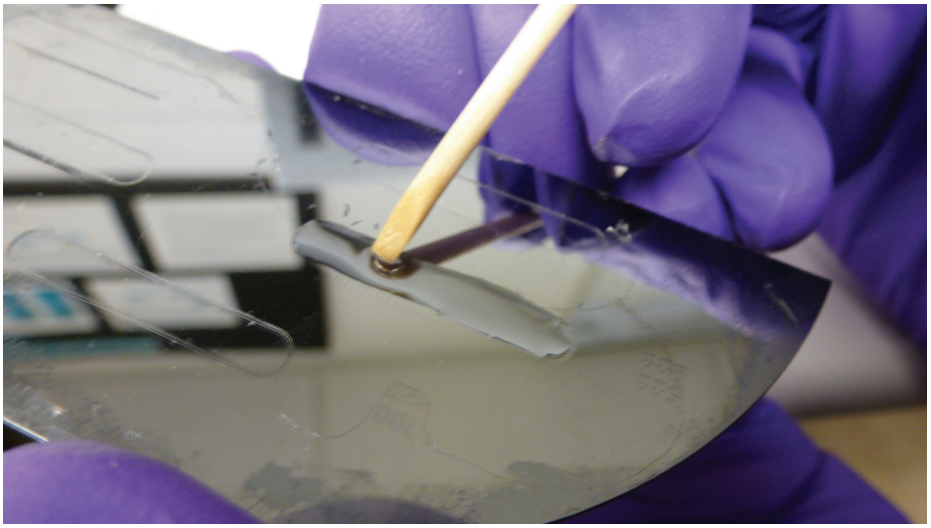

Figure B.4: Filling the mixture onto the mold

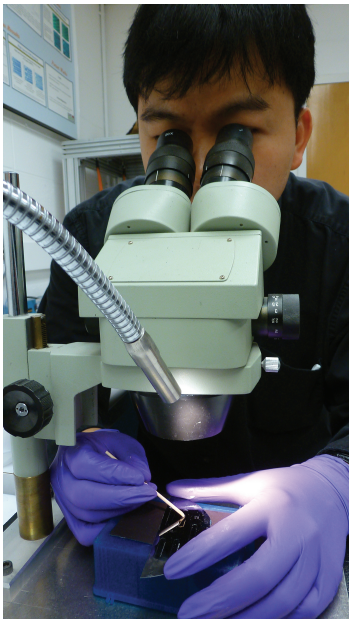

Figure B.5: Precise manipulation of the mixure through the microscope

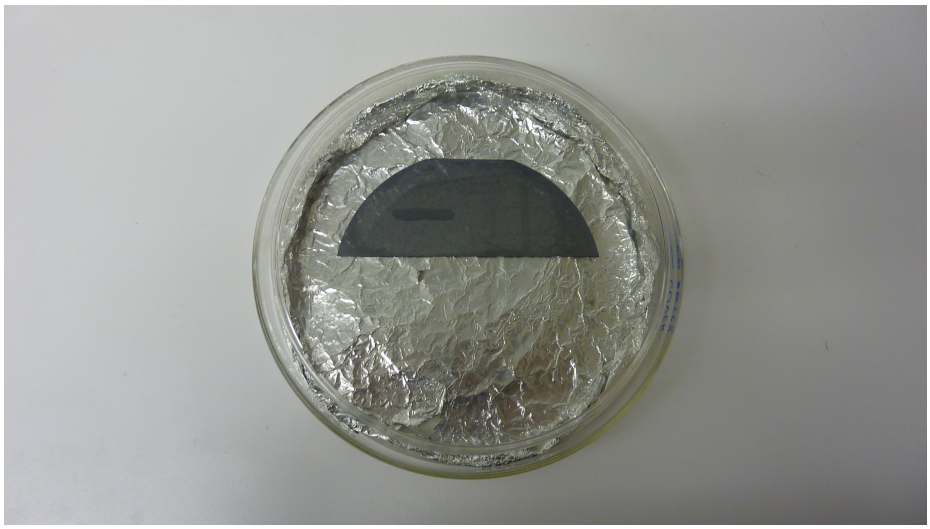

Figure B.6: Mixure on the mold left at the room temperature for 20 minutes for the complete fill-up



Figure B.7: Mixure on the mold left in the oven for 12 hours for curing

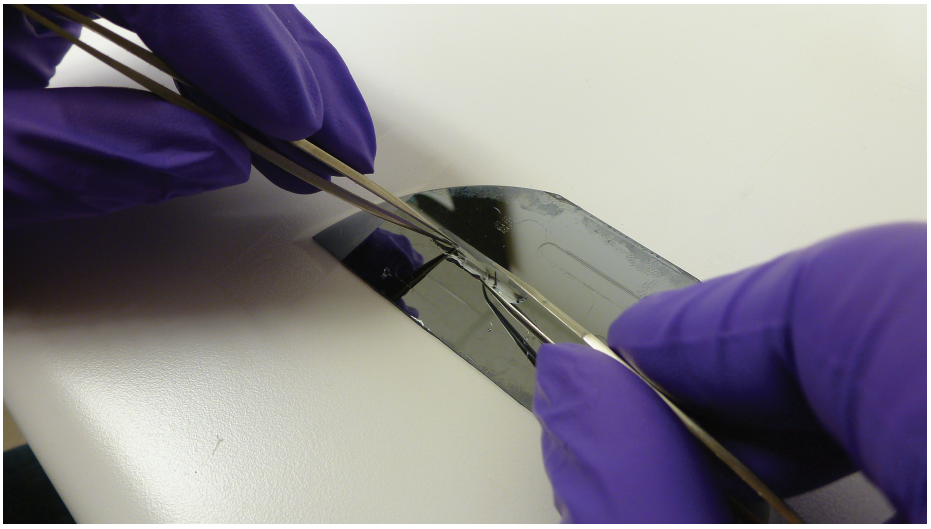

Figure B.8: Peeling off the cilia structure from the mold

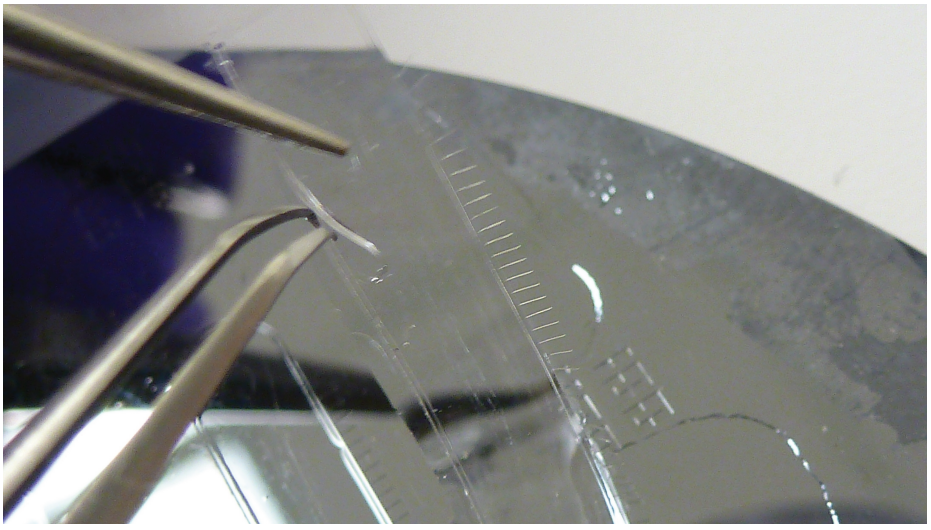

Figure B.9: An array of cilia obtained

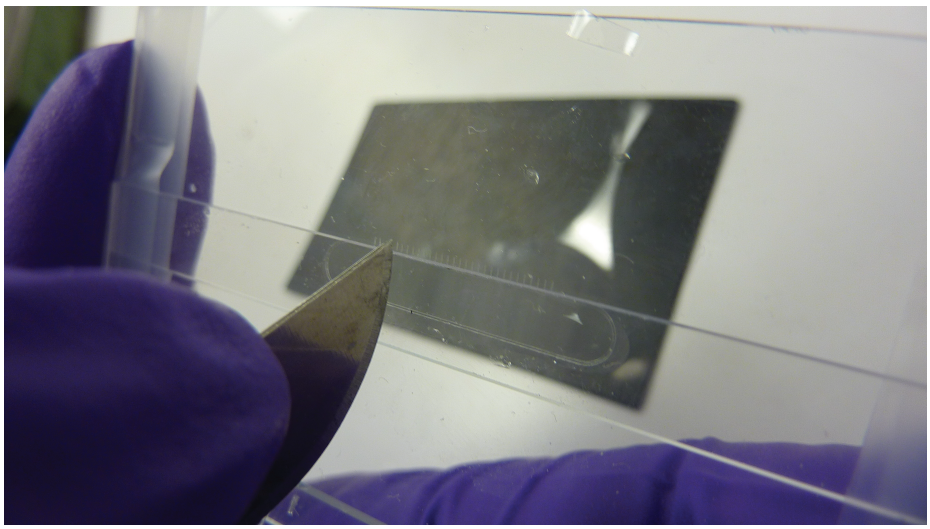

Figure B.10: Cutting the array to obtain a shorter array

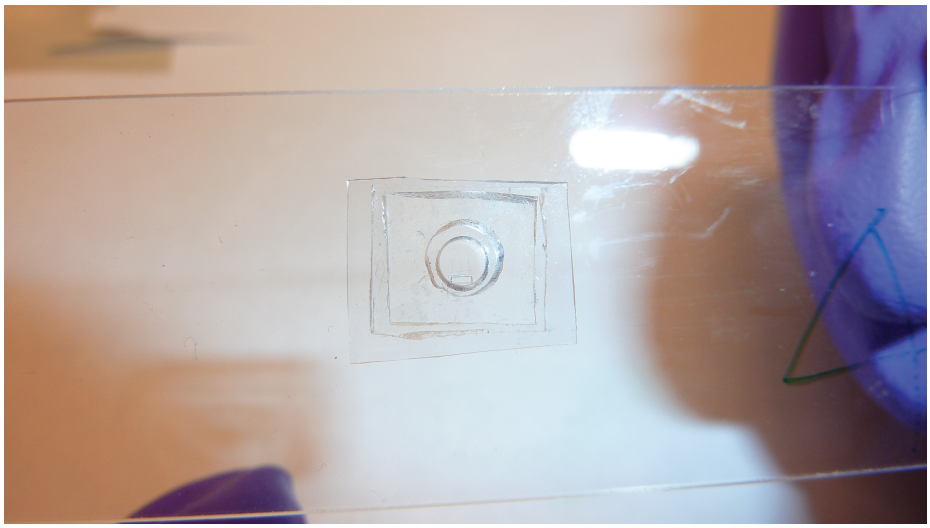

Figure B.11: Final assembly of the mixing chamber, ready for mixing experiments

Appendix C

CONTROL DESIGN AND IMPLEMENTATION

C.1 Determining the Controller Gain, K

The open-loop model of the piezoactuator (G_p in Figure A.2) is obtained experimentally. In particular, experimental frequency responses are obtained by using a dynamic signal analyzer (SRS Model SR785) at different input voltage V_a amplitudes as shown in Figure A.3. A fit of the experimental response is obtained using Matlab and the resulting model G_p is described by the following transfer function

$$G_p(s) = \frac{u_c(s)}{V_a(s)} = k\prod_i^N \frac{(s - z_i)}{(s - p_i)} \tag{C.1}$$

where the poles p_i, zeros z_i and gain k are listed in Table C.1.

Poles, p_i	$(-23.95 \pm 235.56i)2\pi$
	$(-7.78 \pm 316.89i)2\pi$
	$(-13.25 \pm 414.64i)2\pi$
Zeros, z_i	$(-4.41 \pm 293.87i)2\pi$
	$(-3.01 \pm 376.16i)2\pi$
Gain, k	1206400

Table C.1: Parameters of piezoactuator model G_p in Eq. (C.1) : Open-loop model

The open-loop model of the piezoactuator (G_p) is used to plot the root locus using the Matlab commands.

After the iterative process in design, it is concluded that the proportional control is appropriate for this particular control system in terms of performance and simplicity and it is chosen for the implementation.

The root locus is shown in Figure C.1 with the selected gain of 5, which satisfies the performance and stability, and the resulting closed-loop pole locations marked by the plus signs (+) on the root locus are listed in Table C.2.

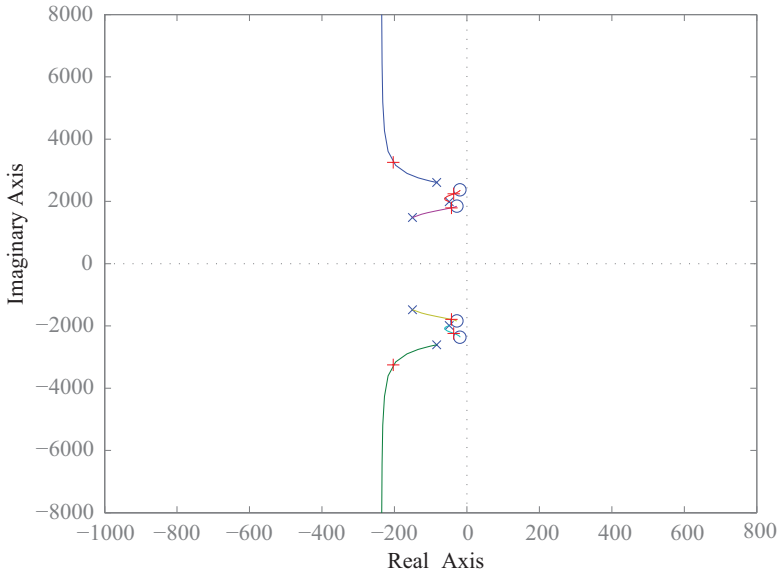

Figure C.1: Root locus

Poles, p_i	$(-6.82 \pm 285.02i)2\pi$
	$(-5.81 \pm 356.61i)2\pi$
	$(-32.35 \pm 517.82i)2\pi$

Table C.2: Closed-loop pole locations

Note that the root locus shown in Figure C.1 is generated by the following Matlab code.

```
% this file plots the root locus
clear all; close all; clc;

load datamodel % load the model obtained in Appendix A
```

```
sysmodel = syst_current;

rlocus(sysmodel)% plot the root locus to show the closed-loop pole
% trajectories as a function of the gain,K

[K,r]=rlocfind(sysmodel)% put up a crosshair cursor in the graphics window
% which is used to interactively select gain,K and obtain the
% closed-loop poles associated with the selected gain,K
% the selected point, the gain k, and the closed-loop poles will appear
% in the command window
```

C.2 Hardware and Software for Implementing the Control

[1] A circuit diagram that contains the amplifier, the piezoactuator, the op-amps, the potentiometer for biasing, and the resistors for scaling, is designed as shown in Figure C.2.

[2] The circuit as designed is built on a breadboard and connected to NI myDAQ as shown in Figure C.3.

[3] Labview graphical-based programming language is used for the DAQ interface. The front panel is shown in Figure C.4 and the block diagram is shown in Figure C.5.

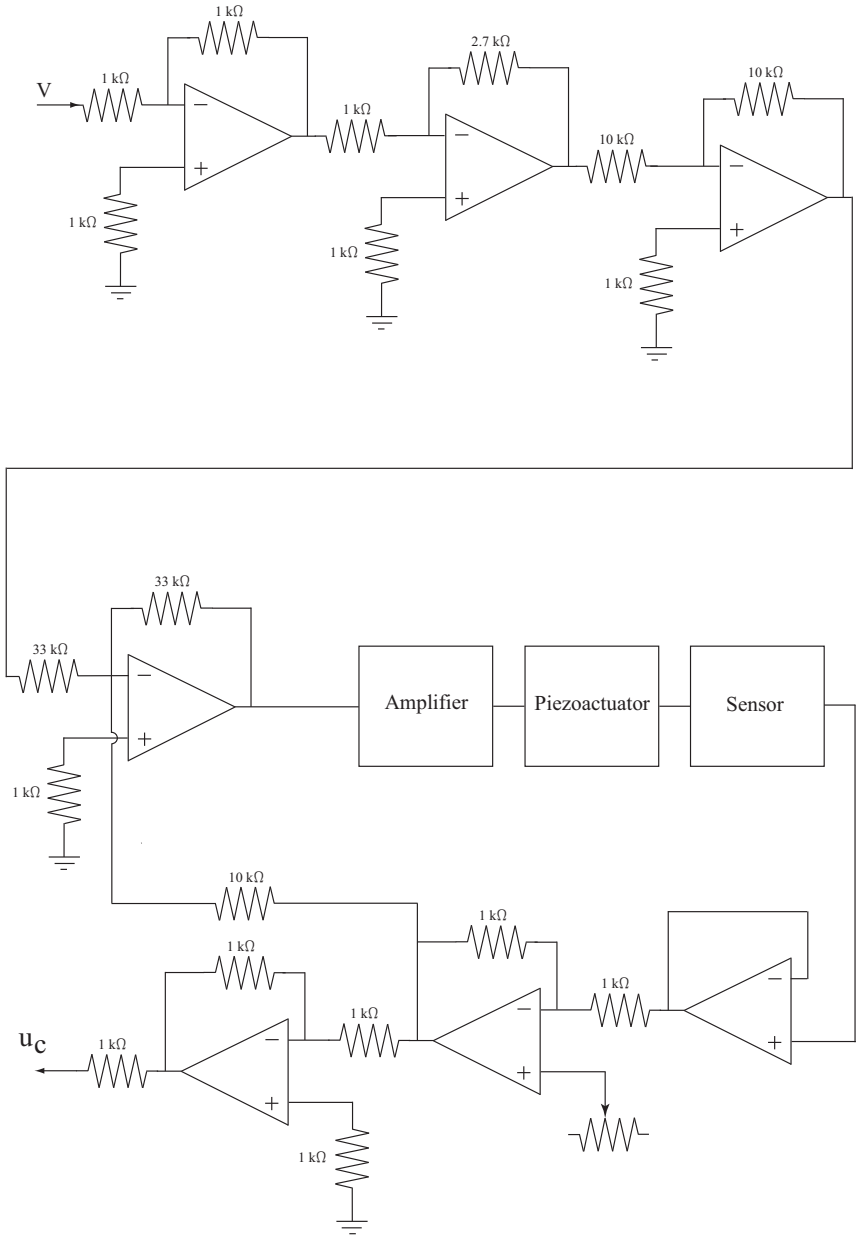

Figure C.2: Circuit diagram

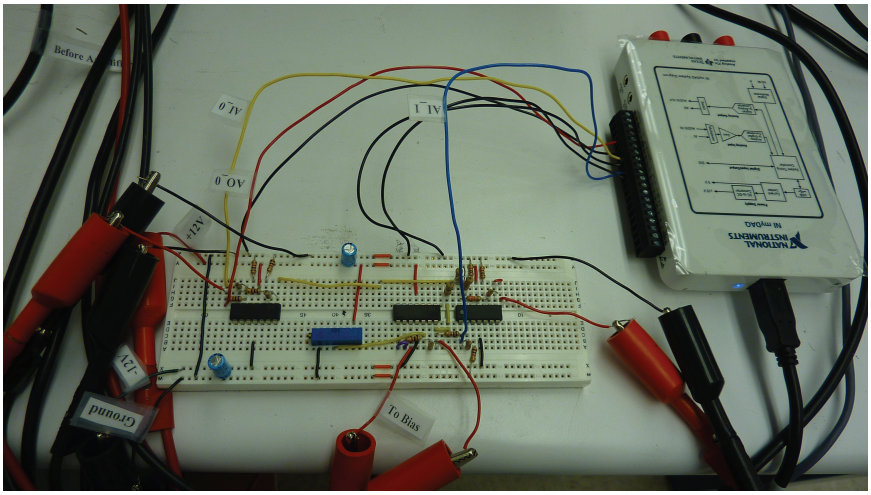

Figure C.3: Op-amp circuit built on the breadboard connected to NI myDAQ : Power supply lines, ground lines, blue capacitors between them, and DAQ wires on the circuit board are not shown in Figure C.2.

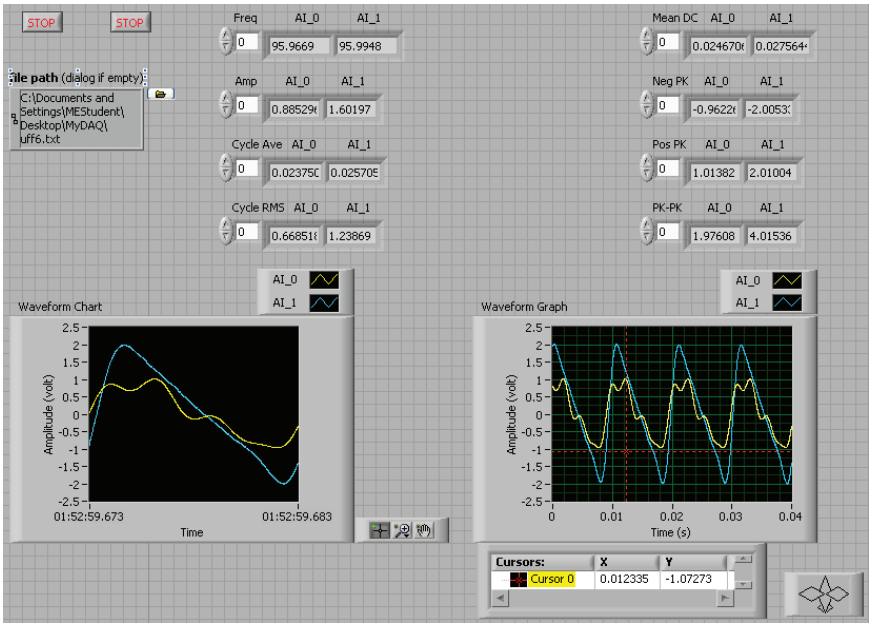

Figure C.4: Labview front panel for DAQ system while running the mixing experiment

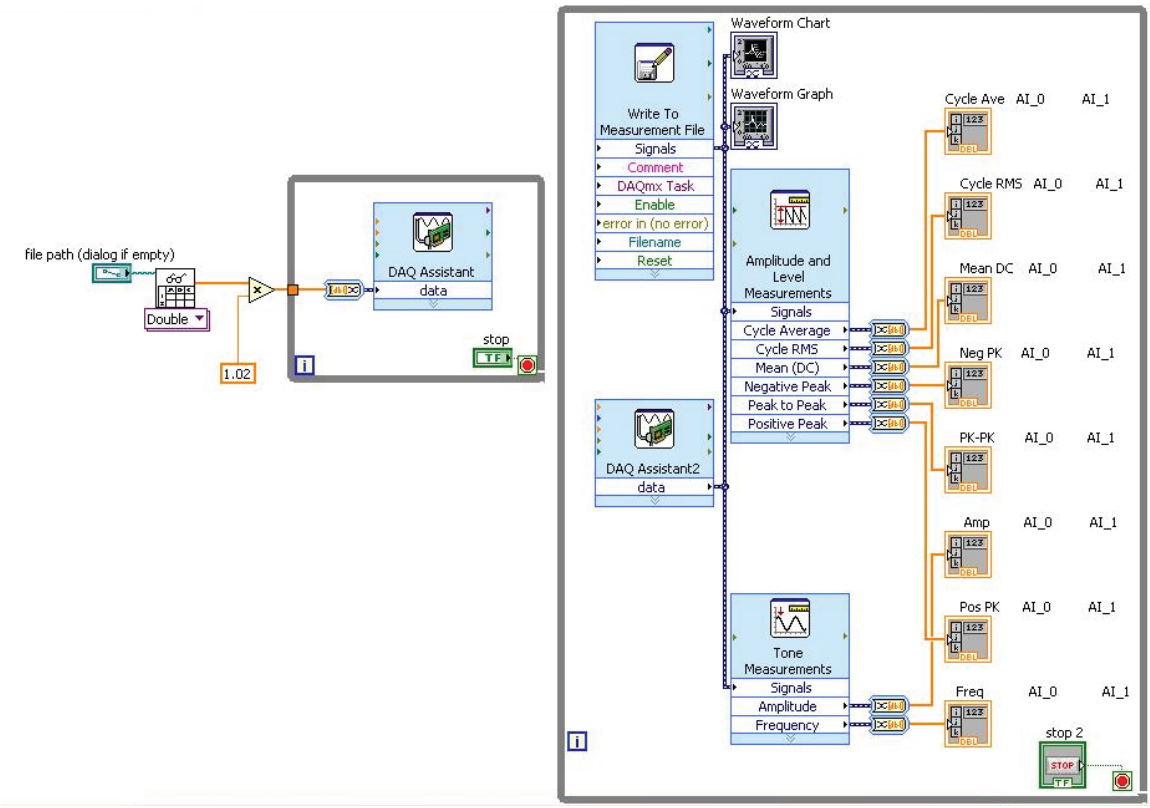

Figure C.5: Labview block diagram for DAQ system

C.3 Iterative Control Approach to Finding the Inverse Inputs

[1] The following Matlab code is used to determine the iteration gain, ρ.

```
% this file generates the plot to determine the iteration gain,rho

clear all; close all;clc;
figure_no = 0; % figure number

Kac=1;% signal gain before entering DSA
Ks=1;% sensor gain
Kas=1/(Kac);

%load the experimental freq response data
load JK241; % 1v ideal ref set on DSA.
load JK245; % 100 mv set on DSA

f_Hz_jk241   = jk241(:,1); % frequency in Hz
f_rad_jk241  = 2*pi*f_Hz_jk241; % frequency in radian
G_jk241     = jk241(:,2); % these are complex numbers

f_Hz_jk245   = jk245(:,1); % frequency in Hz
f_rad_jk245  = 2*pi*f_Hz_jk245; % frequency in radian
G_jk245     = jk245(:,2);  % these are complex numbers

% extract the magnitude and phase information
m_jk241=(abs(G_jk241))/Kas;% the magnitude of G
m_db_jk241=20*log10(abs(G_jk241)/Kas); % magnitude in db
```

```
p_jk241=(angle(G_jk241))*180/pi;

% extract the magnitude and phase information
m_jk245=(abs(G_jk245))/Kas;% the magnitude of G
m_db_jk245=20*log10(abs(G_jk245)/Kas); % magnitude in db
p_jk245=(angle(G_jk245))*180/pi;

figure_no = figure_no +1; figure(figure_no)
subplot(2,1,1);
semilogx(f_Hz_jk241,m_db_jk241,'b',f_Hz_jk245,m_db_jk245,'m');
title('Closed-Loop Response,1.0v Ideal Ref DSA output,100mv DSA input');
xlabel('Frequency (Hz)');
ylabel('Magnitude (db)');
subplot(2,1,2);
semilogx(f_Hz_jk241,p_jk241,'b',f_Hz_jk245,p_jk245,'m');
xlabel('Frequency (Hz)');
ylabel('Phase (degree)');
legend('1.0v Ideal Ref DSA output','100mv DSA input',3);

% magnitude ratio and phase difference between two different sizes
% of inputs
del_phase=(unwrap((p_jk245-p_jk241))); % in degreee
del_mag=m_jk245./m_jk241;
two_cos_del_phase=2*cos(del_phase*pi/180);
ratio=two_cos_del_phase./del_mag;

figure_no = figure_no +1; figure(figure_no)
subplot(2,1,1);
```

```
semilogx(f_Hz_jk241,del_mag,'m');
title('Magnitude Ratio');
xlabel('Frequency (Hz)');
ylabel('Magnitude Ratio (abs)');
subplot(2,1,2);
semilogx(f_Hz_jk241,del_phase,'m');
title('Phase Difference');
xlabel('Frequency (Hz)');
ylabel('Phase Difference (degree)');

figure_no = figure_no +1; figure(figure_no)
plot(f_Hz_jk241,ratio,'b');
title('2cos del phase/del mag');
xlabel('Frequency (Hz)');
ylabel('2cos del phase/del mag');
axis([100 500 0 23])

Ratio_Min=min(ratio)
Lower_bound=Ratio_Min*ones(size(ratio)); % draw the line for lower bound

figure_no = figure_no +1; figure(figure_no)
plot(f_Hz_jk241,ratio,'b',f_Hz_jk241,Lower_bound,'r');
title('2cos del phase/del mag');
xlabel('Frequency (Hz)');
ylabel('2cos del phase/del mag');
```

[2] The following Matlab function is used to compute the optimal inverse solutions.

```
% this function is available in the lab
function [uopt,yopt] = optinv_s_exp(w_g,g,r,q,omega,y,t)
%
%  optimal inversion function
% Usage: [uopt,yopt] = optinv_expdat(w_g,g,r,q,omega,y,t)
%
% Notes
% g denotes the stable transfer function evaluated at w_g which starts at
%   zero frequency input and optimal inverse are set to zero at frequencies
%   w such that  max(w_g) < w <  max(omega)
%
% system must be non-hyperbolic, i.e., no zeros on the imaginary axis
% r and q are defined as a function of omega, i.e. specify frequencies
% values in omega and the values of r and q for those frequencies
% If r and q are not specified for a frequency then r =1 and q=0;
% t row vector, must be evenly spaced time points (and has an odd length)
% it is advisable that y be zero at beginning and end.
% y must be same size as time vector "t"
% the output u is the optimal inverse-input into the system
% yopt is the modified output


%Related Papers
%[1]  Q. Zou and S. Devasia "Preview-based Stable-Inversion for Output
%       Tracking," ASME J. of Dynamic Systems, Measurement and Control,
```

```
%     Vol. 121 (4), pp. 625-630, December 1999.
%[2] S. Devasia "Approximated Stable Inversion for Nonlinear Systems
%     with Nonhyperbolic Internal Dynamics," IEEE Trans. on Automatic
%     Control,Vol. 44 (7), pp. 1419-1425, July 99.
%[3] J.S. Dewey, K. K. Leang and S. Devasia "Experimental and
%       Theoretical Results in Output-Trajectory Redesign for Flexible
%    Structures," ASME Journal of Dynamic Systems, Measurement,
%       and Control, Vol. 120 (4), pp. 456-461, Dec. 1998.
%[4]   S. Devasia and B. Paden "Stable Inversion for Nonlinear
%     Nonminimum-Phase Time-Varying Systems," IEEE Trans. on Automatic
%       Control, Vol. 43 (2), pp. 283-288, Feb. 1998.
%[5] S. Devasia, B. Paden and C. Rossi "Exact-Output Tracking Theory
%     for Systems with Parameter Jumps," International Journal of Control
%       , Vol. 67 (1), pp. 117-131, May 1997.
%[6] S. Devasia, D. Chen and B. Paden "Nonlinear Inversion-Based Output
%     Tracking," IEEE Transactions on Automatic Control, Vol. 41 (7),
%       pp. 930-942, July 1996.
%[7]  D. Croft and S. Devasia "Vibration Compensation for High Speed
%     Scanning Tunneling Microscopy," Review of Scientific Instruments
%     published by the American Institute of Physics, Vol. 70 (12),
%       pp. 4600-4605, December 1999.

delt  = t(2)-t(1);
Nt      = length(t);
Nf      = (Nt-1)/2;
del_freq    = ((2*pi/delt)/2)/Nf;
i  = sqrt(-1);
u  = zeros(size(t));
```

```
yopt  = zeros(size(t));
yf      = fft(y);
ome_max  = max(omega);
%ym = abs(yf); yp=(180/pi)*unwrap(angle((yf)));
%ww=(1:1:Nt)*(2*pi/delt);plot(ww,abs(ym))

for jj=1:1:Nf,
   ome = del_freq*jj;
   if ome < ome_max
      rr = interp1(omega,r,ome);
      qq = interp1(omega,q,ome);
   else
      rr = 1;
      qq = 0;
   end
   if ome < max(w_g)
      gw = interp1(w_g, g, ome);
      yopt(jj+1) = ( (gw*(conj(gw))*qq)/( gw*(conj(gw))*qq + rr))*yf(jj+1);
      u(jj+1)   = yopt(jj+1)/gw;
   else
      yopt(jj+1)  = 0;
      u(jj+1)     = 0;
   end
   jjj  = Nt+1-jj;
   yopt(jjj)  = conj(yopt(jj+1));
   u(jjj)  = conj(u(jj+1));

end
```

```
% the DC gain effects
rr  = interp1(omega,r,0);
qq  = interp1(omega,q,0);
gw       = interp1(w_g,g,0);
yopt(1)  = ( (gw*(conj(gw))*qq)/( gw*(conj(gw))*qq + rr) )*yf(1);
u(1)  = yopt(1)/gw;

yopt = real(ifft(yopt));
uopt = real(ifft(u));

return
```

[3] The following Matlab code is used to find the initial inverse input.

```
% this file finds the initial inverse input
clear all; close all;clc;

% constants and parameters
figure_no=0; % figure number
TimeScale=10^(-3); % time scaled to millisecond
sec2msec=1000; % conversion factor from second to millisecond
freq = 96*TimeScale; % frequency in cycle per millisecond
AoverB =.25; % A/B time asymmetry index
one_period=1/freq;% millisecond
DCfactor=1;% dc gain based on function generator
```

```
N=2000;%2000 % number of points
SamplingFreq192K=192000;
del=(1/freq)/N; % time step
save variables TimeScale sec2msec one_period freq SamplingFreq192K...
    AoverB N del

% experimental data and frequency response
load JK241; % load the experimental frequency response data,100 to 500 Hz
f_Hz_clk   = [0;jk241(:,1)] ; % frequency in Hz
f_rad_clk = 2*pi*f_Hz_clk;  % frequency in radian
G_clk    = ([abs(jk241(1,2));jk241(:,2)]);  % these are complex numbers
m_clk=(abs(G_clk));% the magnitude of G
m_db_clk=20*log10(abs(G_clk));  % magnitude in db
p_clk=unwrap(angle(G_clk))*180/pi;

figure_no = figure_no +1; figure(figure_no)
subplot(2,1,1);
semilogx(f_Hz_clk,m_db_clk,'k');
title('Experimental Closed-Loop Response');
xlabel('Frequency (Hz)');
ylabel('Magnitude (db)');
subplot(2,1,2);
semilogx(f_Hz_clk,p_clk,'k');
xlabel('Frequency (Hz)');
ylabel('Phase (degree)');

figure_no = figure_no +1; figure(figure_no)
subplot(2,1,1);
```

```
plot(f_Hz_clk,m_db_clk,'k');
title('Experimental Closed-Loop Response');
xlabel('Frequency (Hz)');
ylabel('Magnitude (db)');
subplot(2,1,2);
plot(f_Hz_clk,p_clk,'k');
xlabel('Frequency (Hz)');
ylabel('Phase (degree)');

w_g=f_rad_clk*TimeScale;% input for optimum inverse
g=G_clk ;% input for optimum inverse

% tracking scheme
% quantify the frequency weights (r and q) on input and tracking error
scale_q = 1; % increase this increases the tracking precision
scale_r = 1; % increase this term to reduce the magnitude of inputs
% choose q and r
omega =  [0 200 400 500 100500*1000]*2*pi*TimeScale;
q =      [1 1    1   0  0]*scale_q;
r =      [0 0    0   1  1]*scale_r;
omegap = [0 200 400 500 600 ];

% plot Q and R
figure_no = figure_no +1; figure(figure_no)
plot(omegap,q,'-r',omegap,r,':k')
axis([0 500 -0.2 1.2])
xlabel('Hz')
legend('Q','R')
```

```
% trajectory definitions
downlen = 1/(2*freq*(AoverB+1)); % time in millisecond=A;
uplen = AoverB/(2*freq*(AoverB+1)); % time in millisecond=B;
Height=4; % peak-to-peak-amplitude in volt (4 volts = 20 microns)
Amplitude=Height/2;
ymax = Height/2;
rampup = ymax/(uplen);% uphill slope
rampdown = ymax/(downlen);% downhill slope
% define the desired trajectory in section
% tA= 0:delt:uplen-delt;
tA= 0:del:uplen;
Y1=rampup*tA;
tB=max(tA)+del:del:max(tA)+downlen;
Y2 = max(Y1)-rampdown*(tB-max(tA));
Y3 = min(Y2)-rampdown*(tB-max(tA));
Y4 = -min(Y3)+rampup*(tA-max(2*tA)+del);
%Y=[Y1(1:end-1) Y2];
Y=[Y1 Y2 Y3 Y4];
Y=Y(1:end-1);

figure_no =figure_no+1; figure(figure_no);  clf;
plot(Y)
xlabel('Number of Points')
ylabel('Displacement(\mum)')
title ('Wave Trajectory')
grid
%return
```

```
Ynew=Y(1:(length(Y)-1)); % one of the superimposed points to be removed
tnew=del*(0:1:length(Ynew)-1);

figure_no =figure_no+1; figure(figure_no);  clf;
plot(tnew,Ynew,'r','LineWidth',2')
xlabel('Time(millisecond)')
ylabel('Displacement(\mum)')
title ('Wave Trajectory')
grid
% return

Y3p=[Ynew Ynew Ynew]; % 3 periods
t3p=del*(0:1:(length(Y3p)-1));

% return
Y=Ynew; % one cycle
Y=[Y Y Y Y Y Y Y Y Y Y Y Y Y Y Y]; % 15 cycles
Y=[Y Y Y]; % 45 cycles
t=del*(0:1:(length(Y)-1));
% return

figure_no =figure_no+1; figure(figure_no);  clf;
plot(t,Y,'r','LineWidth',2')
axis([min(t) max(t) (min(Y)-0.1*max(Y)) (max(Y)+0.1*max(Y))])
xlabel('Time(millisecond)')
ylabel('Displacement(\mum)')
title ('Wave Trajectory')
```

```
grid
% return

% trajectory input to optimum inverse function and execution
y_tail=[0*Y 0*Y 0*Y];
y_middle=[0*Y 0*Y 0*Y];
y=  [y_tail Y y_middle -Y y_tail];
t = del*[0:1:(length(y)-1)];

figure_no =figure_no+1; figure(figure_no);  clf;
plot(t,y)
xlabel('Time(millisecond)')
ylabel('Displacement(\mum)')
title ('Trajectory  Fed into Optimum Inverse Function')
% return

% find the optimal inverse
[uoptinv,yoptinv]=optinv_s_exp(w_g,g,r,q,omega,y,t);
save initialSolution uoptinv yoptinv
save inputVector w_g g r q omega
% return

load initialSolution
load inputVector

figure_no =figure_no+1; figure(figure_no);  clf;
subplot(311), plot(t,uoptinv,'r'); ylabel('input (volt)')
subplot(312), plot(t,y,'g',t,yoptinv,'b'); ylabel('output (\mum)')
```

```
legend('y','yopt')
subplot(313), plot(t,yoptinv-y,'g'); ylabel('yopt-y(\mum)')

figure_no =figure_no+1; figure(figure_no);  clf;
plot(t,uoptinv,'r');
xlabel('Time(millisecond)')
ylabel('input (volt)')
title ('uopt0')
% return

% plot the optimal solution, desired trajectories, and error
figure_no =figure_no+1; figure(figure_no);  clf;
subplot(311), plot(t,uoptinv,'r'); ylabel('input (volt)')
subplot(312), plot(t,y,'g',t,yoptinv,'b'); ylabel('output (\mum)')
legend('y','yopt')
subplot(313), plot(t,yoptinv-y,'g'); ylabel('yopt-y(\mum)')

Npoints=one_period/del;% numbers of points taken in one period
t_steady_state=1680;% time in millisecoond visaully determined to wait
% till steady state

cycles2wait=fix(t_steady_state/one_period);
Nk=cycles2wait*Npoints;% index

yd=[y(Nk+1:Nk+(Npoints-1)+1)];
yopt=[yoptinv(Nk+1:Nk+(Npoints-1)+1)];
uopt=[uoptinv(Nk+1:Nk+(Npoints-1)+1)];
time=del*(0:1:length(yd)-1);
```

```
figure_no =figure_no+1; figure(figure_no);  clf;
plot(time,yd,'m',time,uopt,'b')

xlabel('millisecond')
ylabel('y_{d} (\mum),uopt(volt)')
title('y_{d} (\mum),uopt0(volt)')
legend('yd','uopt0')

% find time where the minimum uopt occurs
[C Iumin]=min(uopt);
t_umin=Iumin*del
% return

uopt_2p=[uopt uopt]; % 2 cycles
yd_2p=[yd yd]; % 2 cycles
yopt_2p=[yopt yopt]; % 2 cycles

time_2p=del*(0:1:length(uopt_2p)-1);
figure_no =figure_no+1; figure(figure_no);  clf;
plot(time_2p,uopt_2p,'b')
xlabel('millisecond')
ylabel('uopt(volt)')
title('uopt0(volt), 2 periods')

figure_no =figure_no+1; figure(figure_no);  clf;
plot(time_2p,yd_2p,'b')
xlabel('millisecond')
```

```
ylabel('yd(\mum)')
title('yd, 2 periods')

figure_no =figure_no+1; figure(figure_no);  clf;
plot(time_2p,yopt_2p,'b')
xlabel('millisecond')
ylabel('yopt(\mum)')
title('yopt, 2 periods')

% find time at zero crossing or sign change
Iuzero=find(uopt_2p(1:end-1).*uopt_2p(2:end)<=0)
time_uzero_xing=del*Iuzero(1)
uopt_zero=[uopt_2p(Iuzero:Iuzero+(Npoints-1))];

figure_no =figure_no+1; figure(figure_no);  clf;
plot(time,uopt_zero,'m')
xlabel('millisecond')
ylabel('uopt(volt)')
title('uopt(volt) sent to DAQ')

uopt_min=[uopt_2p(Iumin:Iumin+(Npoints-1))];
yd_min=[yd_2p(Iumin:Iumin+(Npoints-1))];

figure_no =figure_no+1; figure(figure_no);  clf;
plot(time,uopt_min,'b',time,yd_min,'r')
xlabel('millisecond')
ylabel('uopt(volt)')
title('uopt min and yd from MATLAB optimal solution ')
```

```
legend('umin','ymin')

% Sample the data and save it in a text file

% set the sampling frequency of 192KHz to change to D/A
FD2A = SamplingFreq192K*TimeScale;% sampling rate in cycle/millisecond
% for 96 Hz and 2000 points in 1 period
N_points = (FD2A/freq)% number of points to be an integer

time_old=time;
time_new=(0 :1:(N_points-1))*(1/FD2A); % last point to be removed

uopt_sp=interp1(time_old,uopt_zero,time_new','linear','extrap');
uopt0_sp2daq=uopt_sp;

figure_no =figure_no+1; figure(figure_no);  clf;
plot(time_new,uopt0_sp2daq,'r')
xlabel('millisec')
ylabel('u_{opt0} (volt)')
title('u_{opt0} scaled and sent to DAQ')
% return

% save into a text file
fid = fopen('uff0.txt','w');
fprintf(fid, '%2.4f\t', uopt0_sp2daq);% define the format
fclose('all'); % close the file

% check the number of points, maximum values, and minimum values
```

```
Number_of_Points_inv=length(uopt0_sp2daq)
Max_uopt0_sp2daq=max(uopt0_sp2daq)
Min_uopt0_sp2daq=min(uopt0_sp2daq)

save initialData % save everything
save nextIterationData yd uopt time Iumin Npoints del % save these
% for next iterations
```

[4] The following Matlab code is used to find the next inverse inputs based on the iterative control law till the divergence occurs.

```
% this file finds the first inverse input from the iterative control law
% this file is used for the next iterations untill the divergence occurs
clear all; close all;clc;
figure_no=0; % initialize figure number
% load data
load variables
load inputVector
load nextIterationData

% read experimental data from 2 analog input channels saved in Excel file
% visaully determine numbers of cycles to wait till steady state
% read data from the Excel file
uopt_ai=xlsread('uff0.xls',1,'B43152:B44193');
time_ai=xlsread('uff0.xls',1,'A43152:A44193');
```

```
yact_ai=xlsread('uff0.xls',1,'D43152:D44193');
time_ai_yact=xlsread('uff0.xls',1,'C43152:C44193');

% time_ai_yact=time_ai
figure_no = figure_no +1; figure(figure_no);
time_ai=(time_ai-min(time_ai))*sec2msec;

plot(time_ai,uopt_ai','m',time_ai,yact_ai,'g')
xlabel('Time(millisecond)')
ylabel('uopt0 (volt)  yact0(\mum)')
title ('uopt0 (volt)  yact0(\mum)')
legend('uopt0 (volt)','yact0 (\mum)')
%return

% time_new=time;
% interpolate to get 2000 points in 1 period (1000 points from the
% experiment)
yact_new=interp1(time_ai,yact_ai,time','linear','extrap');
uopt_ai_new=interp1(time_ai,uopt_ai,time','linear','extrap');

figure_no =figure_no+1; figure(figure_no);  clf;
plot(time,uopt_ai_new','r')
xlabel('millisec')
ylabel('uopt volt new (volt)')
title('uopt ai scaled and interpolated')
yact_new=yact_new';
yact_new_2p=[yact_new yact_new];
```

```
% yact shifted here
% shift yact_new to yd time
yact=[yact_new_2p((Npoints-Iumin)+2:(Npoints-Iumin)+2+(Npoints-1))];
% yact with time shift
% return

figure_no =figure_no+1; figure(figure_no);  clf;
plot(time,yact,'r')
xlabel('millisec')
ylabel('yact (volt)')
title('yact shifted to yd')
% return
e=yd-yact;% compute the error

figure_no =figure_no+1; figure(figure_no);  clf;

subplot(2,1,1)
plot(time_ai,uopt_ai','m',time_ai,yact_ai,'b')
xlabel('Time(millisecond)')
ylabel('uopt (volt)  yact(\mum)')
title ('uopt (volt)  yact(\mum) from Experiment AI')
legend('uopt (volt)','yact (\mum)')
subplot(2,1,2)
plot(time,e,'r')
xlabel('millisec')
ylabel('Error (\mum)')
title('Error,y_{d}-y_{act} ')
%return
```

```
% find time at zero crossing or sign change
Izero_xing_e=find(e(1:end-1).*e(2:end)<=0)
time_zero_xing_e=del*Izero_xing_e(1)
%return

% check it graphically to make sure
zero_line=0*ones(length(e));
figure_no = figure_no +1; figure(figure_no);
plot(time,e,'r',time,zero_line,'b')
xlabel('millisecond')
ylabel('Error (\mum)')
title('Error ,y_{d}-y_{act} ')
% return

error_2p=[e e];
error=[error_2p(Izero_xing_e:Izero_xing_e+(Npoints-1))];% take 1 period
% plot the error
figure_no =figure_no+1; figure(figure_no);  clf;
plot(time,error,'r')
xlabel('millisec')
ylabel('Error (\mum)')
title('Error, zero-zero,y_{d}-y_{act} ')
% return

% compute the root mean squared error
RMSE = sqrt(sum(error.*conj(error))/size(error,1))
% return
```

```
% iterative process
% define the errors
errors=[error error error error error error error error];% 8 periods
errors=[errors errors errors errors errors];% 8*5=40 periods
errors=[errors errors errors];% 120 periods
te=del*(0:1:(length(errors)-1));

% plot the error
figure_no =figure_no+1; figure(figure_no);  clf;
plot(te,errors,'k')
xlabel('Time(millisecond)')
ylabel('Error,yd-yact(\mum)')
title ('Error New,yd-yact(\mum)')
% return

% define the tail portion
errors_tail=[0*errors 0*errors];
errors_middle=[0*errors 0*errors];

err=  [errors_tail errors errors_middle -errors errors_tail];% input to
% the optimal inverse
t = del*[0:1:(length(err)-1)];

% plot the error
figure_no =figure_no+1; figure(figure_no);  clf;
plot(t,err)
xlabel('Time(millisecond)')
```

```
ylabel('Error,yact-yd(\mum)')
title ('Error,yact-yd(\mum)')
% return

% compute the optimal inverse
[uopt_extra,yopt_extra]=optinv_s_exp(w_g,g,r,q,omega,err,t);

% save all necessary data
save  uopt_extra_sol t uopt_extra yopt_extra err Izero_xing_e
% return

load  uopt_extra_sol

% plot the optimal solution
figure_no=0;
figure_no =figure_no+1; figure(figure_no);  clf;
plot(t,uopt_extra)
xlabel('Time(millisecond)')
ylabel('uopt_{extra} (volt)')
title ('uopt_{extra} (volt)')

Npoints=one_period/del;% numbers of points taken in one period
t_steady_state=3210;% time in millisecoond visaully determined to wait
% till steady state
cycles2wait=fix(t_steady_state/one_period);
Nk=cycles2wait*Npoints;% index
uopt_extra=[uopt_extra(Nk+1:Nk+(Npoints-1)+1)];
```

```
figure_no =figure_no+1; figure(figure_no);  clf;
plot(time,uopt_extra,'m')
xlabel('millisecond')
ylabel('uopt extra(volt)')
title('uopt extra(volt)')

%uopt_extra shifted here
uopt_extra_2p=[uopt_extra uopt_extra]; % create 2 periods
uopt_extra_ts=[uopt_extra_2p((Npoints-Izero_xing_e)+...
    2:(Npoints-Izero_xing_e)+2+(Npoints-1))]; % shift back to
% the zero yd time and create 1 period
time_2p=del*(0:1:length(uopt_extra_2p)-1);

figure_no =figure_no+1; figure(figure_no);  clf;
plot(time_2p,uopt_extra_2p,'m')
xlabel('millisecond')
ylabel('uopt extra(volt)')
title('uopt extra(volt)')
%return

figure_no =figure_no+1; figure(figure_no);  clf;
plot(time,uopt_extra_ts,'m')
xlabel('millisecond')
ylabel('uopt extra(volt)')
title('uopt extra(volt) shifted')

uopt_old=uopt;
```

```
% iterative control law
rho=0.3; % iteration gain
uopt=uopt+rho*uopt_extra_ts;

% plot uopt0 and uff compared
figure_no =figure_no+1; figure(figure_no);  clf;
plot(time,uopt_old,':r',time,uopt,'k')
xlabel('millisec')
ylabel('uff0 and uff1 (Volt)')
title('uff0 and uff1')
legend('uff0','uff1')
% return

figure_no =figure_no+1; figure(figure_no);  clf;
plot(time,uopt,'b')
xlabel('millisecond')
ylabel('uopt(volt)')
title('uopt(volt)')

% find time where the minimum uopt occurs
[C Iumin]=min(uopt);
t_umin=Iumin*del
% return

% find time at zero crossing or sign change
I_zero_xing_uopt=find(uopt(1:end-1).*uopt(2:end)<=0)
time_zero_xing_uopt=del*I_zero_xing_uopt(1)
```

```
uopt_2p=[uopt uopt]; % 2 cycles

figure_no =figure_no+1; figure(figure_no);  clf;
plot(time_2p,uopt_2p,'b')
xlabel('millisecond')
ylabel('uopt(volt)')
title('uff1(volt), 2 periods')

% find time at zero crossing or sign change
Iuopt_zero=find(uopt_2p(1:end-1).*uopt_2p(2:end)<=0)
time_uzero_xing=del*Iuopt_zero(1)

uopt_zero=[uopt_2p(Iuopt_zero:Iuopt_zero+(Npoints-1))];

figure_no =figure_no+1; figure(figure_no);  clf;
plot(time,uopt_zero,'m')
xlabel('millisecond')
ylabel('uff1(volt)')
title('uff1(volt)')

figure_no =figure_no+1; figure(figure_no);  clf;
plot(time,uopt_zero,'r')
xlabel('millisec')
ylabel('uopt uff1(volt)')
title('uopt uff1')
% return

% save into a text file
```

```
% put uff in an array and save it in a text file
fid = fopen('uff1.txt','w');
fprintf(fid, '%2.4f\t',uopt_zero);
fclose('all');

% check the number of points, maximum values, and minimum values
Number_of_Points_uff=length(uopt_zero)
Max_uff=max(uopt_zero)
Min_uff=min(uopt_zero)

save iteration_1_Data % save everything
save nextIterationData yd uopt time Iumin Npoints del % save these
% for next iterations
```

Appendix D

SAMPLE IMAGES FROM MIXING EXPERIMENTS, IMAGE ANALYSIS, AND PLOTTING THE MIXING INDEX

D.1 Sample Images Captured from Mixing Experiments in Chapter 4

The following sample images of the mixing process are captured at different mixing indices ,$I_{mix} = 0,\ 0.6,\ 0.8,\ 0.9,\ 0.95$ and 1, for 7 runs of each case.

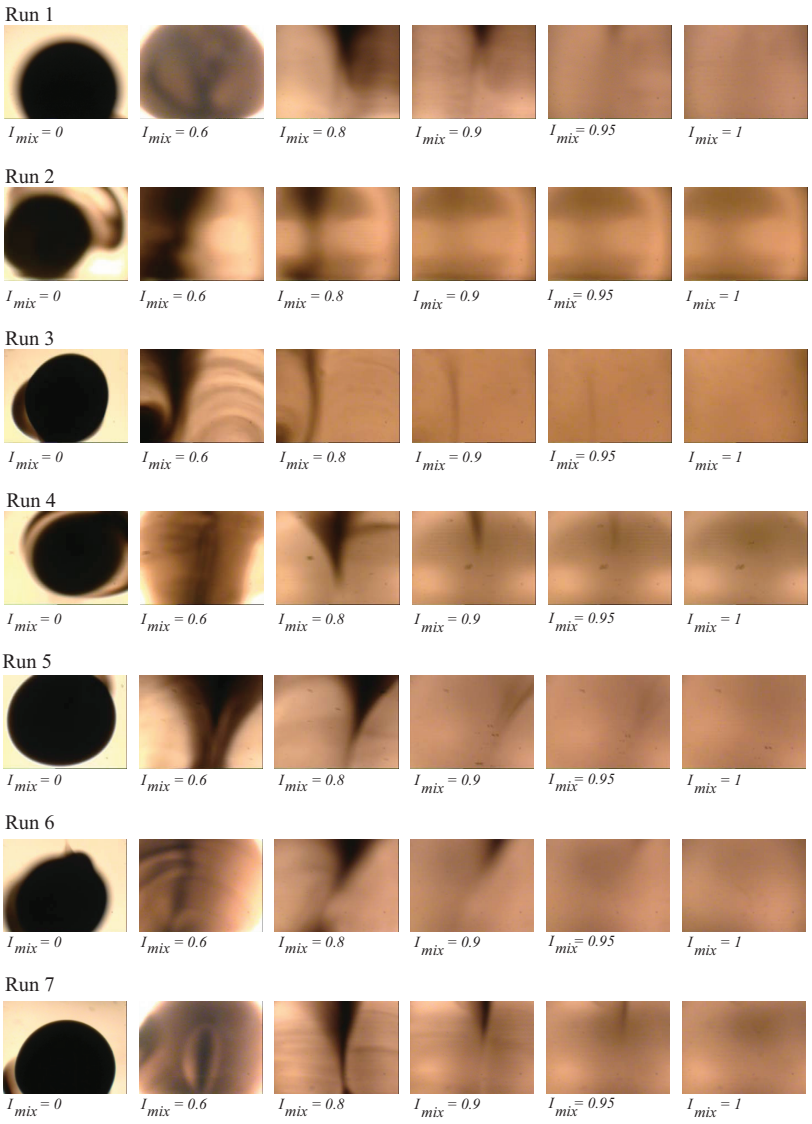

Figure D.1: Sample images captured at different mixing indices for sinusoidal excitation without cilia

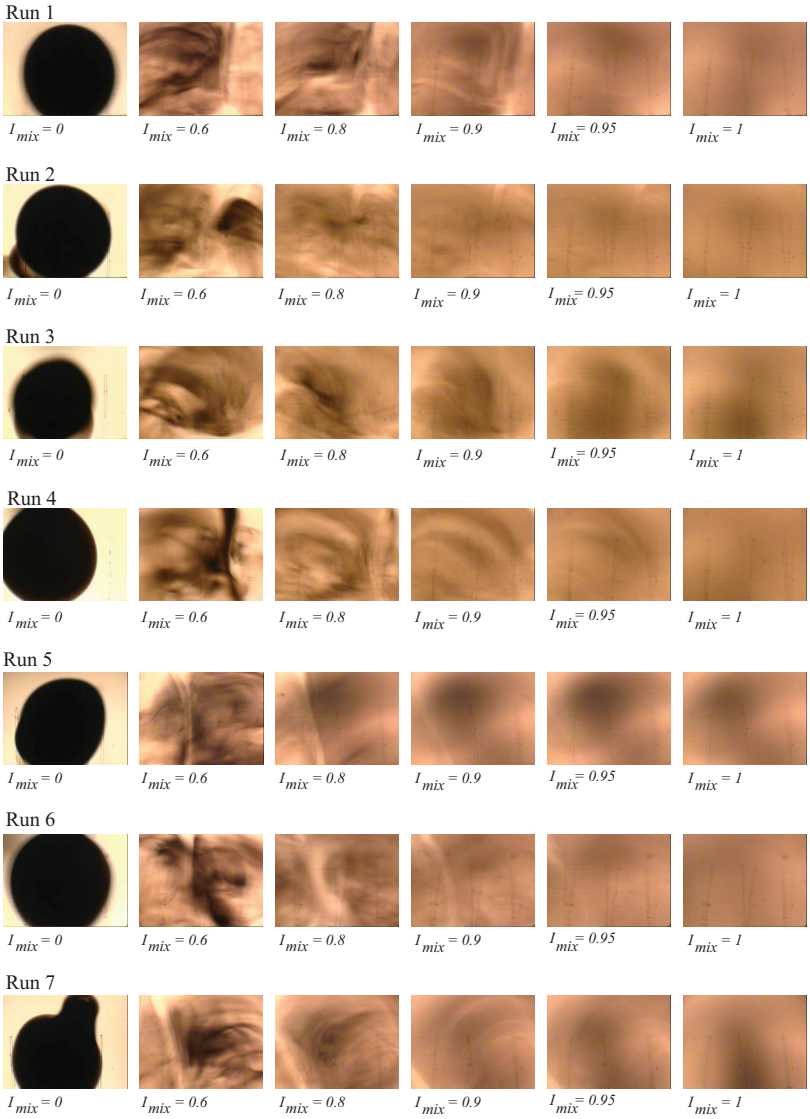

Figure D.2: Sample images captured at different mixing indices for sinusoidal excitation with cilia

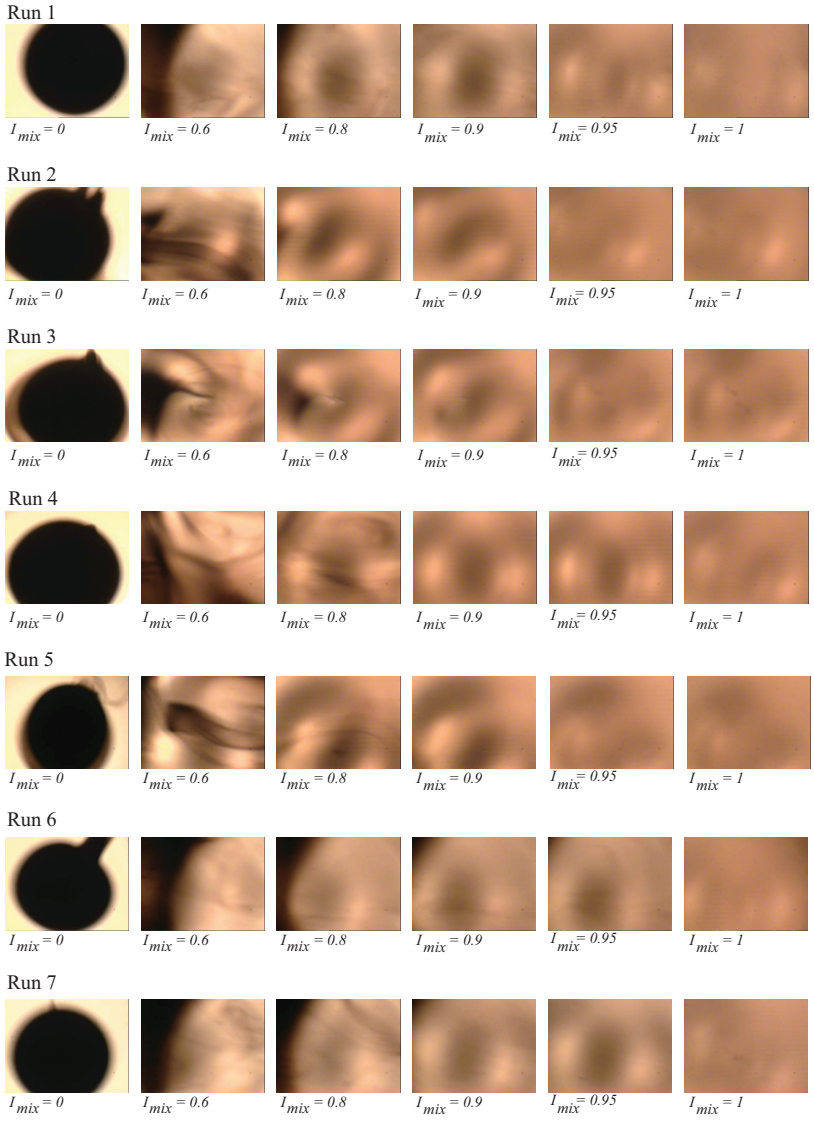

Figure D.3: Sample images captured at different mixing indices for asymmetric excitation without cilia

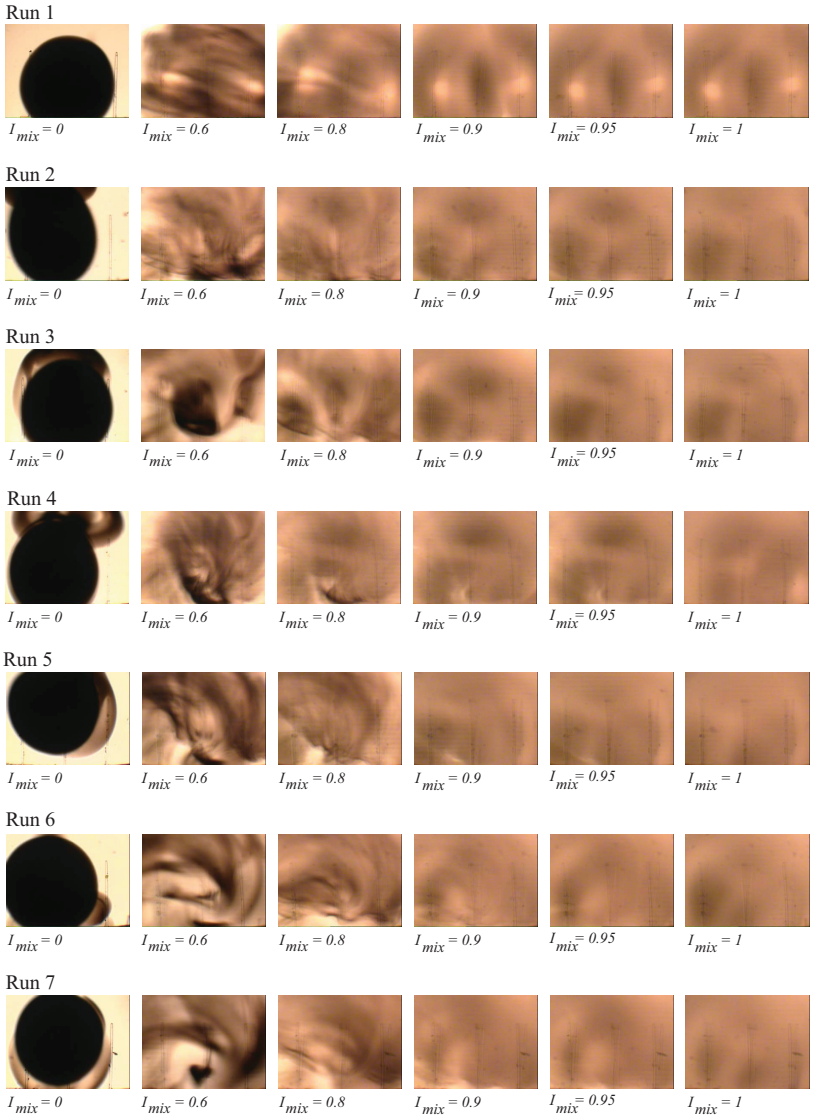

Figure D.4: Sample images captured at different mixing indices for asymmetric excitation with cilia

D.2 Image Analysis and Plotting the Mixing Index

The following is an example for the image analysis and plotting the mixing index for the case with cilia under the influence of the asymmetric actuation in Run1.

Image analysis for determining the mixing index uses the following software tools. [1] Pinnacle studio,version 12, which comes along with the purchase of the Dazzle video creator plus, is used to capture the images from the camera and make the video files from the mixing experiments as shown in Figure D.5.

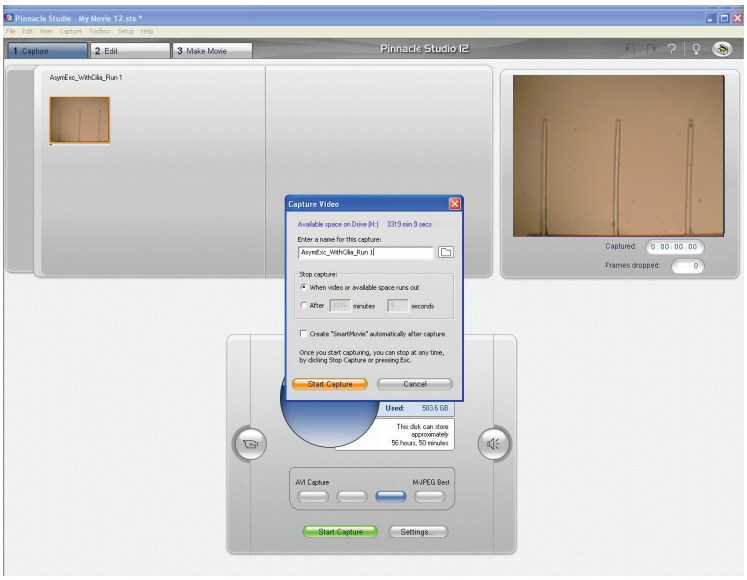

Figure D.5: Pinnacle studio used to capture videos

[2] VirtualDub-1.10.0, free on the website, is used to export the frames/images from the video files with a selected decimation number as shown in in Figures D.6, D.7, and D.8.

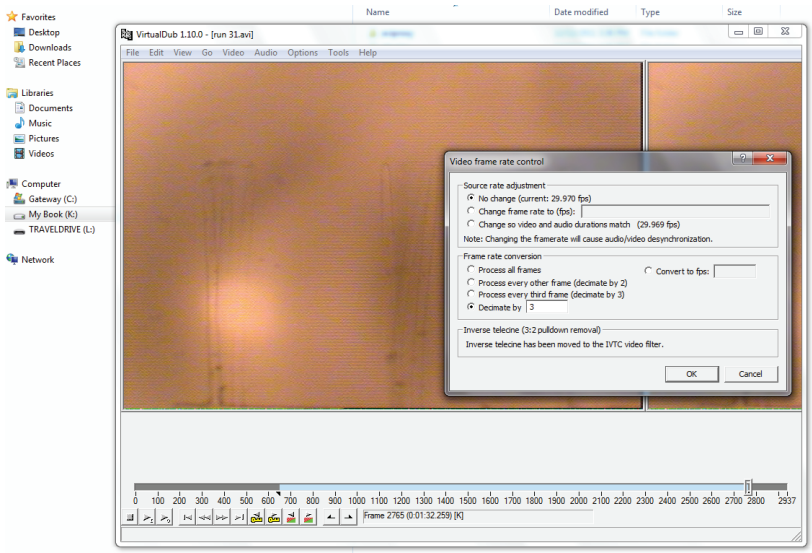

Figure D.6: Selecting the frame range and choosing a decimation number : Decimated by 3 for mixing with cilia and decimated by 15 for mixing without cilia (slower settling time)

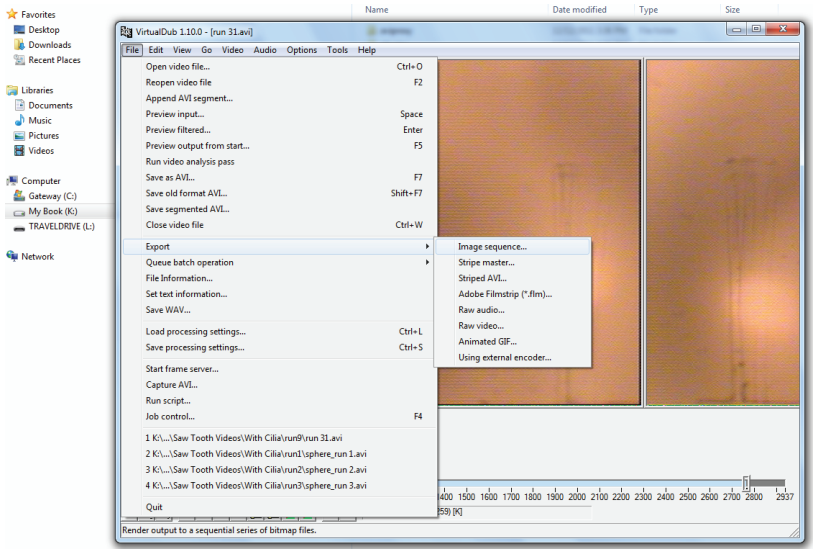

Figure D.7: Exporting the image sequence

[3] Matlab R2009b is used to write the code that can take the information from images.

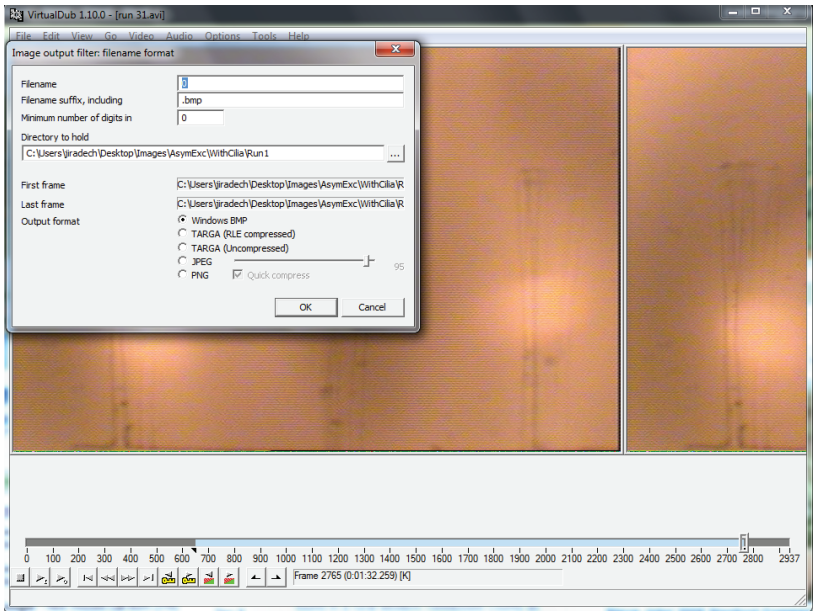

Figure D.8: Storing the images

[3.1] The following Matlab code reads images, computes, and saves the mixing index from the mixing experiment.

```
% step 1
% this file reads images,computes,and saves the mixing index from
% the mixing experiment
clear all; close all; clc;

% set the paramters depending on the experiment
images = 500;  % number of the last image in the file
frame1 = 0;  % number of the first frame
framerate = 30/3; % camera frame rate (30) devided by decimation number(=3)
```

```
file='AsymExc/WithCilia/Run1/';

% define first and last frames which will be c_p at t_0 and c_p at t_N
firstframe = imread(strcat(file,int2str(0),int2str(frame1),'.bmp'));
lastframe = imread(strcat(file,int2str(0),int2str(images),'.bmp'));
first_last = abs(int32(firstframe) - int32(lastframe));
first_lastSum = sum(sum(sum(first_last)));
Mi = [];
wait1 = waitbar(0); % set up a waitbar

% set a for loop for reading images and computing
for i = frame1:images-1
    waitbar(i/(images-1),wait1);
    cur_frame = imread(strcat(file,int2str(0),int2str(i),'.bmp'));
    ImageDelta= abs(int32(cur_frame) - int32(lastframe));
    ImageDeltaSum = sum(sum(sum(ImageDelta)));
    Mi(i-frame1+1,1) = 1-ImageDeltaSum./first_lastSum;
end
close(wait1) % close the waitbar

% set a for loop for computing the mixing index
for i = frame1:images-1
    Mi(i-frame1+1,1)= Mi(i-frame1+1,1)/abs(1-ImageDeltaSum./first_lastSum);
end

time= 0:1/framerate:(images-frame1-1)/framerate; % time vector for the plot
save('AsymExc_WithCilia_Run1','time','Mi') % save in a mat file
```

[3.2] The following Matlab code generates the plot of the mixing index from the mixing experiment.

```
% step 2
% this file produces the plot of the mixing index from the mixing experiment
clear all; close all; clc;

load AsymExc_WithCilia_Run1 % load the mat file saved from step 1
level=0.9; % set 90% mixing time
check = 0;
index = length(Mi);

% set a for loop to search backward for Mi=0.9
for i = length(Mi):-1:1
    if (Mi(i) <= level && check == 0)
        check = 1;index=i;
    end
end

levelline=level*ones(size(time));% draw a horizontal line at Mi=0.9

% plot the mixing index
figure()
plot(time,levelline,'--m',time,Mi,'-b',time(index),Mi(index),'ro')
```

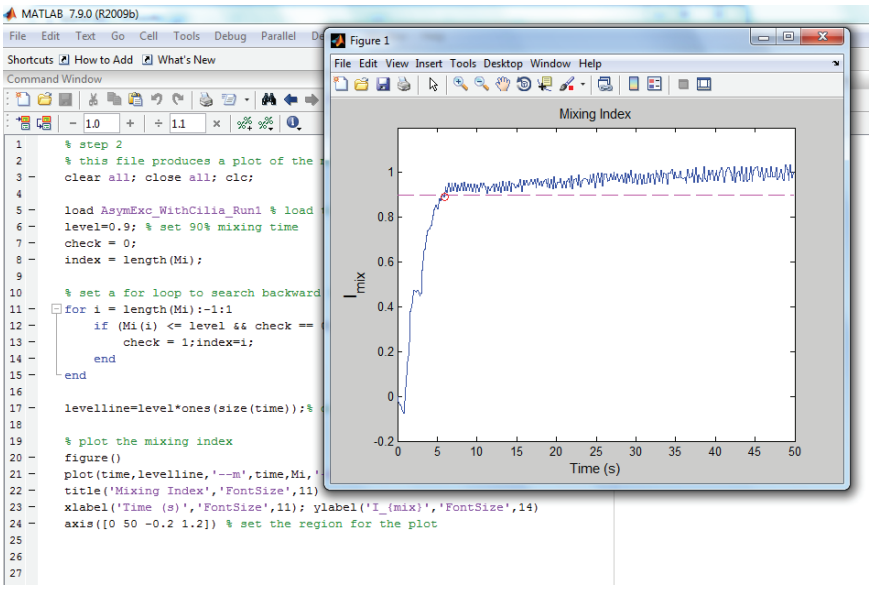

Figure D.9: Mixing index plot

```
title('Mixing Index','FontSize',11)
xlabel('Time (s)','FontSize',11); ylabel('I_{mix}','FontSize',14)
axis([0 50 -0.2 1.2]) % set the region for the plot
```

[4] The plot of the mixing index is generated and shown in Figure D.9.

Appendix E

PARTICLE EXPERIMENTS AND DETERMINING THE SPEEDS

The motion of particles in the flow was evaluated using polymer microspheres (crosslinked poly(styrene/divinylbenzene), mean diameter of 18.97μm, PS07N/1733, Bangs Laboratories, Inc.) with the same operating conditions as the ink-mixing experiment (without the ink) for all four cases: (a) sinusoidal excitation without cilia; (b) sinusoidal excitation with cilia, (c) asymmetric excitation without cilia, and (d) asymmetric excitation with cilia.

E.1 Images Captured from the Particle Experiments in Chapter 4

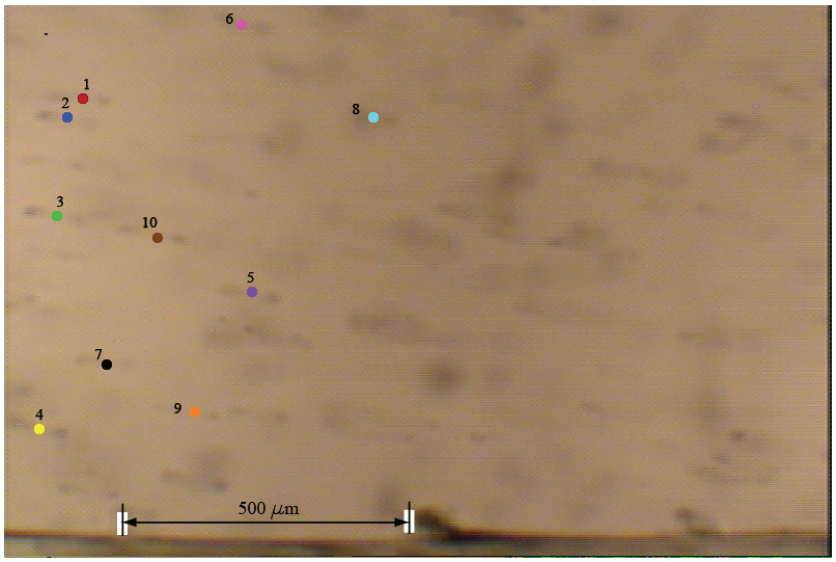

Figure E.1: Captured image used for measuring the distances traveled by particles 1 to 10 while being under the influence of sinusoidal excitation without cilia : Initial frame

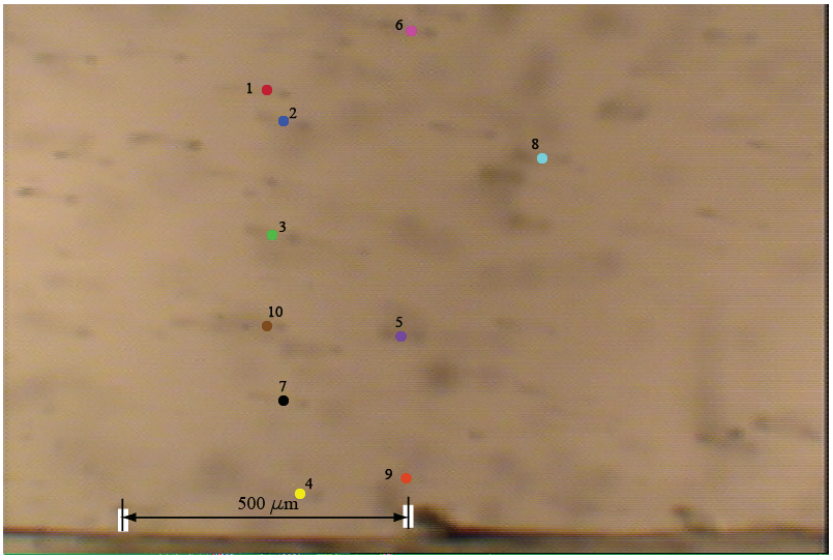

Figure E.2: Captured image used for measuring the distances traveled by particles 1 to 10 while being under the influence of sinusoidal excitation without cilia : Final frame

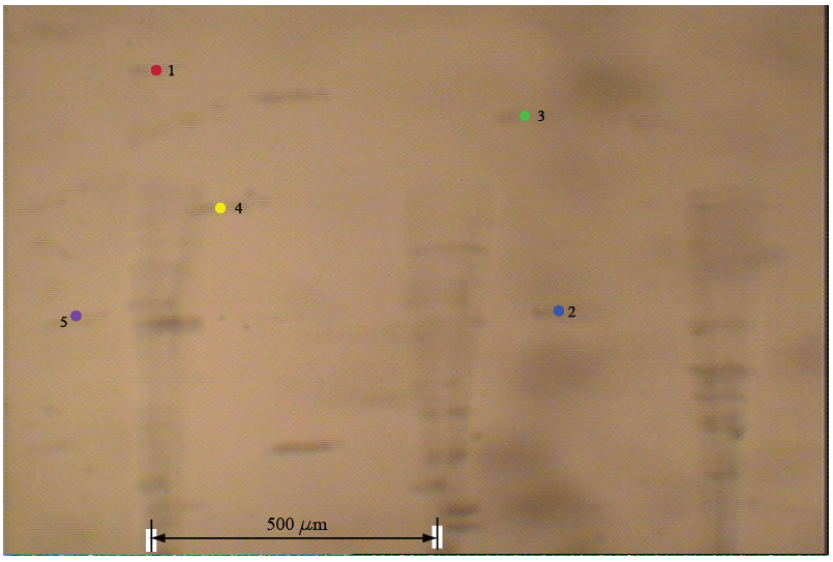

Figure E.3: Captured image used for measuring the distances traveled by particles 1 to 5 while being under the influence of sinusoidal excitation with cilia : Initial frame

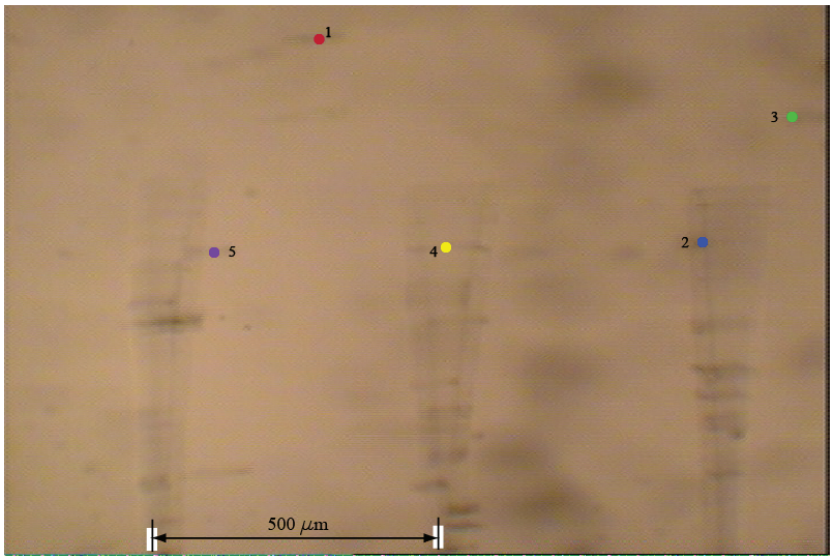

Figure E.4: Captured image used for measuring the distances traveled by particles 1 to 5 while being under the influence of sinusoidal excitation with cilia : Final frame

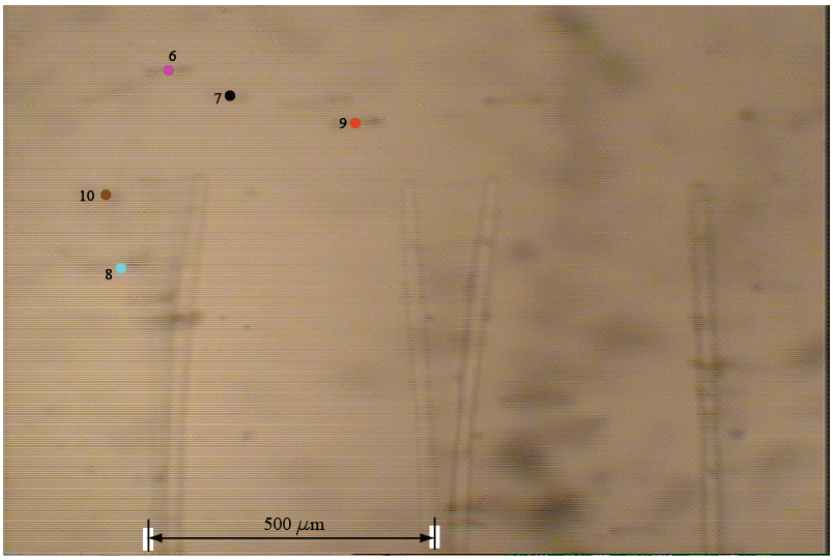

Figure E.5: Captured image used for measuring the distances traveled by particles 6 to 10 while being under the influence of sinusoidal excitation with cilia : Initial frame

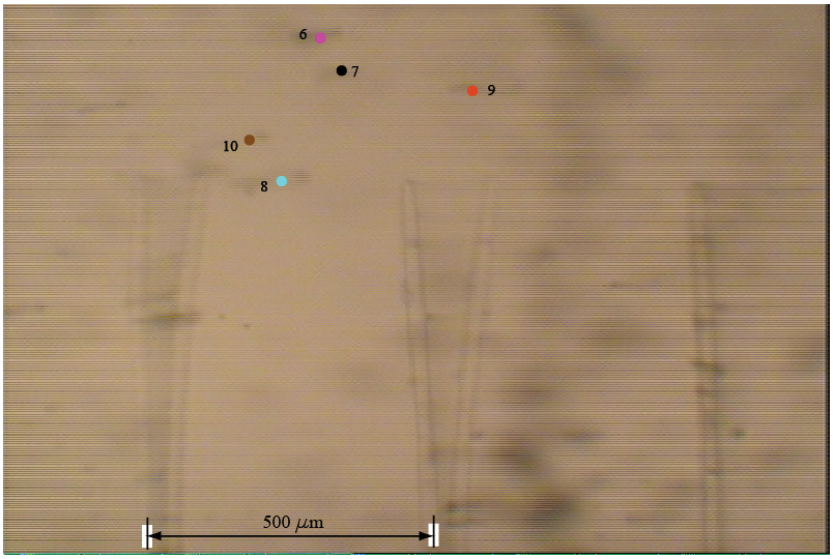

Figure E.6: Captured image used for measuring the distances traveled by particles 6 to 10 while being under the influence of sinusoidal excitation with cilia : Final frame

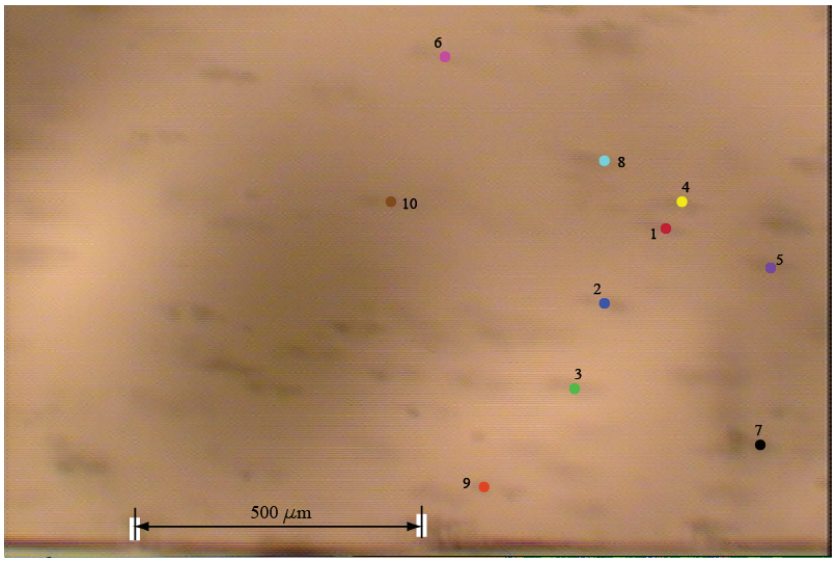

Figure E.7: Captured image used for measuring the distances traveled by particles 1 to 10 while being under the influence of asymmetric excitation without cilia: Initial frame

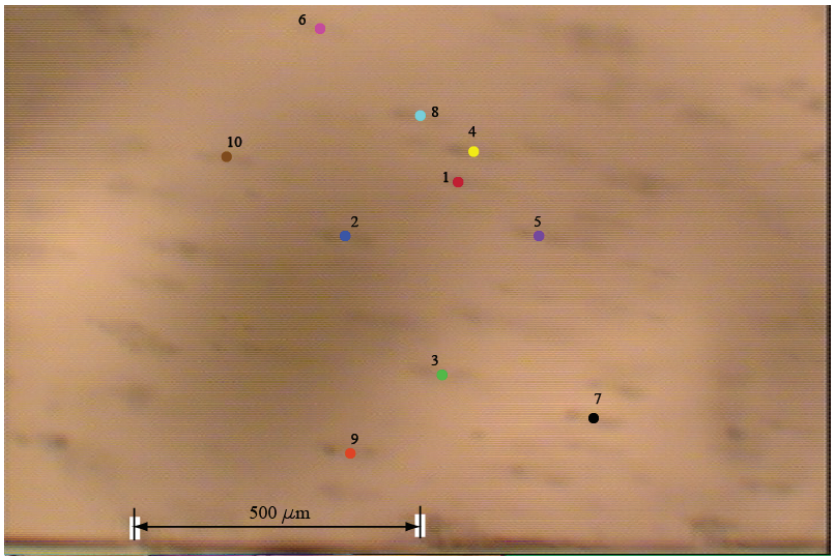

Figure E.8: Captured image used for measuring the distances traveled by particles 1 to 10 while being under the influence of asymmetric excitation without cilia: Final frame

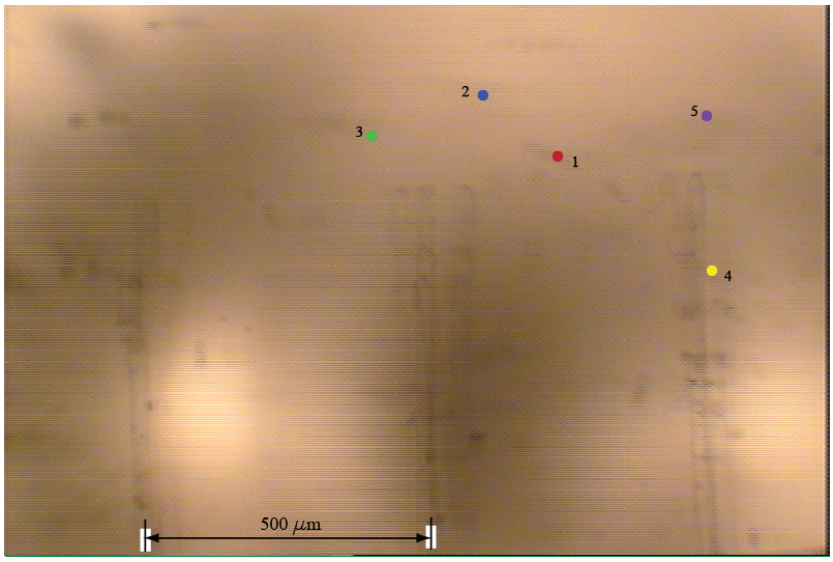

Figure E.9: Captured image used for measuring the distances traveled by particles 1 to 5 while being under the influence of asymmetric excitation with cilia: Initial frame

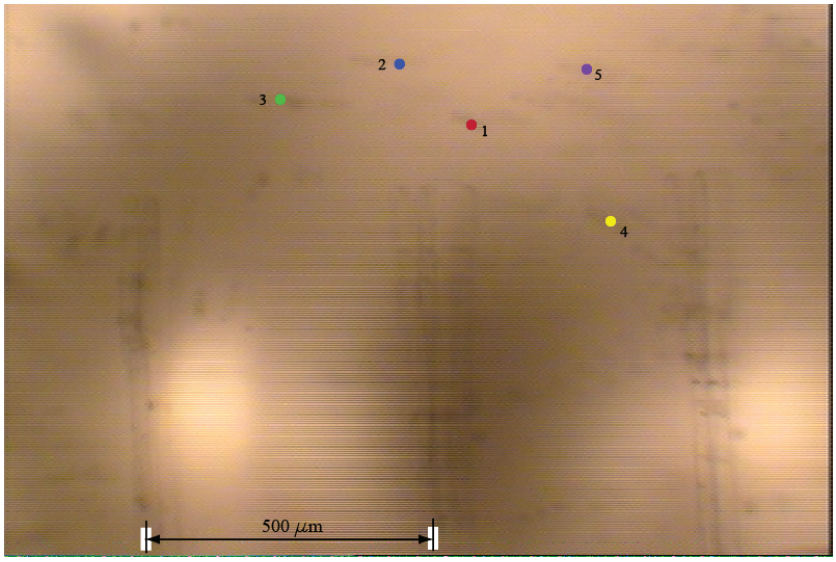

Figure E.10: Captured image used for measuring the distances traveled by particles 1 to 5 while being under the influence of asymmetric excitation with cilia: Final frame

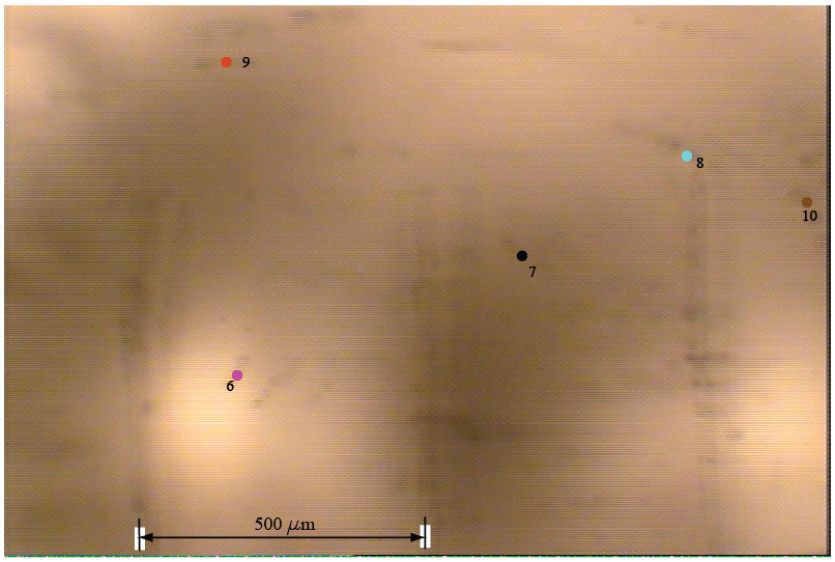

Figure E.11: Captured image used for measuring the distances traveled by particles 6 to 10 while being under the influence of asymmetric excitation with cilia: Initial frame

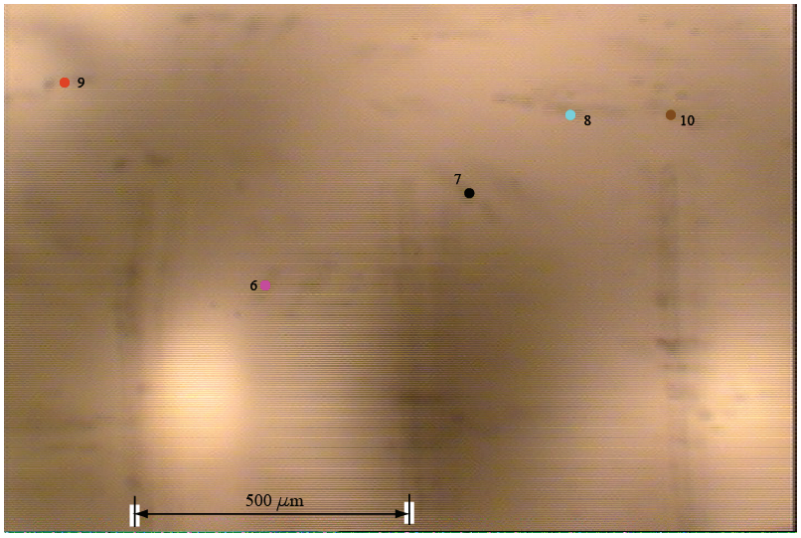

Figure E.12: Captured image used for measuring the distances traveled by particles 6 to 10 while being under the influence of asymmetric excitation with cilia: Final frame

E.2 Determining the Distance Traveled and the Time Taken for Computing the Speed

Each colored dot in each image marks the center of the particle. The xy coordinate values of the center of each dot and the center of the rectangular white mark on the left are obtained using Adobe Illustrator software. With the known coordinate values, the distance on the images between 2 points on the different frames can be calculated. It is noted that the rectangular white marks are not fixed from frame to frame and therefore the relative distances need to be considered.

The actual distance can be determined from the known spacing of $500\mu m$ between the two adjacent cilia. The time taken between the frames can be determined from the known frame rate of the camera of 30 frames/second and the decimation number selected when exporting the image sequence using VirtualDub-1.10.0.

With the distance and time obtained, the speed of the particle is computed and the statistics of the speeds for each case is shown in Table 4.5 in Chapter 4.

Appendix F

STUDENT T-TEST

This appendix shows tests concerning the difference between the two means. For example, it is to show that the observed difference between the means of the mixing time with cilia and the means of the mixing time without cilia is statistically significant or it is attributed to chance. Also it is to show that the observed difference between the means of the speed of the microspheres with cilia and the speed of the microspheres without cilia is statistically significant or it is attributed to chance. For two populations with the means μ_1 and μ_2 and the variancee of σ_1^2 and σ_2^2, the null hypothesis $\mu_1 - \mu_2 = \delta$ is tested, where δ is a specified constant based on indepentdant random samples of size n_1 and n_2. The tests of this null hypothesis against each of the alternatives $\mu_1 - \mu_2 < \delta$, $\mu_1 - \mu_2 > \delta$, and $\mu_1 - \mu_2 \neq \delta$ are considered. The test itself depends on the difference between the sample means $\bar{X}_1 - \bar{X}_2$. The test statistics can be written as [4]

$$t = \frac{(\bar{X}_1 - \bar{X}_2) - \delta}{S_p\sqrt{\frac{1}{n_1} + \frac{1}{n_2}}} \tag{F.1}$$

where

$$S_p^2 = \frac{(n_1 - 1)S_1^2 + (n_2 - 1)S_2^2}{(n_1 + n_2 - 2)}$$

which is a rondom variable having the t distribution with $n_1 + n_2 - 2$ degrees of freedom. The criteria for the two-sample t test are:

Alternative hypothesis	Reject null hypothesis if:
$\mu_1 - \mu_2 < \delta$	$t < -t_\alpha$
$\mu_1 - \mu_2 > \delta$	$t > t_\alpha$
$\mu_1 - \mu_2 \neq \delta$	$t < -t_{\alpha/2}$ *or* $t > t_{\alpha/2}$

Table F.1: Critical regions for testing $\mu_1 - \mu_2 = \delta$

The table for t_α is shown in Figure F.1, from Table 4 in [4].

F.1 Student t-test for Chapter 3

The following test uses the 0.05 level of significance (equivalent to 95% confidence interval) to test whether the difference between the means is statistically significant.

Test [1] : Mixing time without/with cilia for sinusoidal excitation

Step [1]

Null hypothesis : $\mu_1 - \mu_2 = 0$

Alternative hypothesis : $\mu_1 - \mu_2 \neq 0$

Step [2]

Level of significance : $\alpha = 0.05$

Step [3]

Criterion : Reject the null hypothesis if $t < -2.179$ or $t > 2.179$, where 2.179 is the value of $t_{0.025}$ for $7+7-2 = 12$ degrees of freedom (read out from Figure F.1) and t is given by Eq. F.1.

Step [4]

Caculations : The means and the variances of the two samples are
$\bar{X}_1 = 176.4$, $\bar{X}_2 = 14.9$, $S_1^2 = (83.02)^2$, and $S_2^2 = (3.248)^2$,
so that $S_p^2 = \frac{(7-1)(83.02)^2+(7-1)(3.248)^2}{(7+7-2)} = 3451.4$ so $S_p = 58.749$ and

$$t = \frac{(176.4 - 14.9) - 0}{58.749\sqrt{\frac{1}{7} + \frac{1}{7}}} = 5.143$$

Step [5]

Decision : Since $t = 5.143$ exceeds 2.179, the null hypothesis must be rejected at level $\alpha = 0.05$. It is concluded that the difference between the two means is statistically significant and it is not attributed to chance.

F.2 Student t-test for Chapter 4

The statistics of the mixing time and the speed of the microspheres are summarized (from Chapter 4) in Tables F.2 and F.3 respectively.

Excitation Waveform	Mixing time without Cilia (s)	Mixing time with Cilia (s)
Sinusoidal	175.00±45.45	13.56±1.94
Asymmetric	57.14±15.74	5.17±0.67

Table F.2: Mixing time, mean value and standard deviation for 7 runs for each of the four cases — without and with cilia, and symmetric (sinusoidal) and asymmetric excitation

Excitation Waveform	Speed without Cilia (μm/s)	Speed with Cilia (μm/s)
Sinusoidal	335.67±47.01	1026.35±214.46
Asymmetric	616.13±151.06	2317.16±304.22

Table F.3: Speed, mean value and standard deviation for 10 microspheres for each of the four cases — without and with cilia, and symmetric (sinusoidal) and asymmetric excitation

The following tests use the 0.05 level of significance (equivalent to 95% confidence interval) to test whether the difference between the means is statistically significant.

Test [1] : Mixing time without/with cilia for sinusoidal excitation

Step [1]

Null hypothesis : $\mu_1 - \mu_2 = 0$

Alternative hypothesis : $\mu_1 - \mu_2 \neq 0$

Step [2]

Level of significance : $\alpha = 0.05$

Step [3]

Criterion : Reject the null hypothesis if $t < -2.179$ or $t > 2.179$, where 2.179 is the value of $t_{0.025}$ for $7 + 7 - 2 = 12$ degrees of freedom (read out from Figure F.1) and t is given by Eq. F.1

Step [4]

Caculations : The means and the variances of the two samples are
$\bar{X}_1 = 175.0$, $\bar{X}_2 = 13.56$, $S_1^2 = (45.45)^2$, and $S_2^2 = (1.94)^2$,
so that $S_p^2 = \frac{(7-1)(45.45)^2+(7-1)(1.94)^2}{(7+7-2)} = 1034.72$ so $S_p = 32.167$ and

$$t = \frac{(175.0 - 13.56) - 0}{32.167\sqrt{\frac{1}{7} + \frac{1}{7}}} = 9.389$$

Step [5]

Decision : Since $t = 9.389$ exceeds 2.179, the null hypothesis must be rejected at level $\alpha = 0.05$. It is concluded that the difference between the two means is statistically significant and it is not attributed to chance.

Test [2] : Mixing time without/with cilia for asymmetric excitation

Step [1]

Null hypothesis : $\mu_1 - \mu_2 = 0$

Alternative hypothesis : $\mu_1 - \mu_2 \neq 0$

Step [2]

Level of significance : $\alpha = 0.05$

Step [3]

Criterion : Reject the null hypothesis if $t < -2.179$ or $t > 2.179$, where 2.179 is the value of $t_{0.025}$ for $7 + 7 - 2 = 12$ degrees of freedom (read out from Figure F.1) and t is given by Eq. F.1

Step [4]

Caculations : The means and the variances of the two samples are
$\bar{X}_1 = 57.14$, $\bar{X}_2 = 5.17$, $S_1^2 = (15.74)^2$, and $S_2^2 = (0.67)^2$,
so that $S_p^2 = \frac{(7-1)(15.74)^2+(7-1)(0.67)^2}{(7+7-2)} = 119.881$ so $S_p = 10.949$ and

$$t = \frac{(57.14 - 5.17) - 0}{10.949\sqrt{\frac{1}{7} + \frac{1}{7}}} = 8.880$$

Step [5]

Decision : Since $t = 8.880$ exceeds 2.179, the null hypothesis must be rejected at level $\alpha = 0.05$. It is concluded that the difference between the two means is statistically significant and it is not attributed to chance.

Test [3] : Mixing time for the case with cilia with symmetric/asymmetric excitation

Step [1]

Null hypothesis : $\mu_1 - \mu_2 = 0$

Alternative hypothesis : $\mu_1 - \mu_2 \neq 0$

Step [2]

Level of significance : $\alpha = 0.05$

Step [3]

Criterion : Reject the null hypothesis if $t < -2.179$ or $t > 2.179$, where 2.179 is the value of $t_{0.025}$ for $7 + 7 - 2 = 12$ degrees of freedom (read out from Figure F.1) and t is given by Eq. F.1

Step [4]

Caculations : The means and the variances of the two samples are
$\bar{X}_1 = 13.56$, $\bar{X}_2 = 5.17$, $S_1^2 = (1.94)^2$, and $S_2^2 = (0.67)^2$,

so that $S_p^2 = \frac{(7-1)(5.17)^2+(7-1)(0.67)^2}{(7+7-2)} = 2.106$ so $S_p = 1.451$ and

$$t = \frac{(13.56 - 5.17) - 0}{1.451\sqrt{\frac{1}{7} + \frac{1}{7}}} = 10.815$$

Step [5]

Decision : Since $t = 10.815$ exceeds 2.179, the null hypothesis must be rejected at level $\alpha = 0.05$. It is concluded that the difference between the two means is statistically significant and it is not attributed to chance.

Test [4] : Mixing time for the case without cilia with symmetric/ asymmetric excitation

Step [1]

Null hypothesis : $\mu_1 - \mu_2 = 0$

Alternative hypothesis : $\mu_1 - \mu_2 \neq 0$

Step [2]

Level of significance : $\alpha = 0.05$

Step [3]

Criterion : Reject the null hypothesis if $t < -2.179$ or $t > 2.179$, where 2.179 is the value of $t_{0.025}$ for $7 + 7 - 2 = 12$ degrees of freedom (read out from Figure F.1) and t is given by Eq. F.1

Step [4]

Caculations : The means and the variances of the two samples are
$\bar{X}_1 = 175.0$, $\bar{X}_2 = 57.14$, $S_1^2 = (45.45)^2$, and $S_2^2 = (15.74)^2$,
so that $S_p^2 = \frac{(7-1)(45.45)^2+(7-1)(15.74)^2}{(7+7-2)} = 1156.7$ so $S_p = 34.010$ and

$$t = \frac{(175.0 - 57.14) - 0}{34.010\sqrt{\frac{1}{7} + \frac{1}{7}}} = 6.483$$

Step [5]

Decision : Since $t = 6.483$ exceeds 2.179, the null hypothesis must be rejected

at level $\alpha = 0.05$. It is concluded that the difference between the two means is statistically significant and it is not attributed to chance.

Test [5] : Microsphere speed without/with cilia for sinusoidal excitation

Step [1]

Null hypothesis : $\mu_1 - \mu_2 = 0$

Alternative hypothesis : $\mu_1 - \mu_2 \neq 0$

Step [2]

Level of significance : $\alpha = 0.05$

Step [3]

Criterion : Reject the null hypothesis if $t < -2.101$ or $t > 2.101$, where 2.101 is the value of $t_{0.025}$ for $10 + 10 - 2 = 18$ degrees of freedom (read out from Figure F.1) and t is given by Eq. F.1

Step [4]

Caculations : The means and the variances of the two samples are
$\bar{X}_1 = 335.67$, $\bar{X}_2 = 1026.35$, $S_1^2 = (47.01)^2$, and $S_2^2 = (214.46)^2$,
so that $S_p^2 = \frac{(10-1)(47.01)^2+(10-1)(214.46)^2}{(10+10-2)} = 24102$ so $S_p = 155.247$ and

$$t = \frac{(335.67 - 1026.35) - 0}{155.247\sqrt{\frac{1}{10} + \frac{1}{10}}} = -9.948$$

Step [5]

Decision : Since $t = -9.948$ is less than -2.101, the null hypothesis must be rejected at level $\alpha = 0.05$. It is concluded that the difference between the two means is statistically significant and it is not attributed to chance.

Test [6] : Microsphere speed without/with cilia for asymmetric excitation

Step [1]

Null hypothesis : $\mu_1 - \mu_2 = 0$

Alternative hypothesis : $\mu_1 - \mu_2 \neq 0$

Step [2]

Level of significance : $\alpha = 0.05$

Step [3]

Criterion : Reject the null hypothesis if $t < -2.101$ or $t > 2.101$, where 2.101 is the value of $t_{0.025}$ for $10 + 10 - 2 = 18$ degrees of freedom (read out from Figure F.1) and t is given by Eq. F.1

Step [4]

Caculations : The means and the variances of the two samples are
$\bar{X}_1 = 616.13$, $\bar{X}_2 = 2317.16$, $S_1^2 = (151.06)^2$, and $S_2^2 = (304.22)^2$,
so that $S_p^2 = \frac{(10-1)(151.06)^2+(10-1)(304.22)^2}{(10+10-2)} = 57684$ so $S_p = 240.176$ and

$$t = \frac{(616.13 - 2317.16) - 0}{240.176\sqrt{\frac{1}{10} + \frac{1}{10}}} = -15.837$$

Step [5]

Decision : Since $t = -15.837$ is less than -2.101, the null hypothesis must be rejected at level $\alpha = 0.05$. It is concluded that the difference between the two means is statistically significant and it is not attributed to chance.

Test [7] : Microsphere speed for the case with cilia with symmetric/asymmetric excitation

Step [1]

Null hypothesis : $\mu_1 - \mu_2 = 0$

Alternative hypothesis : $\mu_1 - \mu_2 \neq 0$

Step [2]

Level of significance : $\alpha = 0.05$

Step [3]

Criterion : Reject the null hypothesis if $t < -2.101$ or $t > 2.101$, where 2.101 is

the value of $t_{0.025}$ for $10 + 10 - 2 = 18$ degrees of freedom (read out from Figure F.1) and t is given by Eq. F.1

Step [4]

Caculations : The means and the variances of the two samples are
$\bar{X}_1 = 1026.35$, $\bar{X}_2 = 2317.16$, $S_1^2 = (214.46)^2$, and $S_2^2 = (304.22)^2$,
so that $S_p^2 = \frac{(10-1)(214.46)^2+(10-1)(304.22)^2}{(10+10-2)} = 69271$ so $S_p = 263.195$ and

$$t = \frac{(1026.35 - 2317.16) - 0}{263.195\sqrt{\frac{1}{10} + \frac{1}{10}}} = -9.437$$

Step [5]

Decision : Since $t = -9.437$ is less than -2.101, the null hypothesis must be rejected at level $\alpha = 0.05$. It is concluded that the difference between the two means is statistically significant and it is not attributed to chance.

Test [8] : Microsphere speed for the case without cilia with symmetric/ asymmetric excitation

Step [1]

Null hypothesis : $\mu_1 - \mu_2 = 0$

Alternative hypothesis : $\mu_1 - \mu_2 \neq 0$

Step [2]

Level of significance : $\alpha = 0.05$

Step [3]

Criterion : Reject the null hypothesis if $t < -2.101$ or $t > 2.101$, where 2.101 is the value of $t_{0.025}$ for $10 + 10 - 2 = 18$ degrees of freedom (read out from Figure F.1) and t is given by Eq. F.1

Step [4]

Caculations : The means and the variances of the two samples are
$\bar{X}_1 = 335.67$, $\bar{X}_2 = 616.13$, $S_1^2 = (47.01)^2$, and $S_2^2 = (151.06)^2$,

so that $S_p^2 = \frac{(10-1)(47.01)^2+(10-1)(151.06)^2}{(10+10-2)} = 12515$ so $S_p = 111.868$ and

$$t = \frac{(335.67 - 616.13) - 0}{111.868\sqrt{\frac{1}{10} + \frac{1}{10}}} = -5.606$$

Step [5]

Decision : Since $t = -5.606$ is less than -2.101, the null hypothesis must be rejected at level $\alpha = 0.05$. It is concluded that the difference between the two means is statistically significant and it is not attributed to chance.

The following tests use the 0.01 level of significance (equivalent to 99% confidence interval) to test whether the difference between the means is statistically significant.

Test [9] : Mixing time for the case with cilia with symmetric/asymmetric excitation

Step [1]

Null hypothesis : $\mu_1 - \mu_2 = 0$

Alternative hypothesis : $\mu_1 - \mu_2 \neq 0$

Step [2]

Level of significance : $\alpha = 0.01$

Step [3]

Criterion : Reject the null hypothesis if $t < -3.055$ or $t > 3.055$, where 3.055 is the value of $t_{0.005}$ for $7 + 7 - 2 = 12$ degrees of freedom (read out from Figure F.1) and t is given by Eq. F.1

Step [4]

Caculations : The means and the variances of the two samples are
$\bar{X}_1 = 13.56$, $\bar{X}_2 = 5.17$, $S_1^2 = (1.94)^2$, and $S_2^2 = (0.67)^2$,
so that $S_p^2 = \frac{(7-1)(5.17)^2+(7-1)(0.67)^2}{(7+7-2)} = 2.106$ so $S_p = 1.451$ and

$$t = \frac{(13.56 - 5.17) - 0}{1.451\sqrt{\frac{1}{7} + \frac{1}{7}}} = 10.815$$

Step [5]

Decision : Since $t = 10.815$ exceeds 3.055, the null hypothesis must be rejected at level $\alpha = 0.01$. It is concluded that the difference between the two means is statistically significant and it is not attributed to chance.

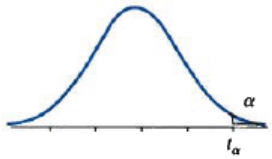

TABLE 4 Values of t_α

v	$\alpha = 0.10$	$\alpha = 0.05$	$\alpha = 0.025$	$\alpha = 0.01$	$\alpha = 0.00833$	$\alpha = 0.00625$	$\alpha = 0.005$	v
1	3.078	6.314	12.706	31.821	38.204	50.923	63.657	1
2	1.886	2.920	4.303	6.965	7.650	8.860	9.925	2
3	1.638	2.353	3.182	4.541	4.857	5.392	5.841	3
4	1.533	2.132	2.776	3.747	3.961	4.315	4.604	4
5	1.476	2.015	2.571	3.365	3.534	3.810	4.032	5
6	1.440	1.943	2.447	3.143	3.288	3.521	3.707	6
7	1.415	1.895	2.365	2.998	3.128	3.335	3.499	7
8	1.397	1.860	2.306	2.896	3.016	3.206	3.355	8
9	1.383	1.833	2.262	2.821	2.934	3.111	3.250	9
10	1.372	1.812	2.228	2.764	2.870	3.038	3.169	10
11	1.363	1.796	2.201	2.718	2.820	2.981	3.106	11
12	1.356	1.782	2.179	2.681	2.780	2.934	3.055	12
13	1.350	1.771	2.160	2.650	2.746	2.896	3.012	13
14	1.345	1.761	2.145	2.624	2.718	2.864	2.977	14
15	1.341	1.753	2.131	2.602	2.694	2.837	2.947	15
16	1.337	1.746	2.120	2.583	2.673	2.813	2.921	16
17	1.333	1.740	2.110	2.567	2.655	2.793	2.898	17
18	1.330	1.734	2.101	2.552	2.639	2.775	2.878	18
19	1.328	1.729	2.093	2.539	2.625	2.759	2.861	19
20	1.325	1.725	2.086	2.528	2.613	2.744	2.845	20
21	1.323	1.721	2.080	2.518	2.602	2.732	2.831	21
22	1.321	1.717	2.074	2.508	2.591	2.720	2.819	22
23	1.319	1.714	2.069	2.500	2.582	2.710	2.807	23
24	1.318	1.711	2.064	2.492	2.574	2.700	2.797	24
25	1.316	1.708	2.060	2.485	2.566	2.692	2.787	25
26	1.315	1.706	2.056	2.479	2.559	2.684	2.779	26
27	1.314	1.703	2.052	2.473	2.553	2.676	2.771	27
28	1.313	1.701	2.048	2.467	2.547	2.669	2.763	28
29	1.311	1.699	2.045	2.462	2.541	2.663	2.756	29
inf.	1.282	1.645	1.960	2.326	2.394	2.498	2.576	inf.

Figure F.1: Values of t_α , from Table 4 in [4]

VITA

Jiradech Kongthon was born and grew up in Nakhon Si Thammarat located in the south of Thailand. He attended local schools for his primary education. He went to Benjamarachutit School in his hometown for his high school and then moved to Bangkok for his undergraduate study.

He received a Bachelor of Engineering in Mechanical Engineering from the King Mongkut's Institute of Technology Thonburi, (later renamed to King's Mongkut University of Technology Thonburi) in 1995. After his undergraduate study, he worked for engineering and construction firms in Bangkok for 6 years.

In 2001, he decided to move to the United States for his graduate studies. He earned a Master of Science in Engineering Management from the California State University, Northridge in 2002 and a Master of Science in Aerospace and Mechanical Engineering from the University of Southern California, Los Angeles in 2006.

He earned a PhD degree in Mechanical Engineering from the University of Washington, Seattle in 2011.

He worked on the dissertation titled "Modeling and Control of Biomimetic Cilia-Based Devices for Microfluidic Applications" for his PhD degree. This research involves employing microfabricated soft biomimetric cilia in liquids actuated by low frequency waves generated from a piezoactuator in order to manipulate and control velocity fields (or flow directions of the liquids) to improve micromixing. The investigations deal with the integration of fluid-structure interactions, dynamics, modeling and motion controls. His graduate research gave him extensive experiences in controlling motions of both structural components and fluid elements at the microscale level with high-precision controls. Additionally, he learned how to make microdevices

based on microfabrication. These research skills will benefit further research efforts in developing microfluidic devices. In the course of his graduate studies, he has also begun to hone his teaching skills by serving as an instructor and a teaching assistant at the University of Washington.

His research interests include dynamics, modeling, controls, air conditioning systems, and green building technologies.

He welcomes your correspondence and can be reached at `jiradechkt@gmail.com`.